7-20-2010

SST: Integrated Fluorocarbon Microsensor System Using Catalytic Modification

M. Clayton Wheeler
Principal Investigator; University of Maine, Orono

Final Report for Period: 09/2008 - 08/2009
Submitted on: 07/20/2010
Principal Investigator: Wheeler, M. C.
Award ID: 0428341
Organization: University of Maine
Submitted By:
Wheeler, M. - Principal Investigator
Title:
SST: Integrated Fluorocarbon Microsensor System Using Catalytic Modification

Project Participants

Senior Personnel

Name: Wheeler, M. Clayton
Worked for more than 160 Hours: Yes
Contribution to Project:
Wheeler was principle investigator and supervised students working on microhotplate sensor fabrication, materials deposition, sensor testing, and sensor applications.

Name: Ressom, Habtom
Worked for more than 160 Hours: No
Contribution to Project:
Ressom transferred to Georgetown University prior to receiving this award. He participated in weekly group meetings via video conference as a technical advisor rather than a Co-PI. Primary responsibilities for supervising students conducting data analysis were transferred to Segee.

Name: Pereira da Cunha, Mauricio
Worked for more than 160 Hours: Yes
Contribution to Project:
Pereira da Cunha directed overall project, along with Wheeler, and supervised students working on surface acoustic wave sensor fabrication, testing and applications.

Name: Segee, Bruce
Worked for more than 160 Hours: Yes
Contribution to Project:
Segee participated as a Co-PI responsible for data analysis since Ressom transferred to Georgetown University.

Name: Nittel, Silvia
Worked for more than 160 Hours: No
Contribution to Project:
Nittel co-supervised a graduate student working on geospatial integration of sensor systems.

Post-doc

Graduate Student

Name: Shirke, Amol
Worked for more than 160 Hours: Yes
Contribution to Project:
Supervised by Wheeler and supported by this grant.
Studied desorption kinetics on sensor materials.

Name: Clark, Aaron
Worked for more than 160 Hours: Yes
Contribution to Project:
Supervised by Wheeler and supported by NSF/GK-12.

Studied chemical vapor deposition of sensor materials on microhotplates and correlated decomposition of analytes to temperature programmed sensing results.

Name: More, Daesha

Worked for more than 160 Hours: Yes

Contribution to Project:

Supervised by Wheeler and supported by this grant.
Developed clean room and micromachining processes to make microhotplate sensor chips. Documented by M.S. thesis including documentary video.

Name: Meulendyk, Bennett

Worked for more than 160 Hours: Yes

Contribution to Project:

Supervised by Pereira da Cunha and co-supported by NSF/IGERT.
Fabricated surface acoustic wave sensors and characterized sensitivity for HF gas detection.

Name: Winchenbach, Samuel

Worked for more than 160 Hours: Yes

Contribution to Project:

Supervised by Segee and supported by this grant.
Developed new technique for analyzing simulated temperature programmed sensing data based on surface reaction kinetics.

Name: Jin, Guang

Worked for more than 160 Hours: Yes

Contribution to Project:

Supervised by Nittel and supported by this grant.
Developed gas delivery and sensor control hardware/software. Studying analysis of data from distributed sensor networks.

Undergraduate Student

Name: DeAngelis, John

Worked for more than 160 Hours: Yes

Contribution to Project:

Supervised by Wheeler on unsupported undergraduate honors thesis.
Topic: Finite element modeling of thermal characteristics of microhotplate sensors.

Name: Seekins, Tyler

Worked for more than 160 Hours: Yes

Contribution to Project:

Tyler worked with John Hessler to construct a system for chemical vapor deposition of materials on microhotplate sensors.

Name: Hessler, John

Worked for more than 160 Hours: Yes

Contribution to Project:

John was supvised by Wheeler and worked with Tyler Seekins to construct a system for chemical vapor deposition of materials on microhotplate sensors.

Name: Whitney, Raymond

Worked for more than 160 Hours: Yes

Contribution to Project:

Student designed photolithography masks for surface acoustic wave and microhotplate devices. Also assisted with clean room fabrication.

Technician, Programmer

Other Participant

Research Experience for Undergraduates

Name: Haluska, David

Worked for more than 160 Hours: Yes

Contribution to Project:

Supervised by Wheeler and supported by this grant.
Topic: Chemical vapor deposition of TiO2 and Pt-catalyzed TiO2.

Years of schooling completed: Junior

Home Institution: Same as Research Site

Home Institution if Other:

Home Institution Highest Degree Granted(in fields supported by NSF): Doctoral Degree

Fiscal year(s) REU Participant supported: 2005

REU Funding: REU supplement

Name: White, John

Worked for more than 160 Hours: Yes

Contribution to Project:

Supervised by Wheeler and supported by this grant.
Topic: X-ray photoelectron spectroscopy of sensor materials.

Years of schooling completed: Sophomore

Home Institution: Other than Research Site

Home Institution if Other: McGill University

Home Institution Highest Degree Granted(in fields supported by NSF): Doctoral Degree

Fiscal year(s) REU Participant supported: 2006

REU Funding: REU supplement

Name: Beote, Brendon

Worked for more than 160 Hours: Yes

Contribution to Project:

Developed and applied method for chemical vapor deposition of tungten oxide and platinum films on microhotplate sensor platforms. Supported by this grant and participated in UMaine's Sensors REU program.

Years of schooling completed: Junior

Home Institution: Same as Research Site

Home Institution if Other:

Home Institution Highest Degree Granted(in fields supported by NSF): Doctoral Degree

Fiscal year(s) REU Participant supported: 2009

REU Funding: REU supplement

Organizational Partners

NIST/Process Measurments Division

NIST fabricated several microhotplate sensors that we used to measure analyte adsorption kinetics.

Other Collaborators or Contacts

Steve Semancik, NIST Process Measurements Division
Richard Cavicchi, NIST Process Measurements Division

Activities and Findings

Research and Education Activities:

Developed microhotplates.
Developed surface acoustic wave HF gas sensor.
Created a computer model for predicting sensor response as a function of analyte reaction kinetics.
Fabricated LabView automated gas delivery, sensor control and data acquisition system.
Created video documentary of clean room processes for microhotplate sensor fabrication.
Developed isothermal desorption model and measured desorption kinetics of sub-femtomolar quantities of benzoic acid on a tin-oxide microhotplate sensor. Presented these results at 2007 Physical Electronics Conference.
Modified isothermal desorption model using Monte Carlo simulation to describe desorption kinetics of 2-Propanol on oxidized TiO2 sensor.
One Master's and one Ph.D. thesis completed, one Ph.D. defense expected May 2010.

Findings:

New methodology for analysis of temperature programmed sensing data.
New sensor for detecting decomposition products of fluorine-containing analytes.
New understanding of molecular interactions with sensor materials.
Documentation of Maine's Laboratory for Surface Science and Technology's microhotplate fabrications processes.
Improved understanding of chemical mechanism for Surface Acoustic Wave hydrogen fluoride sensor.
New application of microhotplates for calorimetric measurements of surface catalytic reaction rates.

Training and Development:

One participant was an NSF:GK12 fellow who taught and disseminated research results to an area high school.
One participant was an NSF:IGERT fellow who integrated his research experience in a team of sensor network engineers.
Three participants were NSF/REU fellows.
Two video documentaries were created.

Outreach Activities:

See GK-12 discussion in previous section.
NSF/REU interacted with area teachers in weekly NSF/RET presentations.

Journal Publications

Meulendyk, BJ; Wheeler, MC; Da Cunha, MP, "Analyses and mitigation of spurious scattered signals in acoustic wave reflection measurements", NONDESTRUCTIVE TESTING AND EVALUATION, p. 155, vol. 21, (2006). Published, 10.1080/1058975070119173

Shirke, AG; Cavicchi, RE; Semancik, S; Jackson, RH; Frederick, BG; Wheeler, MC, "Ferntomolar isothermal desorption using microhotplate sensors", JOURNAL OF VACUUM SCIENCE & TECHNOLOGY A, p. 514, vol. 25, (2007). Published, 10.1116/1.272085

Wheeler, MC; Cavicchi, RE; Semancik, S, "Tin oxide microsensor arrays as probes for the oscillatory CO oxidation reaction on supported platinum", JOURNAL OF PHYSICAL CHEMISTRY C, p. 3328, vol. 111, (2007). Published, 10.1021/jp067173

Jin, G; Nittel, S, "Toward spatial window queries over continuous phenomena in sensor networks", IEEE TRANSACTIONS ON PARALLEL AND DISTRIBUTED SYSTEMS, p. 559, vol. 19, (2008). Published, 10.1109/TPDS.2007.7074

B. J. Meulendyk, M. Clayton Wheeler, M. Pereira da Cunha, "Hydrogen Fluoride Gas Detection with SAW Resonators on Multiple Quartz Orientations", IEEE Sensors, p. , vol. , (2010). Submitted,

Books or Other One-time Publications

S. Winchenbach, M. C. Wheeler, M. Pereira da Cunha, and B. Segee, "Demonstrating A Novel Approach To The Control Of Microhotplate Sensors Utilizing A Distributed Computing Approach And Numeric Modeling", (2007). Conference Proceeding, Published
Bibliography: 2007 AIChE Annual Meeting Conference Proceedings on CD

A. Clark, M. Pereira da Cunha, B. Segee, and M. C. Wheeler, "Correlation Of Microhotplate Metal Oxide Sensor Response To Catalytic Fluorocarbon Decomposition Activity", (2007). Conference Proceeding, Published
Bibliography: 2007 AIChE Annual Meeting Conference Proceedings on CD

B. J. Meulendyk, M. C. Wheeler , B. Segee, and M. Pereira da Cunha, "Sensitivity Of A Surface Acoustic Wave Hydrogen Fluoride Sensor To Quartz Substrate Etching", (2007). Conference Proceeding, Published
Bibliography: 2007 AIChE Annual Meeting Conference Proceedings on CD

Jin, G. and Nittel, S., "Efficient Event Detection in Sensor Network", (2006). Conference Proceeding, Published
Bibliography: Workshop Mobile Location-Aware Sensor Networks, in conjunction with MDM

Jin, G. and Nittel, S., "Tracking Deformable 2D Objects", (2008). Conference Proceedings, Published
Bibliography: Proceedings of ACM Conference Advances in Geographic Information Systems

Segee, B., Perry, M. J., Carter, C., Blanchette, R. and Winchenbach, S., "Visualization Of Large Scientific Data Sets On A Parallel System With A Tiled Display", (2007). Conference Proceeding, Published
Bibliography: Proceedings of The 19th IASTED International Conference on Parallel and Distributed Computing and Systems PDCS

R. Nelson, W. J. DeSisto, B. G. Frederick, A. van Heiningen, and M. C. Wheeler, "High Throughput Microcalorimetry for Catalyst Discovery", (2008). Conference Proceeding, Published
Bibliography: AIChE Annual Meeting Conference Proceedings on CD, New York, NY

Jin, G., "Towards Spatial Queries over Phenomena in Sensor Networks", (2009). Thesis, Published
Bibliography: University of Maine Ph.D. Dissertation SIE2009-001

More, D., "Microhotplate Sensor Array Fabrication", (2007). Thesis, Published
Bibliography: University of Maine Thesis CHE2007-004

B. J. Meulendyk and M. Pereira da Cunha, "Suppression of transverse waveguide modes for SAW resonators with Pt and Pt/Rh/ZrO2 electrodes", (2009). Conference Proceeding, Published
Bibliography: 2009 IEEE Ultrasonics Symposium Proceedings

Meulendyk, B., "Design, Fabrication, and Testing of Quartz Surface Acoustic Wave Resonators for HF Detection", (2010). Thesis, Submitted
Bibliography: University of Maine Ph.D. Dissertation

Web/Internet Site

Other Specific Products

Product Type:

Audio or video products

Product Description:

Two videos were produce for clean room fabrication techniques. One for surface acoustic wave devices and one for microhotplate devices.

Sharing Information:

This video is used to train new students in the clean room.

Contributions

Contributions within Discipline:

The goal of this project was to investigate the feasibility of a sensor system to detect and identify the composition and concentration of fluorinated volatile organic compounds (VOCs). The targeted system should be small, robust, compatible with metal oxide semiconductor

(MOS) technology, cheap, if produced in large scale, and have the potential to be versatile in terms of low power consumption, detection of other gases, and integration in a portable system. The fluorinated VOC sensor system studied in this project has three major elements that could be integrated into a microreactor flow cell: a temperature-programmable microhotplate array/reactor system which serves as the basic sensor platform; an acoustic wave sensor, which was hypothesized to detect material removal (instead of deposition) to verify and quantify the presence of fluorine; and an intelligent method, 'support vector machines,' to analyze the complex and high dimensional data furnished by the sensor system. In addition, this project was designed to provide a multidisciplinary graduate education environment which involved chemical, electrical engineering, advanced data processing. Integration with existing IGERT and GK-12 programs further broadened graduate experiences and also extended educational benefits to high school students and teachers.

The specific research and education outcomes proposed were:

Microhotplate reactor/sensor array
?Develop fabrication methods and characterize arrays
?Develop CVD sensor material deposition methods for metal oxides and supported transition metals
?Test sensitivity to fluorocarbons and compare to interferents such as CO
?Relate sensitivity of fluorocarbon sensor to activity for catalytic decomposition of the analyte to form HF which could be detected by the acoustic wave sensor

Acoustic Wave Sensors
?Model, design, and fabricate quartz based surface acoustic wave (SAW) sensor that responds to HF by substrate material removal
?Characterize material removal mechanism and optimize sensitivity
?Investigate different quartz orientations and influence of metallic film on sensor performance.

Data analysis using support vector machines
?Develop SVM methods for predicting microhotplate sensor response to fluorocarbons and interferents
?Integrate microhotplate sensor array, acoustic wave sensor, and data analysis

Broader Impacts
?Educate graduate students in chemical sensor science and engineering
?Disseminate results via publications and conferences
?Provide research opportunities for underrepresented groups [one female (More)]
?Provide research opportunities for undergraduate students and high school teachers
?Provisional Patent Application, Serial #61-315,068 (Surface Acoustic Wave Resonator With an Open Circuit Grating for use in a High Temperature Environment)

The outcomes of this project successfully addressed the goals related to individual components of the sensor system. In addition, the interactions among our multidisciplinary team resulted in the investigation of new topics meaningful to the targeted research such as distributed sensor networks, novel wireless sensor control, and acoustic wave modeling for heavy electrodes. Some of the originally proposed research targets are still on going efforts, such as optimization of materials for sensing/decomposing fluorinated VOCs, integration of system components, potential for commercial applications, publications and dissemination, student thesis writing, provisional patent processing with envisioned commercial application by a University of Maine spin-off company.

The infrastructure and techniques developed through this project have also enabled new research in related sensor applications and materials development. For instance, the multidisciplinary team at the University of Maine has applied the microhotplates developed under this project as calorimeters with nanojoule sensitivity (50 nJ/K) to measure reaction rates on catalytic materials, and also applied acoustic wave modeling developed under this project to high temperature sensor application.

The above-mentioned accomplishments are detailed below, and the cited references have been provided as supplementary information in an attached PDF file.

Methods for fabricating microhotplate sensor arrays were developed in UMaine's new clean room facility [More 2007, http://www.library.umaine.edu/theses/pdf/MoreD2007.pdf]. The sensors have heating and cooling time constants of less than one millisecond and can be operated at temperatures up to 500?C. Selective deposition of sensor materials was accomplished using chemical vapor deposition systems developed as part of this project. Sensors were tested for sensitivity to a range of gas analytes, and methods for differentiating between analytes were explored [Clark 2007]. It was shown that a rapid pulsed temperature programming method, combined with a principle component analysis based on competing surface reaction rates could be used to distinguish between gas analytes such as fluorine-containing compounds and alcohol interferents [Wheeler 2008].

Two new methods for extracting data from microhotplate based sensors were investigated. The first method involved rapidly heating and cooling the sensing film and observing the film conductance at a nominal temperature. Kinetic reaction constants were derived by fitting an exponential curve to the resulting film conductance [Winchenbach 2007]. The second method treated the microhotplate based sensor as a semiconductor. Initial tests showed that the conductance of the sensing film was dependent on the voltage bias of both the heater and film sense voltages. Hence it is not simply temperature that affects film properties, and it suggests an entirely new design space for microhotplates.

It was determined that the processing power necessary to control a microhotplate is relatively low and can be achieved with an embedded microcontroller. This approach has the advantage of maintaining a tighter control of timing between temperature changes and film resistivity. A further advantage is the ability to create a small and potentially battery powered sensor. On the other hand, calculating reaction constants with exponential curve fitting and processing the results with artificial neural networks requires vastly more processing power than an embedded processor can provide. A distributed system combines the most desirable properties of each processing environment and utilizes wireless communication between a portable sensing unit and a fixed processing unit.

Platinum electrode surface acoustic wave (SAW) resonators on multiple quartz orientations were developed for HF sensing for process monitoring applications and as a decomposition product of fluorine-containing compounds, when combined with microhotplate arrays [Meulendyk 2010]. Platinum electrodes are utilized because of their resilience to HF and their favorable catalyzing properties in the decomposition of fluorine containing compounds. However, platinum electrodes on quartz substrates required modeling and characterization to allow the design of improved HF SAW resonator sensors.

A scalar network model was used to optimize the SAW transducer and reflector geometries using the combined finite element method and boundary element method (FEM/BEM) extracted parameters. FEM/BEM was also used to calculate the mass sensitivities of a 193 MHz resonator on ST-X quartz and a 305 MHz resonator on ST-90?X quartz, which were determined to be 58x10^9 Hz-cm^2/g and 225x10^9 Hz-cm^2/g, respectively.

Scalar potential theory was used to investigate the SAW guiding phenomenon in grating structures composed of platinum electrodes. This technique revealed that acoustic energy leaks from the active area of a Pt-electrode resonator to the busbars of a short circuit grating. Based on the outcomes of this study, the resonator structure was redesigned to use open circuit gratings, thus avoiding the energy leakage to the busbars. The new devices have half of the original losses and the quality factor increased by 56%. In addition, scalar potential theory was used to filter out spurious transverse waveguide modes that interfere with the resonator response. Fabrication of the SAW resonators required the development of processes for substrate cleaning, photolithography, metal deposition, and metal liftoff that are unique to the equipment and materials available in the clean room facilities at the University of Maine. These procedures are documented in writing and as a video to instruct future clean room users in efficient microfabrication techniques.

Testing the SAW sensors in the presence of HF and other analytes requires the use of a gas delivery system, control software, temperature-controlled oven, gas test cell, and device packaging, all of which were custom designed and automated. The platinum-electrode SAW resonators on ST-X and ST-90?X quartz were exposed to 1-18 ppm HF, and exhibited signal-to-noise ratios from 2 to 4 and 5 to 12, respectively. Additionally, the ST-90?X resonator exhibited signal-to-noise ratios less than 2 for many potential interferents, including fluorinated compounds. Based on experimental observations, this work determined, for the first time, that the formation of a condensed liquid layer on the SiO2 substrate is the dominant effect in detecting the presence of HF, rather than SiO2 removal. This observation was also corroborated by theory.

This project developed efficient algorithms for data collection and event processing with regard to continuous chemical phenomena such as toxic clouds [Jin 2008 ACM Proceedings]. In particular, the work focused on estimation of such phenomena and on detecting and tracking the boundary of toxic clouds.

In sensor networks, sensor motes have to work in a cooperative way to estimate underlying phenomena. To estimate the spatial properties of underlying phenomena, the local processing of aggregation queries is important. For continuous phenomena, also known as spatial fields, additional estimation methods are required to process the sensor readings in order to generate the estimation results. Estimation methods, however, are computationally intensive, even when computed in a centralized setting. Processing the additional estimation methods faces more difficulties in the energy and bandwidth constrained environment of sensor networks. In [Jin 2008 IEEE], Guang Jin and Dr. Nittel introduced the SWOP (Spatial Window query Over Phenomena) approach, which breaks the entangled link between estimation results and sensor readings, and conserves the network resources by compressing the data extracted from a sensor network. The SWOP processes spatial window queries on a continuous phenomena based on Gaussian kernel estimation. The key of the approach is using Hermite series to approximate the Gaussian kernel function; as a result, the number of messages transmitted in the networks could be relaxed by logarithmic operation. Hence, a large amount of network resources can be saved, while the network still returns comparable estimation results with neglectable errors.

The group tested SWOP in different settings. SWOP archives the compression by grouping the sensors into sub clusters. Therefore, the clustering algorithm plays an important role in SWOP, the more dense clusters are found, the higher the compressing rate can be achieved. HEED was chosen as the clustering algorithm for SWOP since HEED is more appropriate for mobile settings. HEED, on the other hand, can only return a ``randomized' clustering layout. Therefore, we measure the mean, min and max data size as illustrated. Compared with centralized solutions, SWOP requires significantly less data extracted from sensor networks. To get the same quality of estimation results as the original phenomenon, the ordinary distributed solution needs much more data to represent the estimation result. For a small data set, SWOP only requires as half as data required by centralized solution. SWOP, however, is designed for a larger sensor networks. For those cases, SWOP can compress the data up to 1/4 as required by centralized solution, and thus, save communication cost significantly.

Contributions to Other Disciplines:

The multidisciplinary approach of this project impacts a number of disciplines:
Chemistry and chemical engineering
Electrical engineering
Computer engineering
Spatial engineering
Material science

Contributions to Human Resource Development:

This work impacted undergraduate and area high school education through involvement of REU and GK-12 students.
The IGERT student obtained a certificate in sensor technology independent of his Ph.D. degree requirements.

Contributions to Resources for Research and Education:

Contributions Beyond Science and Engineering:

Conference Proceedings

Meulendyk, BJ;Wheeler, MC;Segee, B;da Cunha, MP, Generalized and pure shear horizontal SAW sensors on quartz for hydrogen fluoride gas detection, "OCT 28-31, 2007", 2007 IEEE ULTRASONICS SYMPOSIUM PROCEEDINGS, VOLS 1-6, : 480-483 2007

Jin, G;Nittel, S, UDC: A self-adaptive uneven clustering protocol for dynamic sensor networks, "DEC 13-15, 2005", MOBILE AD-HOC AND SENSOR NETWORKS, PROCEEDINGS, 3794: 897-906 2005

Categories for which nothing is reported:

Any Web/Internet Site

Contributions: To Any Resources for Research and Education

Contributions: To Any Beyond Science and Engineering

Correlation of Reactivity to Sensor Selectivity for Fluorocarbon Detection using Microhotplate Arrays

Aaron Clark[1], Mauricio Pereira da Cunha[2,3], Bruce Segee[2], and M. Clayton Wheeler[1]

[1]*Department of Chemical and Biological Engineering, University of Maine*
[2]*Department of Electrical and Computer Engineering, University of Maine*
[3]*Laboratory for Surface Science and Technology, University of Maine*

A hybrid microsensor system consisting of an array of microhotplate reactors/sensors and a complimentary surface acoustic wave (SAW) sensor is being developed for selective detection of fluorocarbon compounds using tetrafluoroethane (R134A) as a model compound. The microhotplate sensors simultaneously detect and decompose the analyte while the SAW depends on exposure to the hydrolysis products of the R134A for its sensing mechanism. This paper focuses on comparing the microhotplate sensing and catalytic reaction mechanisms.

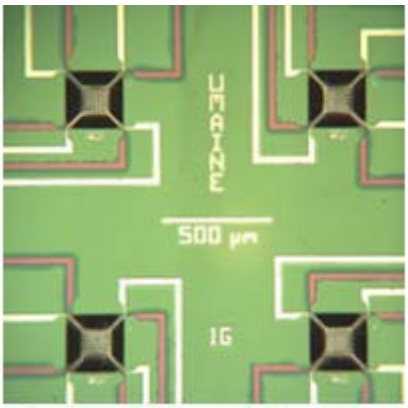

Figure 1. Four element microhotplate array

The microhotplate devices, shown in Fig. 1, were fabricated in the clean room at the University of Maine's Micro Instruments and Systems Laboratory and each consists of a suspended sandwich of multiple SiO_2/SiN layers that separate two platinum circuit element layers: 1) an embedded serpentine heater and 2) surface electrical contacts. Since microhotplates are thermally isolated from the substrate by silicon micromachining, they can be heated and cooled over a range of more than 400 °C at rates of over 10^6 °C per second. Semiconducting SnO_2 and catalytically active platinum are selectively deposited on the microhotplates using chemical vapor deposition with precursors tin tetrabutoxide and platinum acetylacetonate. Measuring the electrical response of the material over a range of operating temperatures is a way to improve the selectivity of metal oxide sensors that is commonly referred to as temperature programmed sensing (TPS).

In TPS the reaction kinetics control the surface concentrations of species such as oxygen and hydroxyl. These surface concentrations significantly affect the electrical conductivity of the sensing film. The rates depend on the sensor material as well as the temperature. The sensor sensitivity and selectivity of SnO_2 (with and without Pt catalyst doping) are correlated to the decomposition rate of R134A measured using a microreactor catalyst characterization system.

Correlation of Reactivity to Sensor Selectivity for Fluorocarbon Detection using Microhotplate Arrays

Aaron Clark

Advisor: M. Clayton Wheeler

Chemical & Biological Engineering

THE UNIVERSITY OF MAINE

Fluorocarbon Sensor

- Tetrafluoroethane (R-134a) as a model compound
- Sensing techniques
  - Microsensors/microreactors being developed as one element of a hybrid sensor platform
  - Temperature programmed sensing (TPS) for analyte identification (selectivity)
- Understanding TPS
  - TPS spectra depend on unique surface reactions
  - Corellating reaction rates to sensor response using bulk catalysts
    - Temperature programming
    - Gas chromatography
    - Mass spectrometry

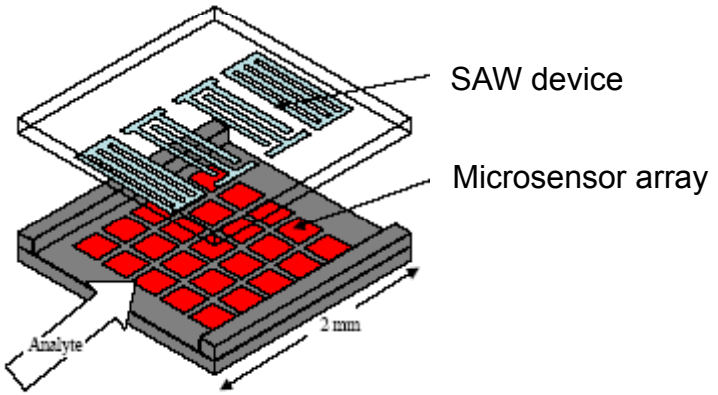

Microhotplate Gas Sensors

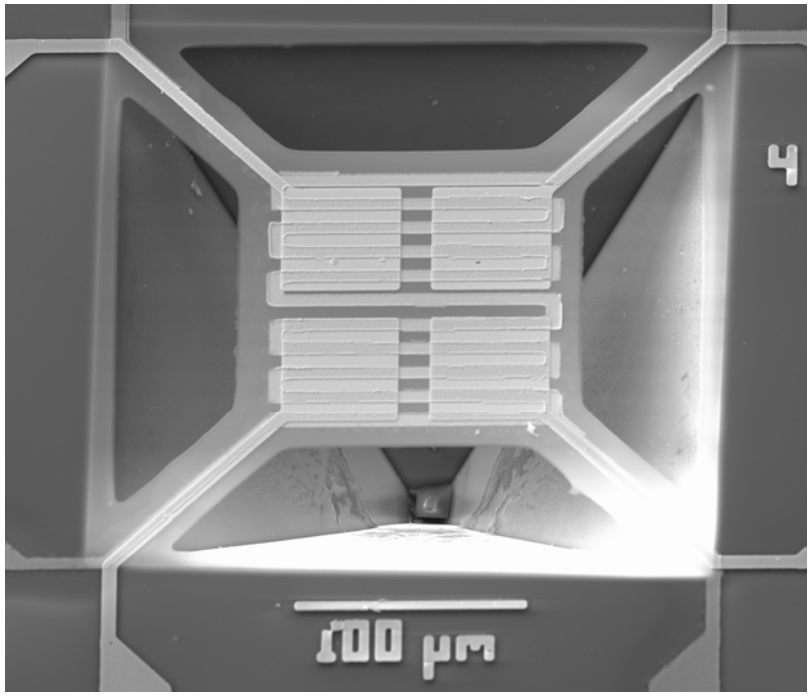

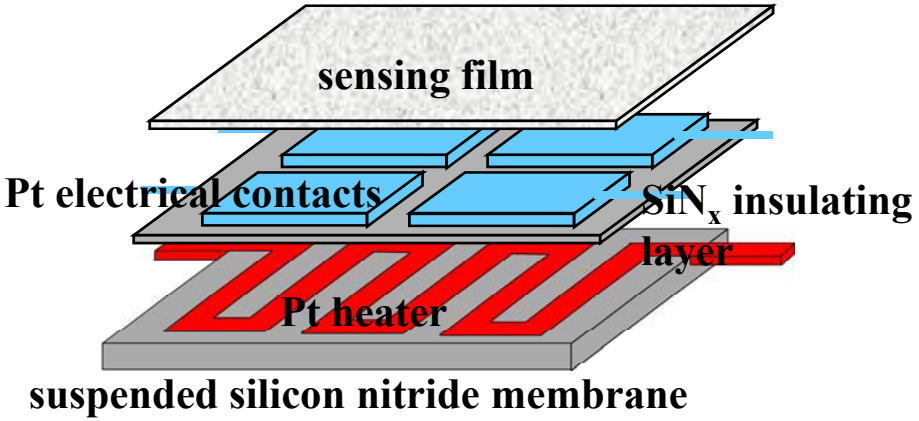

- Electrical contacts: Sensing film resistance measurement
- Heater: Temperature control and measurement (resistance change)
- Micromachined: Thermally isolated
  - Rapid heating and cooling

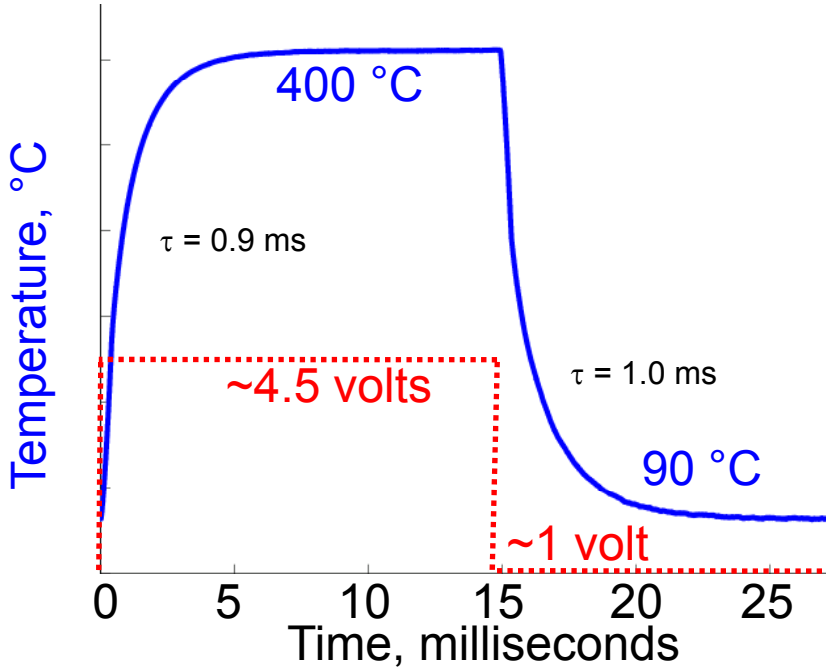

Microsensor Fabrication

UMaine's Laboratory for Surface Science and Technology

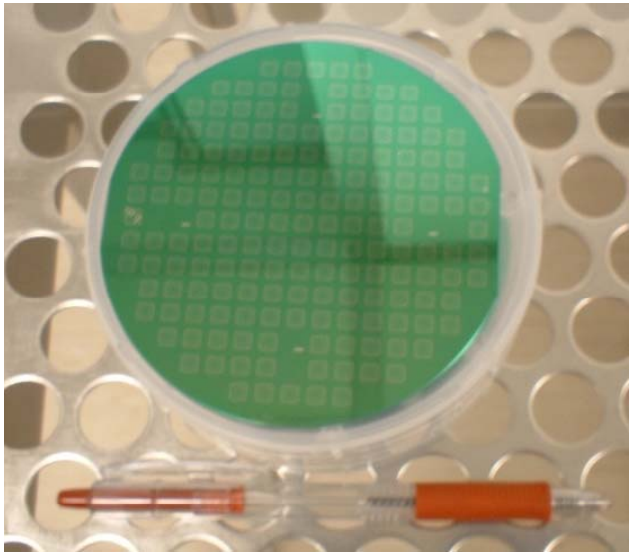

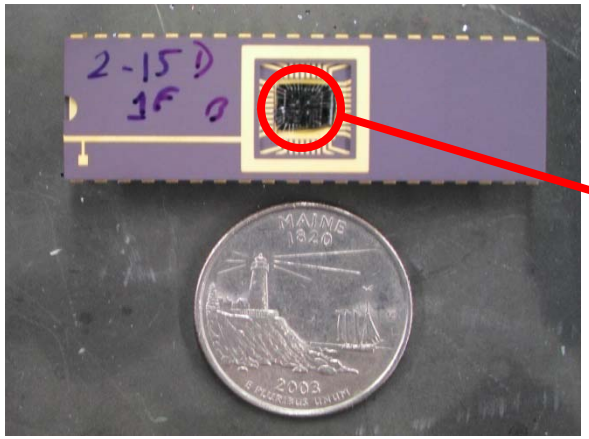

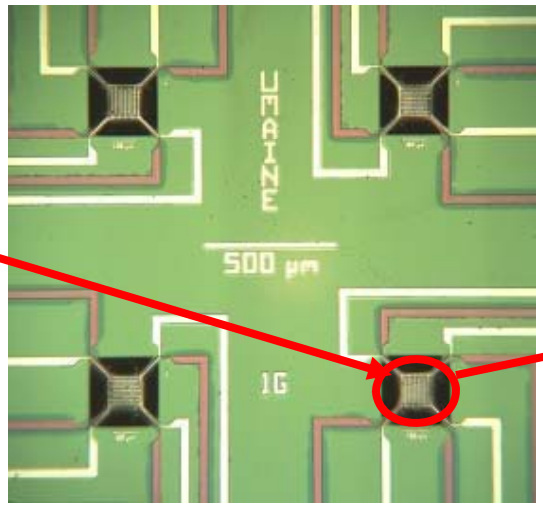

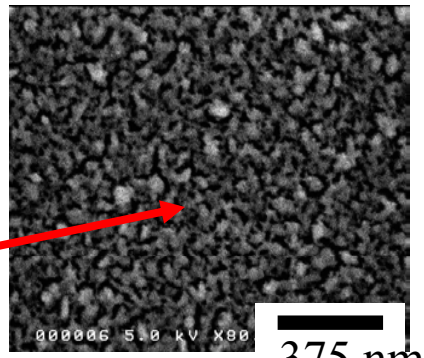

375 nm

Materials Deposition: Spin Coating vs. CVD

Sol Spin Coating

- Sb-doped SnO_2
- 15% aq. Solution
- 2000 rpm
- All four devices coated with the same material

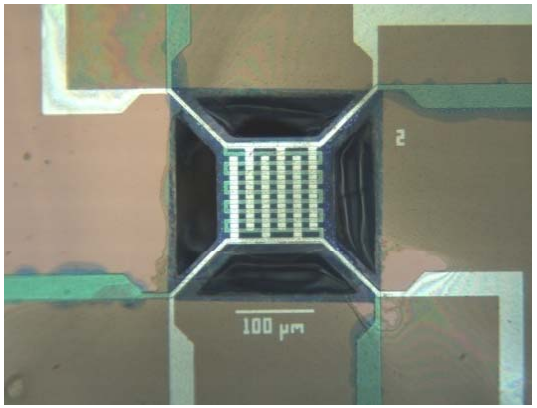

Chemical Vapor Deposition

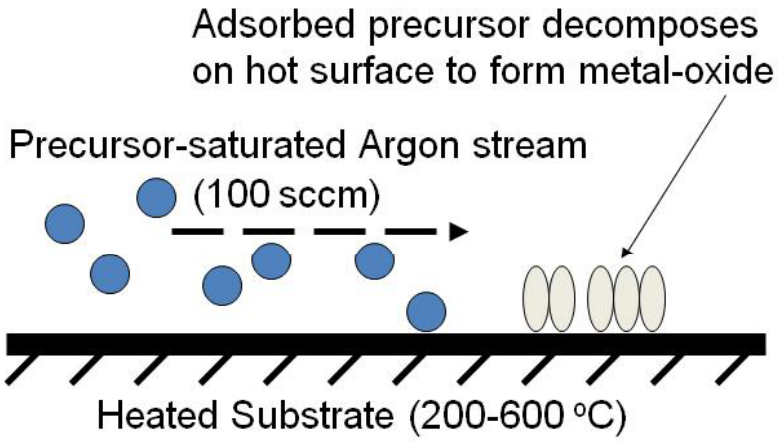

Precursors (1:5 - 1:20)

Tin butoxide (SnO_2)

Titanium isopropoxide (TiO_2)

Platinum acetylacetonate (Pt)

Reactor Pressure

0.6 – 20 torr

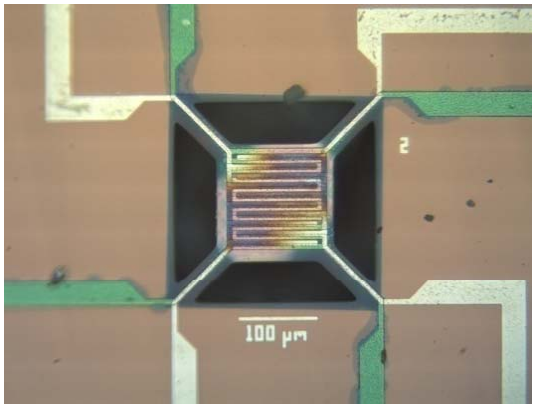

Metal-Oxide Sensing Materials

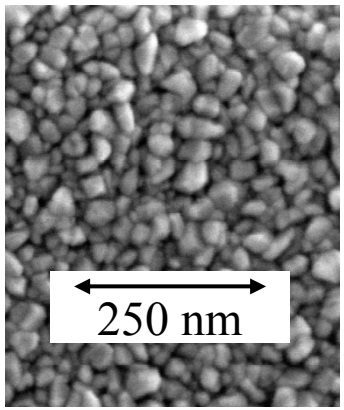

SnO_2 film

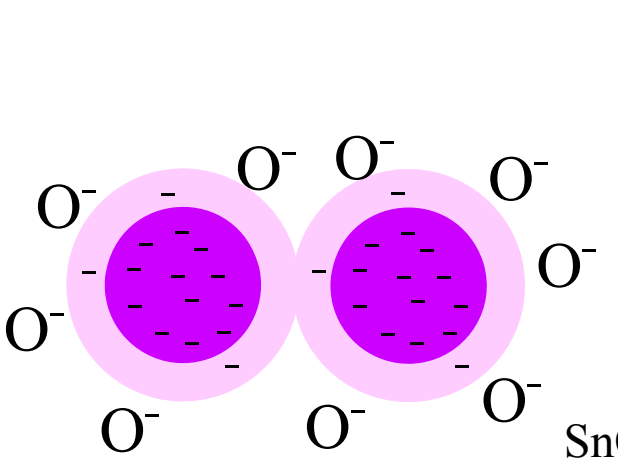

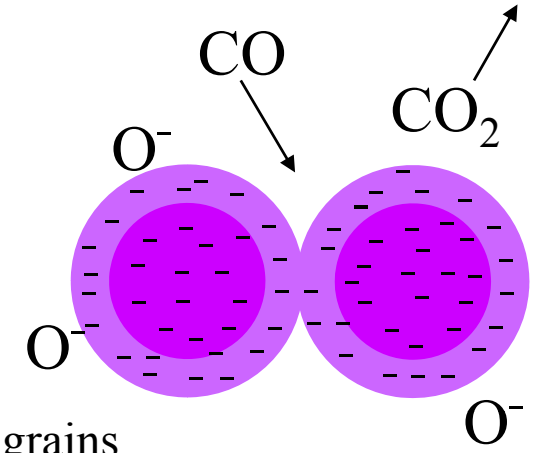

SnO_2 grains

- Electrical conductivity is affected by adsorbates
- Sensing performance depends on:
  - Film composition (selectivity and sensitivity)
  - Film micro-structure (sensitivity)
- Reaction mechanisms can also be modified by using surface-dispersed catalysts
  - Example: Pt increases the sensitivity of SnO_2 to CO

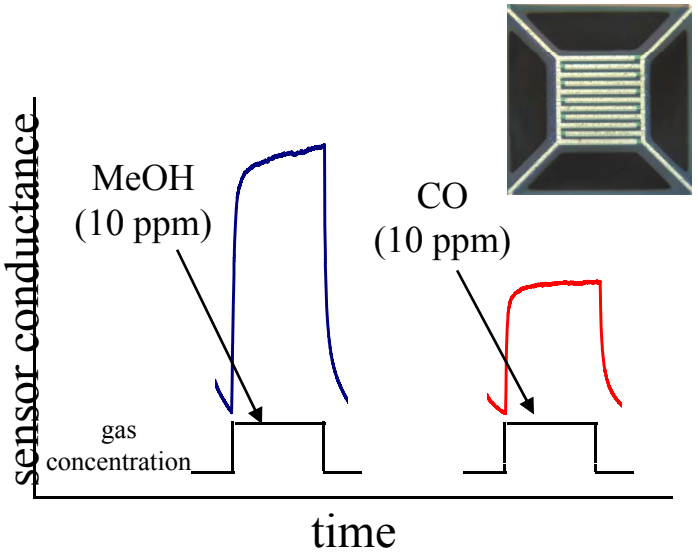

Sensor Test System

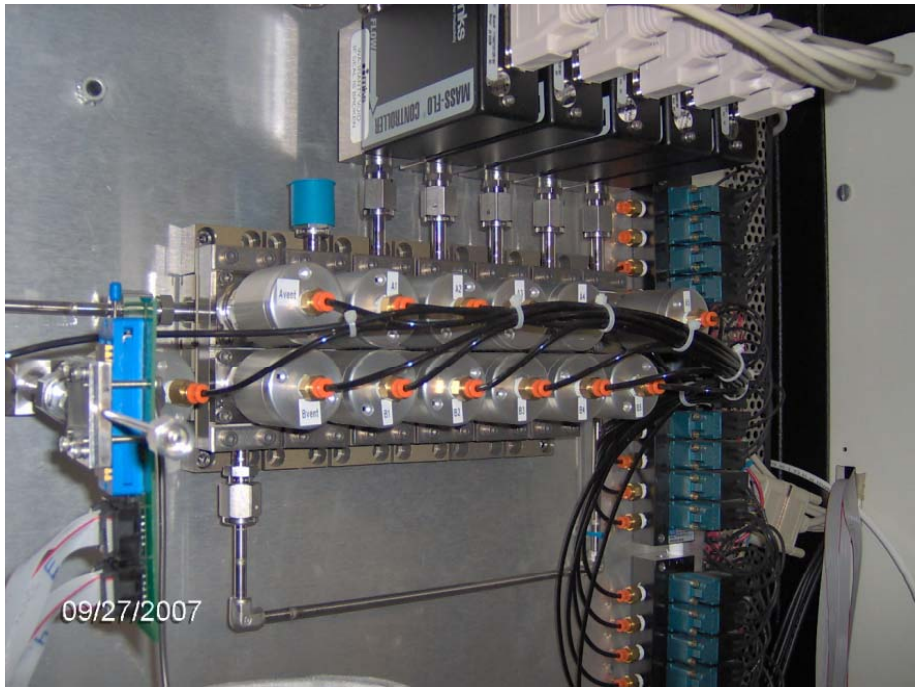

- Automated
- 4 test gases (methanol)
- Zero or humid air
- Up to 2000 sccm
- Space time < 1 sec

Isothermal Sensor Response: Methanol vs. R-134a

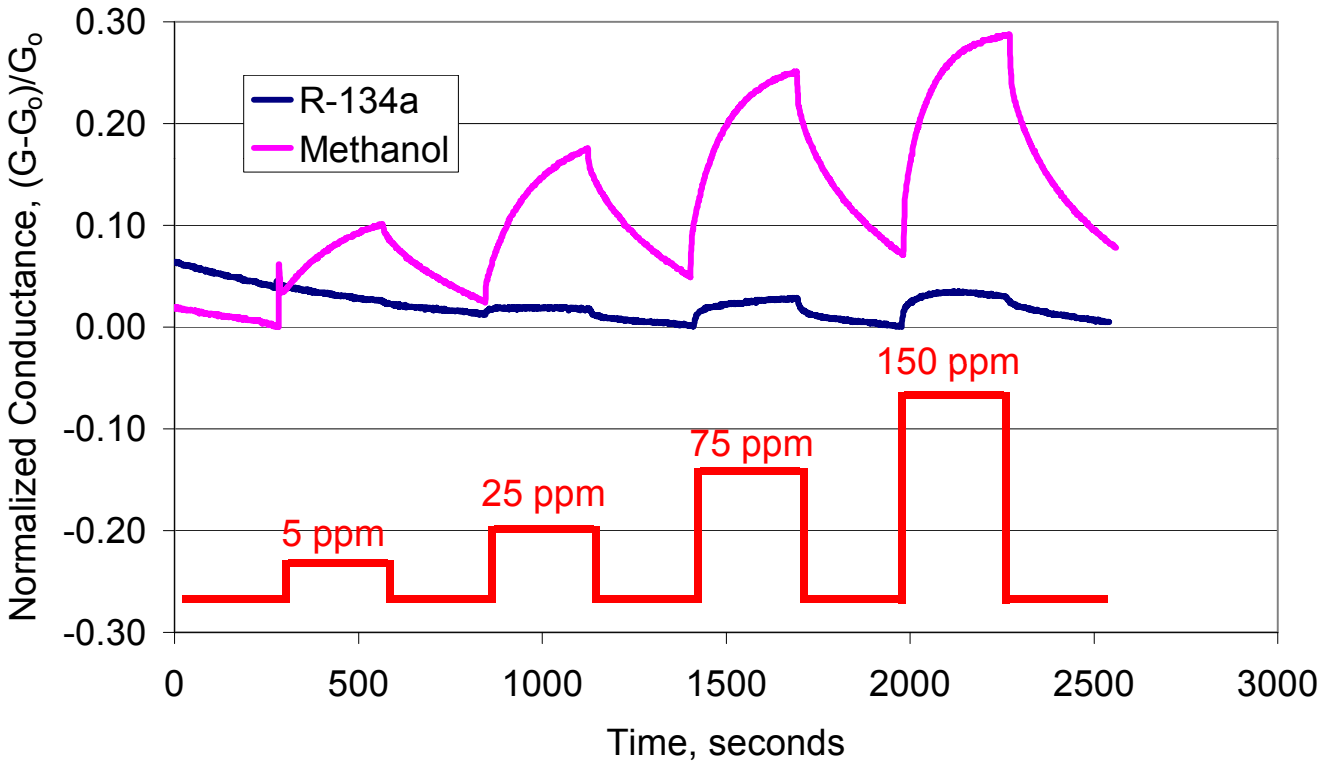

- 200°C
- 5 minute exposures
  - R-134a & methanol
  - 5, 25, 75, 150 ppm
- 5 minutes dry air
- Constant total flow rate (120 sccm)

Improving Selectivity: Temperature Programmed Sensing

"Simple" Kinetic Mechanism: CO Oxidation

$$\frac{d\theta_{CO}}{dt} = \Gamma_{CO} S(1-\theta_{CO}) - k_r \theta_{CO}\theta_O - k_{des,CO}\theta_{CO}$$

$$\frac{d\theta_O}{dt} = 2\Gamma_{O_2} S(1-\theta_{CO}-\theta_O)^2 - k_r \theta_{CO}\theta_O - k_{des,O_2}\theta_{O_2}^2$$

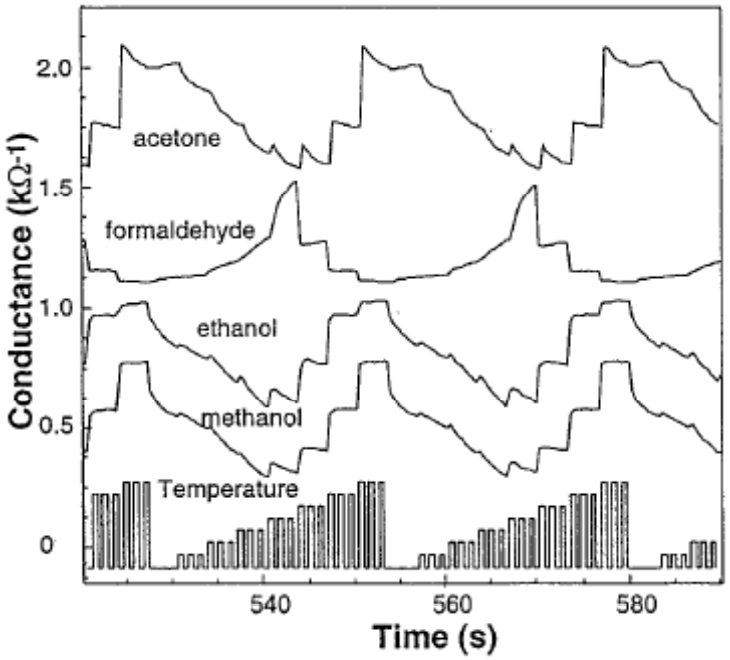

S. Semancik and R. Cavicchi, Acc. Chem. Res., 31(5), 279-287 (1998).

- Temperature ramp 20-450 °C
- Baseline conductance measurement
- Non-linear programming can even differentiate between ethanol and methanol

Sensor Temperature Effect: R-134a

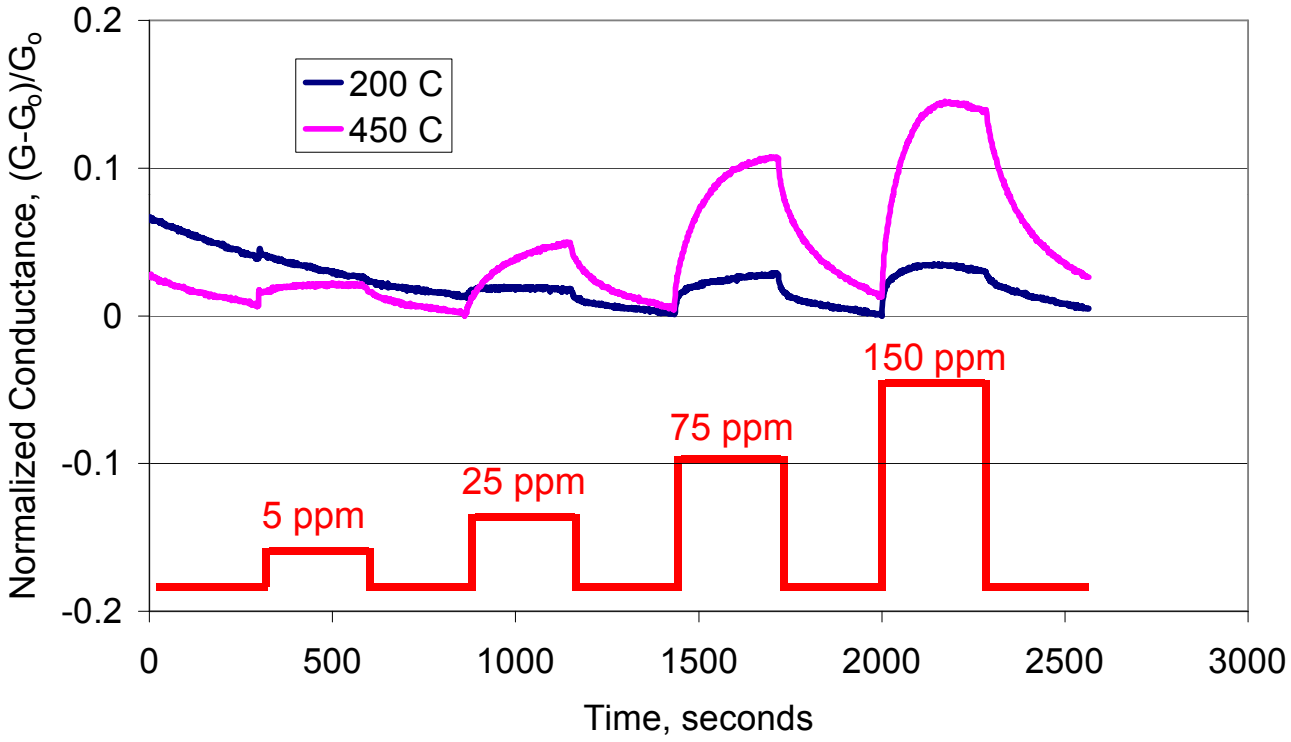

- 5 minute exposures
  - 5, 25, 75, 150 ppm
- 5 minute dry air
- Constant total flow rate (120 sccm)

TPS: Method

- Linear (stepped) temperature ramp
- 750 millisecond step times
- Conductance measurement
  - First 250 milliseconds
- Cycles 5 minutes in air
- Cycles 5 minutes in test gas

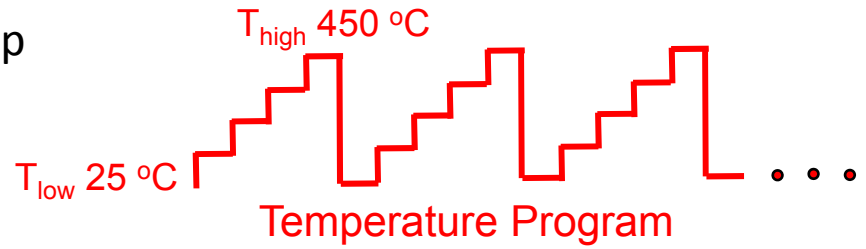

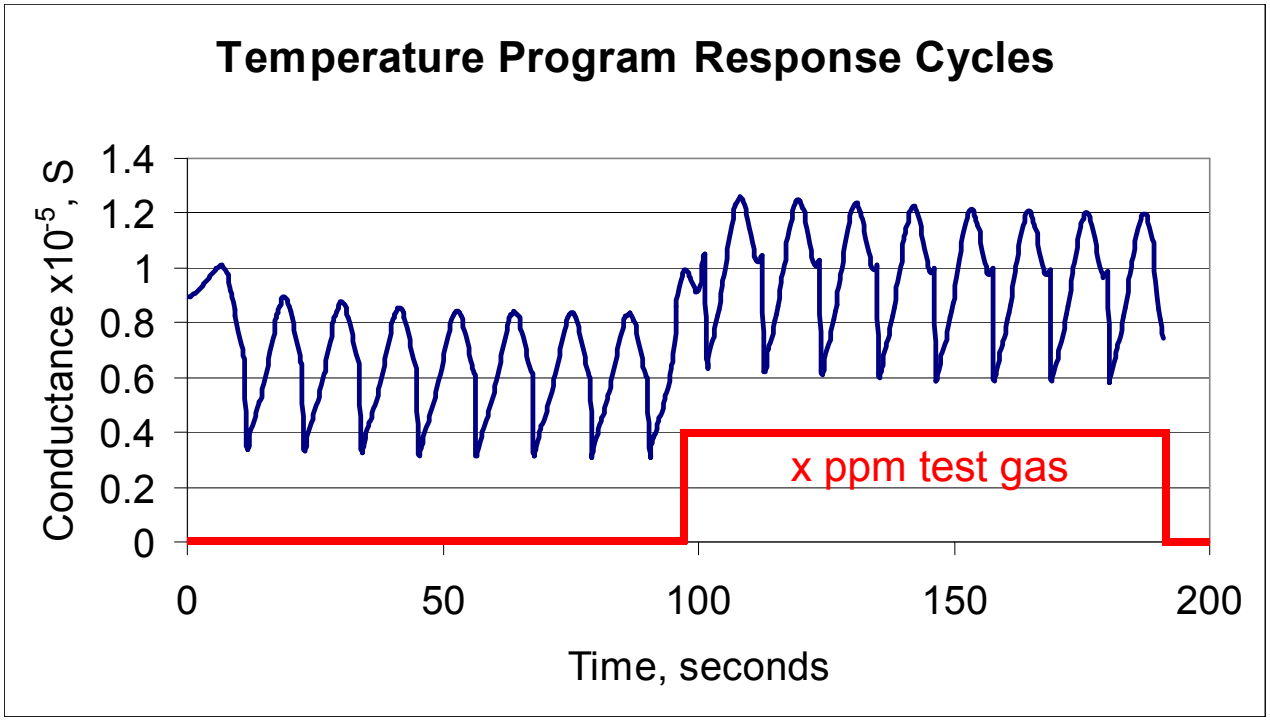

TPS: Methanol

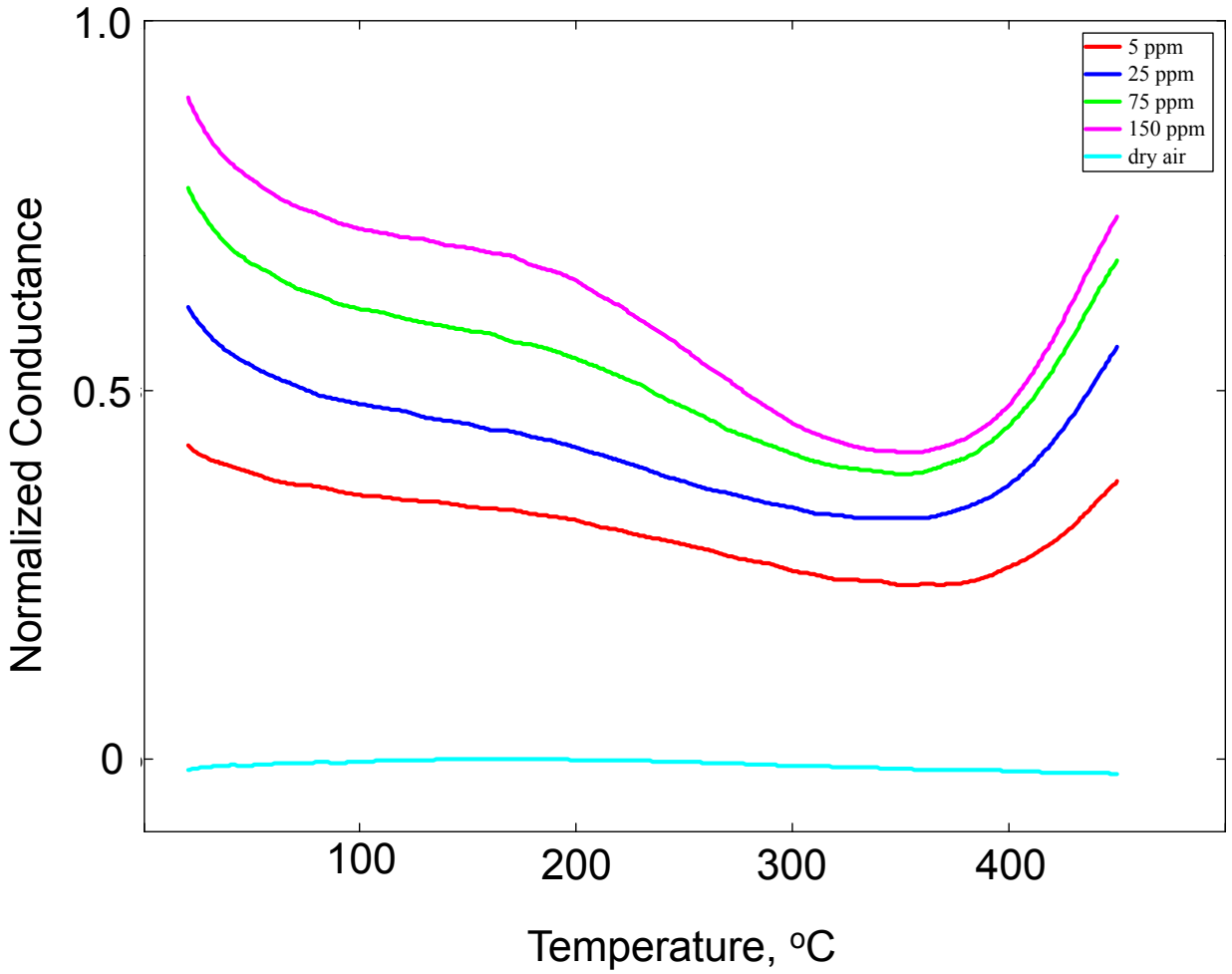

- Characteristic information
- Sensors should be sensitive at methanol concentrations less than 5 ppm

TPS: R-134a

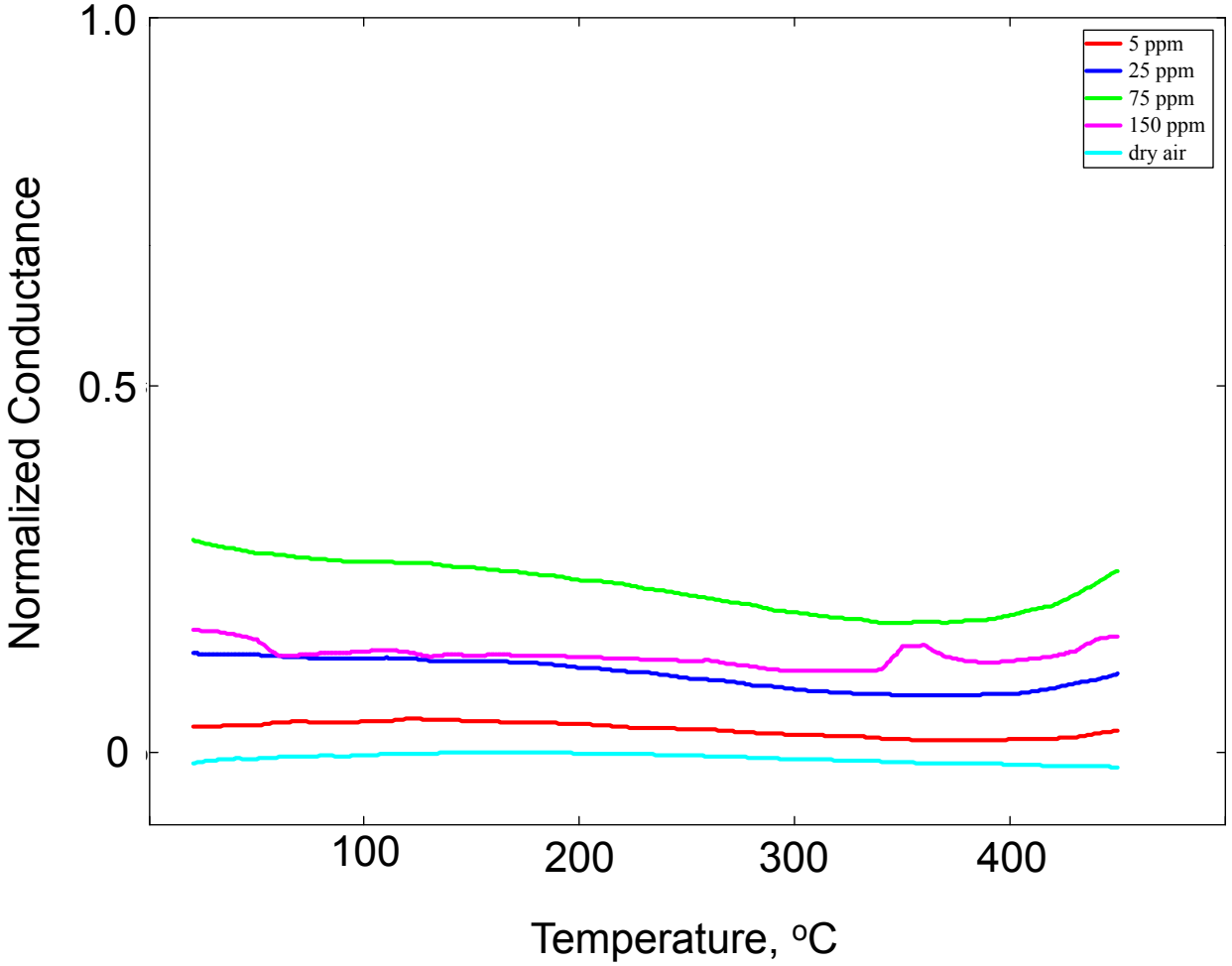

- Less sensitive than methanol
- Poisoning at high concentrations?

Packed Bed Reactor Studies

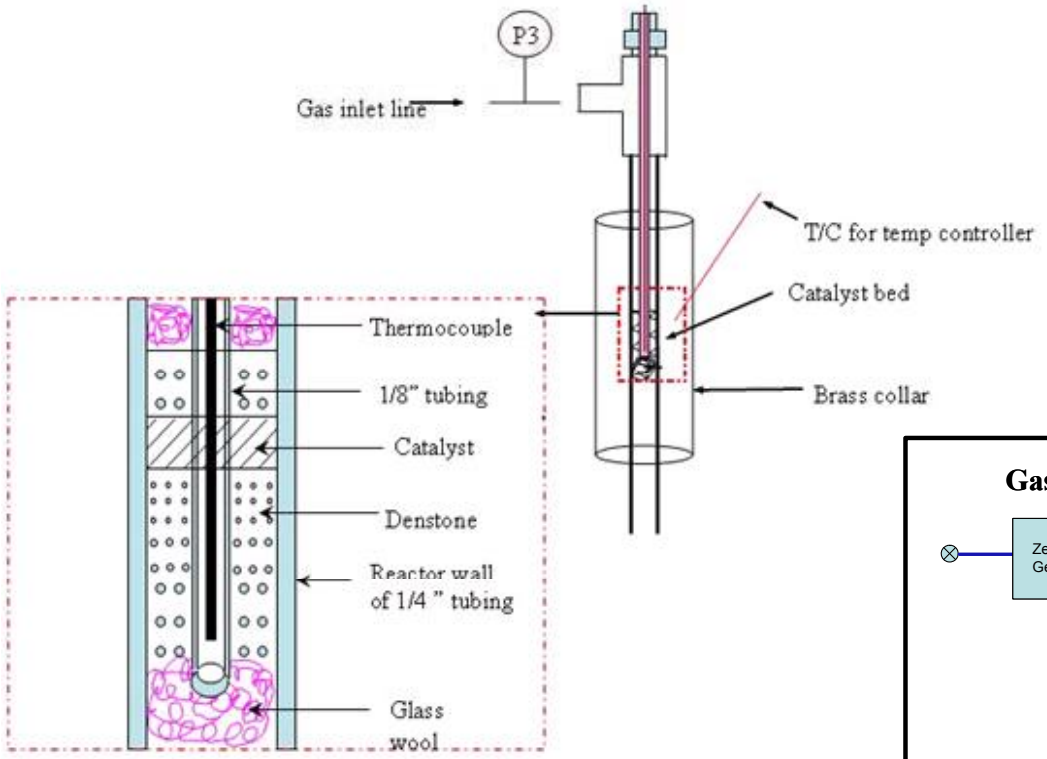

Decomposition in air

– Oxidation (above ~200 °C)

$CFH_2CF_3 + O_2 \rightarrow CF_3COOH + HF$

– Hydrolysis

$CFH_2CF_3 + O_2 + 2H_20 \rightarrow 2CO_2 + 4HF$

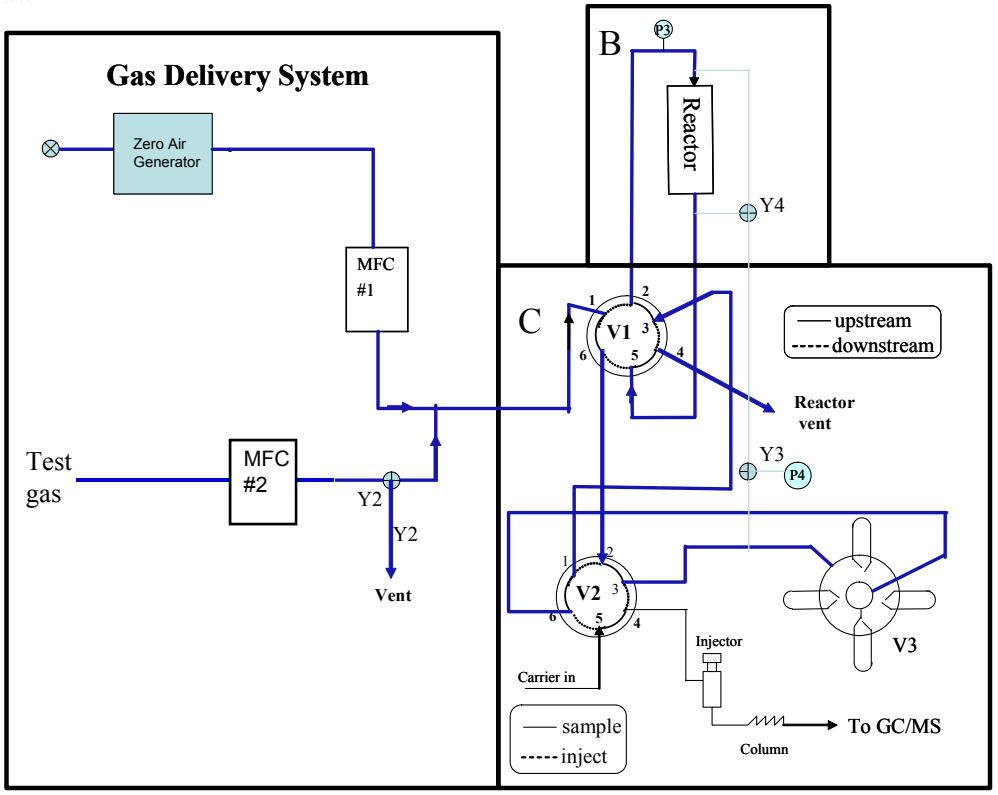

GC/MS

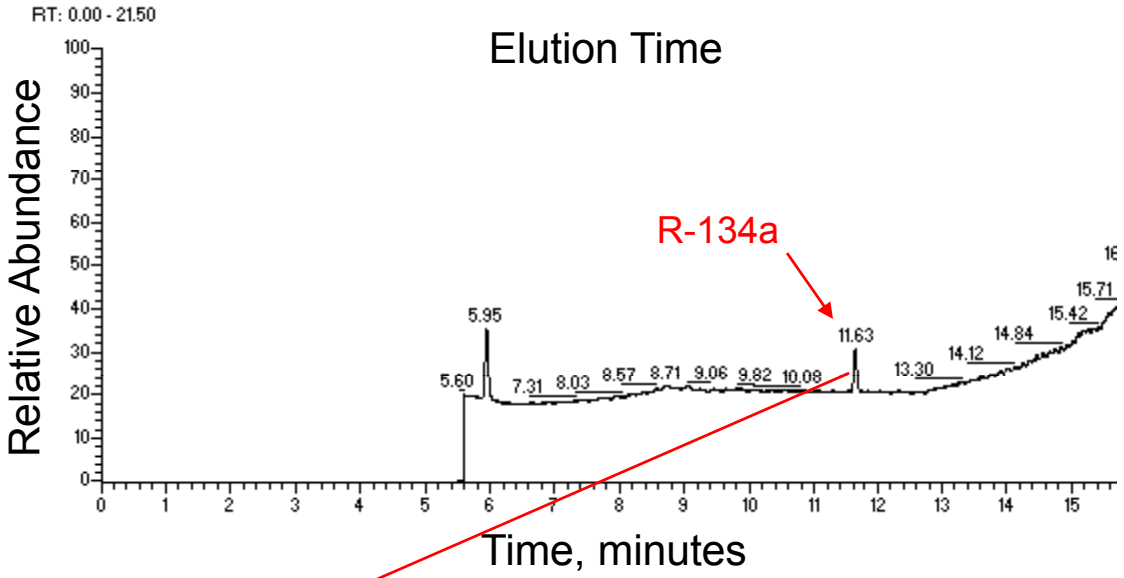
RT: 0.00 - 21.50
Relative Abundance
Elution Time
R-134a
5.95
5.60
7.31
8.03
8.57
8.71
9.06
9.82
10.08
11.63
13.30
14.12
14.84
15.42
15.71
Time, minutes

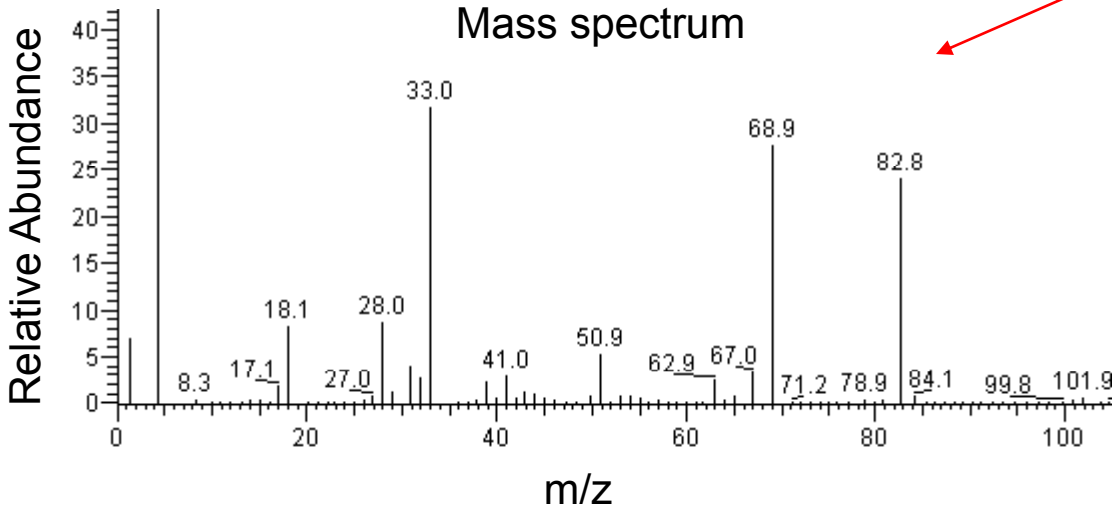
Mass spectrum
Relative Abundance
33.0
68.9
82.8
18.1
28.0
50.9
8.3
17.1
27.0
41.0
62.9
67.0
71.2
78.9
84.1
99.8
101.9
m/z


09/27/2007

Summary

- Fabricated microhotplate sensors
- Deposited materials by CVD and spin-coating
- Evaluated compatibility of SnO_2-Sb for R-134a sensing
- Developing TPS for selective identification
- Studying chemical reactivity and deactivation mechanisms

Acknowledgements

- NSF Sensors Small Team
  - Chemical and Biological Engineering
    - Clayton Wheeler
    - Daesha More
  - Electrical Engineering
    - Mauricio Pereira da Cunha
    - Bennett Meulendyk
  - Computer Engineering
    - Bruce Segee
    - Sam Winchenbach
  - Spatial Engineering
    - Silvia Nittel
    - Guang Jin
- Grant # NSF CTS-0428341
- GK-12 Grant # NSF 0538457

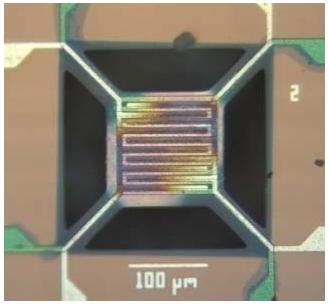

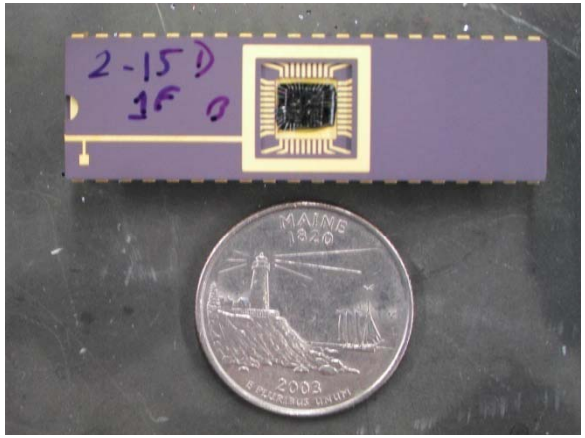

Hybrid Sensor System for Fluorocarbon Detection

M. C. Wheeler[1], D. More[1], A. Clark[1], M. Pereira da Cunha[2,3], B. Meulendyk[2], B. Segee[2], S. Winchenbach[2]

[1]University of Maine Chemical and Biological Engineering, 5737 Jenness Hall, Orono, ME, 04469, USA
[2] University of Maine Electrical and Computer Engineering
[3] University of Maine Laboratory for Surface Science and Technology

Abstract

This paper presents results of a hybrid microsensor system consisting of an array of microhotplate reactors/sensors and an integrated surface acoustic wave (SAW) sensor for detection of fluorocarbon compounds. The microhotplate sensors are designed to simultaneously decompose and detect the analyte while the SAW sensors respond to hydrogen fluoride (HF), a hydrolysis product of the analytes. Temperature programmed reaction data from the microhotplate sensor array and frequency response of the SAW are combined to provide both sensitivity and selectivity to the target fluorocarbon. Sensor fabrication, sensor performance, and sensing mechanisms are reported and discussed.

I. Introduction

Metal Oxide Semiconductor (MOS) sensors are commonly used to quantify concentrations of gases with known composition because they have high sensitivity, however, they are not selective. We are developing a hybrid sensor system to provide both sensitivity and selectivity to fluorinated hydrocarbons using tetra-fluoroethane (R134A) as a model compound. A microarray of MOS sensor/reactors is used to detect the analyte while simultaneously decomposing it to produce HF which can be detected by a surface acoustic wave (SAW) resonator.

SAW resonators have been extensively investigated for a variety of sensing applications but usually require a selective layer to make the device responsive to a specific analyte. The quartz-based SAW resonators used in this work render the use of a selective layer unnecessary, since HF reacts directly with the substrate, forming H_2O and SiF_4 [1], [2]. Previous work has revealed that the formation of a condensed liquid layer on the surface of the SAW resonator is the dominant effect in detecting the presence of HF [3].

II. Experimental

A. *Microhotplate Arrays*

The MOS sensors are silicon-based microhotplates modeled after the NIST platform [4] but are fabricated using simplified processing steps in UMaine's Laboratory for Surface Science and Technology clean room. Chips with both 4- and 10-element microhotplate arrays were fabricated beginning with commercially-obtained 4 in., SiN_x-coated Si wafers. Each individually addressable microhotplate consists of a serpentine Pt heater, a layer of insulating SiN_x, and Pt electrical contacts on the surface. The chips were surface micromachined using tetramethyl-ammoniumhydroxide and packaged in 40-pin ceramic packages. The devices can be heated to ~500°C and cooled to room temperature with time constants ≤ 1.0 ms. Catalyzed metal oxide materials, such as Pt-TiO_2 and Pt-SnO_2, were deposited using chemical vapor deposition (CVD) as well as spin-on methods. Fig. 1 shows a 4-element array fabricated at UMaine.

B. *Surface Acoustic Wave HF Sensor*

Two-port pure shear horizontal (SH) SAW resonators on ST-cut quartz (0°, 132.75°, 90°) were fabricated using platinum thin film electrodes deposited in the UMaine clean room facilities. Fig. 2 shows two SAW resonators inside a low volume test cell (≈ 1 ml) used in gas delivery experiments. The resonators are mounted on a printed circuit board (PCB) and bonded to 50Ω RF feed-throughs, which connect to the SMA pins via microstrip transmission lines on the opposite side of the PCB.

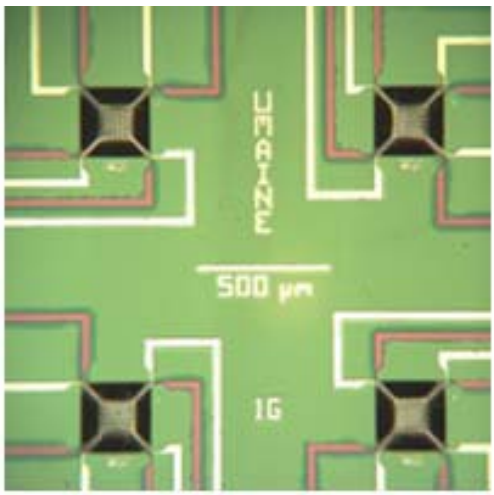

Figure 1. *4-Element microhotplate array.*

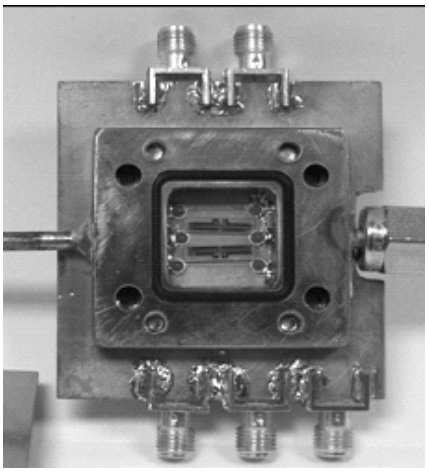

Figure 2. SAW resonators in test cell.

C. *Sensor Test System*

An automated gas delivery system is used to dilute up to four analyte mixtures with either dry or humid zero air and deliver them to a test cell at total flow rates of 20 to 2,000 sccm. The test cell in Fig. 2. is designed to allow the microhotplate array to be positioned in close proximity (<1 mm) opposite the SAW. The flow characteristics of the cell were measured experimentally, and it was determined to behave as a well-mixed system. Flow rates and concentrations were found to be at steady-state within 10 to 500 ms after switching gases because of the low volumes in the switching valves and test cell. The cell was enclosed in a custom, clam-shell oven to maintain the ambient temperature within ±0.08°C at temperatures ranging from 25 to 50°C. The oven is used to separate the thermal response from chemical response at this stage of the work.

A data acquisition computer is used to control the gas delivery, vary the temperature of the microhotplates, measure the resistance of the MOS films, and collect SAW response data from a network analyzer. Microhotplate resistance data can be collected at frequencies greater than 1 kHz making rapid temperature programming possible.

III. Results and Discussion

A. *R134A Detection and Decomposition*

Experiments have been conducted to compare the sensitivity of the resistance of CVD-prepared SnO_2 and Sb-doped nanoparticle SnO_2 films to both R134A and methanol at concentrations ranging from 5 to 150 ppm and temperatures from 25 to 450°C. Both materials have a higher relative sensitivity to methanol than R134A, while SnO_2 prepared via CVD using tin butoxide as the precursor was more sensitive than the nanoparticle tin oxide. At the highest concentrations, the sensitivity to R134A decreases after just a few minutes of exposure. To explore the R134A sensing and decomposition mechanisms, bulk MOS materials are currently being used in a microreactor coupled to a gas chromatograph mass spectrometer. These experiments are critical to understanding the interactions between the combined response of the hybrid sensor system.

B. *HF Detection by SAW*

During gas phase HF exposure to the SH SAW resonator, the dominant sensing mechanism reflects the detection of a condensed liquid layer on the SiO_2 surface. At HF concentrations ranging from 1 ppm to 18 ppm, the resonator responds to the changing state of the condensed liquid layer with clear frequency shifts within minutes of exposure. Permanent frequency shifts in the SAW response are observed due to the etching of SiO_2 after the evaporation of the liquid layer when HF is removed from the test gas for longer than 2 hours. As indicated in Fig. 3, these permanent shifts are about 75% smaller than the frequency shifts due to the presence of the condensed liquid layer for each HF exposure.

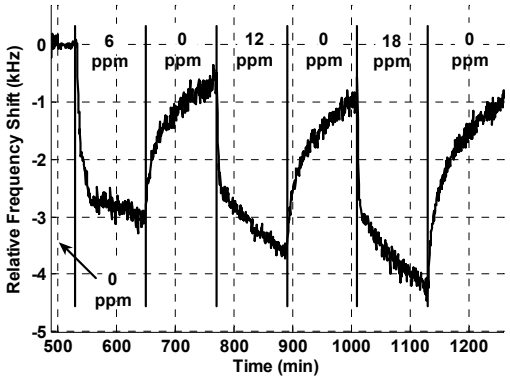

Figure 3. Frequency response of pure SH SAW resonator to HF in 100 sccm dry air at 35°C. Operating frequency: 293.9 MHz.

Acknowledgment

This work has been funded by the National Science Foundation grant #CTS-0428341.

References

[1] P.J. Holmes, J.E. Snell, "A vapour etching technique for the photolithography of silicon dioxide," Microelectronics and Reliability, 5 (1966) 337-341.

[2] C.R. Helms, B.E. Deal, "Mechanisms of the HF/SiO_2 vapor phase etching of SiO_2," Journal of Vacuum Science and Technology A, 10 (1992) 806-811.

[3] B. J. Meulendyk, M.C. Wheeler, B. Segee, and M. Pereira da Cunha, "Generalized And Pure Shear Horizontal SAW Sensors On Quartz For Hydrogen Fluoride Gas Detection," Proceedings of the IEEE International Ultrasonics Symposium, 2007.

[4] J.S. Suehle, R.E. Cavicchi, M. Gaitan, and S. Semancik, "Tin oxide gas sensor fabricated using CMOS micro-hotplates and in-situ processing," IEEE Elect. Dev. Lett., vol 14, 118-120, 1993.

Hybrid Sensor System for Fluorocarbon Detection

M.C. Wheeler, D. More, A. Clark
Dept. of Chemical and Biological Engineering
M. Pereira da Cunha, B. Meulendyk, B. Segee, S. Winchenbach
Dept. of Electrical and Computer Engineering
University of Maine, USA.

Problem Description

- **Fluorinated volatile organic compounds are a class of compounds** that represent a threat to human health through environmental pollution or chemical attacks.
- **Integration of a microhotplate sensor array, surface acoustic wave (SAW) devices, and neural networks** target the selective identification of this class of compounds in low concentrations.

Microhotplate

- Micromachined silicon device
- Low thermal mass, fast temperature response
- Metal oxide sensing materials deposited via chemical vapor deposition

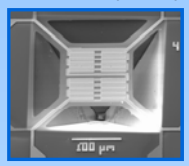

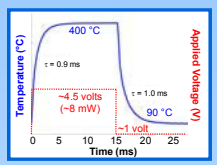

Response is related to individual species surface coverages, which are controlled by fundamental rates.

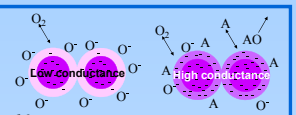

$$\frac{d\theta}{dt} = r_{ads}(P,\theta,T) - r_{des}(T,\theta) - r_{rxn}(T,\theta)$$

Sensor array – detects analyte concentrations less than 1 ppm
Reactor array – decomposes analytes

Fluorocarbons+Air+H_2O

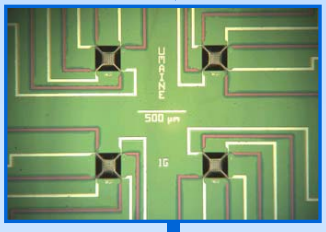

SAW Sensor

- SAW resonators, operating in a narrow frequency band, are sensitive to surface perturbations
- HF reacts directly with SiO_2, making quartz-based SAW resonators well suited for HF sensing
- In the presence of water vapor, the reaction of HF with SiO_2 has two significant effects:
  - liquid condensation
  - substrate removal

$$SiO_2 + 6HF \rightarrow H_2SiF_6 + 2H_2O$$
$$H_2SiF_6 \rightarrow 2HF + SiF_4$$

substrate removal — liquid condensation

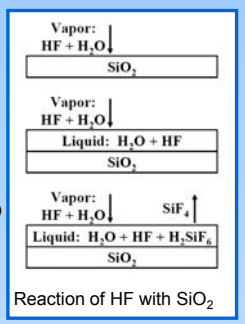

Reaction of HF with SiO_2

The formation of a condensed liquid layer was identified as the dominant HF sensing mechanism for two-port SAW resonators.

HF & other products

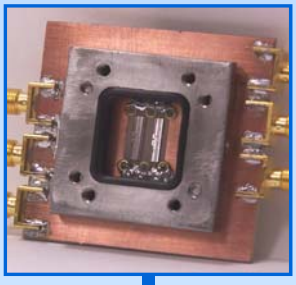

Data Processing

Data Collection and Control

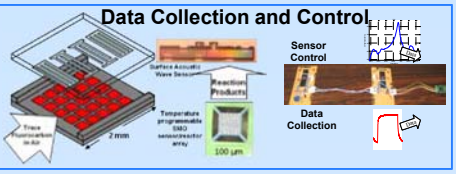

Classification and Quantitation

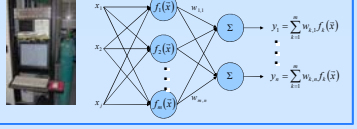

Hybrid sensor combination improves sensitivity and selectivity for fluorinated hydrocarbons. Microhotplate array allows detection and quantitation. SAW enables confirmation of fluorine functionality.

Results

Microhotplate

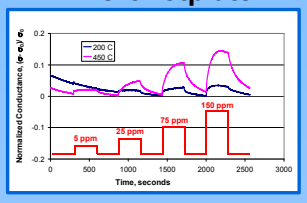

- Tetrafluoroethane (R-134A) on SnO_2

SAW Sensor

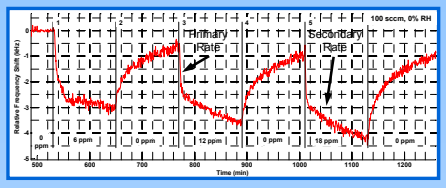

- HF concentration affects rate of frequency change
  - Primary rate – formation of liquid layer
  - Secondary rate – diffusion limited liquid layer growth and substrate etching

Data Processing

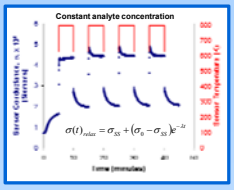

- T-Jump method cycles surface coverage between two steady-states

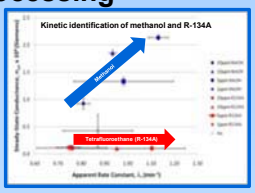

- Plot of relaxation rate parameters identifies species and quantitates concentrations

Conclusions

- Integrated hybrid sensor system
- Microhotplates act as both sensors and reactors for SAW
- New SAW sensing mechanism identified
- SAW detects HF as low as 1 ppm
- Relatively simple sensor control compatible with portable instruments
- Novel data analysis

References

J. S. Suehle, R. E. Cavicchi, M. Gaitan, and S. Semancik, "Tin Oxide Gas Sensor Fabricated using CMOS Micro-hotplates and In-situ Processing," IEEE Electron Dev. Lett. 14(3), 118-120 (1993).

A. Clark, M. Pereira da Cunha, B. Segee, and M. C. Wheeler, "Correlation Of Microhotplate Metal Oxide Sensor Response to Catalytic Fluorocarbon Decomposition Activity," 2007 AIChE Annual Meeting Conference Proceedings on CD, New York, NY, 2007.

C.R. Helms, B.E. Deal, "Mechanisms of the HF/SiO2 vapor phase etching of SiO2," Journal of Vacuum Science and Technology A, 10 (1992) 806-811.

B. J. Meulendyk, M. C. Wheeler, M. Pereira da Cunha, "Comparison of Rayleigh Wave and Surface Transverse Wave Surface Acoustic Wave Sensors on Quartz for the Detection of Hydrogen Fluoride," IEEE International Ultrasonics Symposium, New York, NY (2007).

S. Winchenbach, M. C. Wheeler, M. Pereira da Cunha, and B. Segee, "Demonstrating A Novel Approach To The Control Of Microhotplate Sensors Utilizing A Distributed Computing Approach And Numeric Modeling," 2007 AIChE Annual Meeting Conference Proceedings on CD, New York, NY, 2007.

Acknowledgements

Work funded by the National Science Foundation:
Sensor Small Team CTS-0428341
IGERT DGE-0504494
GK-12 NSF-0538457

2007 AIChE Annual Meeting Proceedings

Demonstrating a Novel Approach to the Control of Microhotplate Sensors Utilizing a Distributed Computing Approach and Numeric Modeling

Samuel Winchenbach, Department of Electrical and Computer Engineering
Dr. M. Clayton Wheeler, Department of Chemical and Biological Engineering
Dr. Mauricio Pereira da Cunha, Department of Electrical and Computer Engineering and Laboratory for Surface Science and Technology
Dr. Bruce Segee, Department of Electrical and Computer Engineering

University of Maine
Orono, Maine

Abstract

Microhotplates are sensor platforms that allow for rapid, controlled changes in temperature. Since reaction rates of chemical interactions depend on temperature one can obtain more information about chemical species present by varying the hotplate temperature and monitoring the electrical characteristics of a film applied to the hotplate. A mathematical model was created that simulates the chemical reaction in a metal oxide film in the presence of oxygen as a function of temperature. This model suggested a novel approach to controlling a microhotplate, namely, to use the temperature at which a resistance is reached rather than a resistance for a fixed set of temperatures. A sensing system was developed that demonstrated the viability of this approach in making a low cost, hand-held, portable instrument.

Introduction

A common thin film gas sensor has a semiconducting metal oxide film that interacts with gases of interest. Gas concentrations in the surrounding environment can be inferred by monitoring the electrical properties of the film. A significant drawback to this type of sensor is a lack of selectivity, i.e., different gases (possibly in different concentrations) can cause the same electrical properties to be exhibited. A technique referred to as temperature programmed sensing (TPS) takes advantage of reaction kinetics that control the surface concentrations of species, such as oxygen, thus significantly affecting the electrical conductivity of sensing film. Since surface reaction rates change with temperature, it is possible to obtain analyte-specific, multidimensional responses from a given film by varying its temperature [1,2]. We have developed a simple kinetic model to simulate sensor response, and by recognizing fundamental characteristics of the response, have developed a novel simulation and computing algorithm to reduce the dimensionality of TPS data. This demonstrates the importance of understanding the fundamental mechanisms underlying processes when implementing data analysis techniques.

A conventional approach to sensing is to choose a temperature *a priori* at which the sensitivity of the film to a target concentration of a given gas is maximized. This allows a very simple temperature control scheme, but does not address the issue of selectivity. Microhotplates are sensor platforms with very low thermal mass that allow for rapid temperature control (10^6 °C/s). Therefore, high-resolution TPS spectra spanning a range on the order of 500°C can be collected many times per minute, thus, obtaining much more

information about the gas environment.

When one looks at the underlying chemical principles that drive the metal oxide thin film gas sensor, significant insight can be obtained. Fundamentally, within the metal oxide film, contiguous grains exist, forming a conducting path across the film. As the grains interact with the ambient environment at elevated temperatures oxidation and/or reduction reactions occur that change the surface oxidation state of the film. For an n-type semiconductor such as SnO_2, the electrical resistance decreases with increasing temperature due to thermal excitation of intrinsic charge carries. The resistance increases when the film is highly oxidized because of a depletion of electron charge carriers near the surface of the film. Conversely, if oxygen is removed from the surface by reaction with reducing species, the electrical conductivity of the film increases [3]. The oxidation of the film occurs via temperature-dependent reaction processes, and there are techniques to separate the reaction temperature effects from the intrinsic temperature effects. One option is to subtract the conductance response of the film in the absence of the analyte. Alternatively, the rapid thermal characteristics of microhotplates make it possible to measure the resistance of a film at a constant temperature even during a temperature program. The microhotplate can be repeatedly cooled/heated in a few milliseconds for resistance measurements at an intermediate temperature after allowing time for equilibrium surface concentrations to be established at the programmed temperatures [1]. Therefore, we can learn how to better operate the sensor and analyze sensor data by understanding the fundamental characteristics of surface-mediated reactions.

Reaction Kinetics

A computer model, based on Langmuir-Hinshelwood surface reactions (Equations 1-3) was developed for a general reducing reaction involving analyte “A", with gas concentration (flux), activation energies (E_A), sticking probabilities, and temperature as variables. The model resembles what one might postulate for catalytic CO oxidation on platinum [4]. It includes: (1) irreversible, dissociative adsorption of oxygen, (2) reversible adsorption of the analyte, and (3) reaction between the analyte and oxygen with rapid desorption of the product. We will use this model to describe reactions in a general sense even though it doesn’t explicitly include intermediate reaction steps or dissociative adsorption of the analyte.

$$O_2 \rightarrow 2O_{ads} \qquad \text{Eq. 1}$$

$$A \leftrightarrow A_{ads} \qquad \text{Eq. 2}$$

$$O_{ads} + A_{ads} \rightarrow AO \qquad \text{Eq. 3}$$

Based on the reactions in Eq. 1-3, the material balances describing the surface coverage of O_{ads} and A_{ads} are

$$d\theta_O/dt = P_{O_2} H_{O_2} (1-\theta_O-\theta_A)^2 - k_1 \theta_O \theta_A \qquad \text{Eq. 4}$$

and

$$d\theta_A/dt = P_A H_A (1-\theta_O-\theta_A) - k_1 \theta_O \theta_A - k_2 \theta_A \qquad \text{Eq. 5}$$

where θ_i is the fractional surface coverage of species i, P_i is the partial pressure, H_i is a term that includes the sticking probability of species i and converts partial pressure to monolayers per second. The rate constants, k_1 and k_2 are assumed to follow the Arrhenius form

$$k_i = \nu_i e^{-E_{A,i}/RT} \qquad \text{Eq. 6}$$

where ν_i is usually assumed to be on the order of 10^{13} s^{-1} for first order processes but literature values range between 10^{10} and 10^{20} s^{-1}. Second order pre-exponential factors are usually much smaller. The value used for the surface reaction activation energy, $E_{A,1}$, was 15 kcal/mol and was chosen to make the predictions consistent with temperature and pressure behavior commonly observed in CO sensing which are sensitivity in the ppm range at temperatures ranging from 150-400 °C. The values used for $E_{A,2}$ are consistent with recent measurements of benzoic acid desorption from a tin-oxide microhotplate (23 kcal/mol) [5]. The value of $E_{A,2}$ was varied to simulate the difference in adsorption energy for two different analytes (e.g., propane and hexane) so that we could test the sensitivity of our analysis technique. The steady state fractional oxygen coverage determined from Eqs. 4 and 5 is plotted versus temperature for partial pressures ranging from 5 to 100 ppm and for $E_{A,2}$ = 25 kcal/mol in Fig. 1 and $E_{A,2}$ = 30 kcal/mol in Fig. 2.

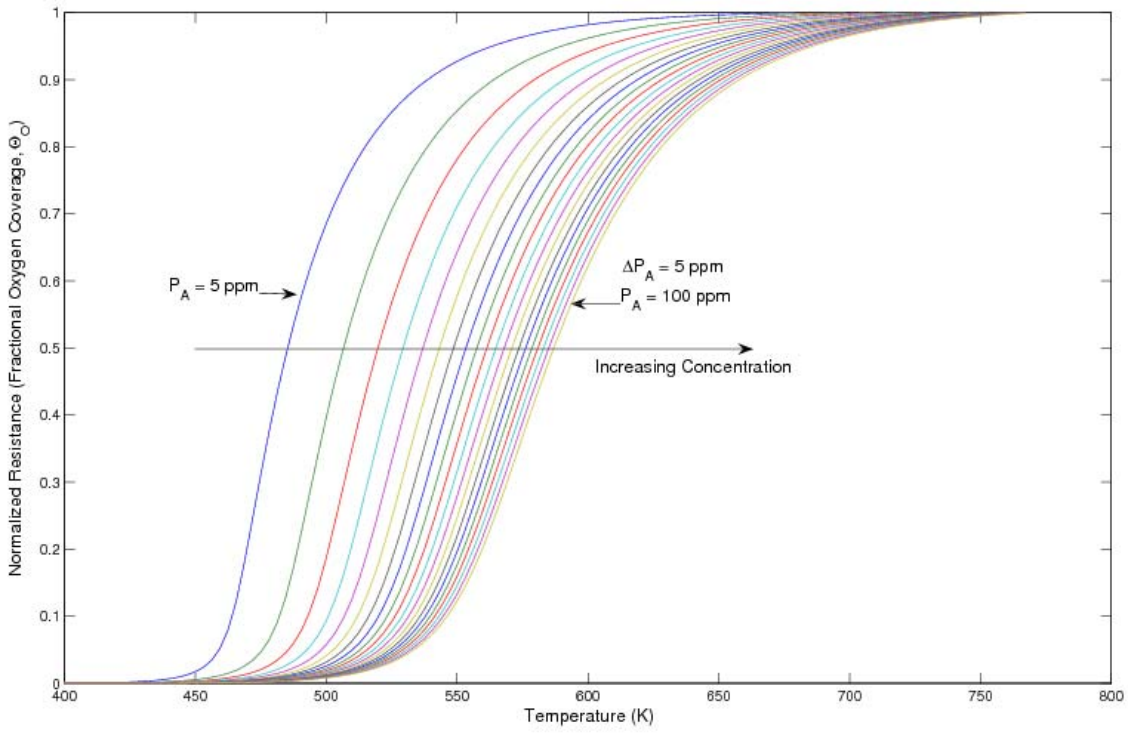

Figure 1: "S" Curves for E_A=25 kcal/mol. 5 to 100 ppm in 5 ppm increments

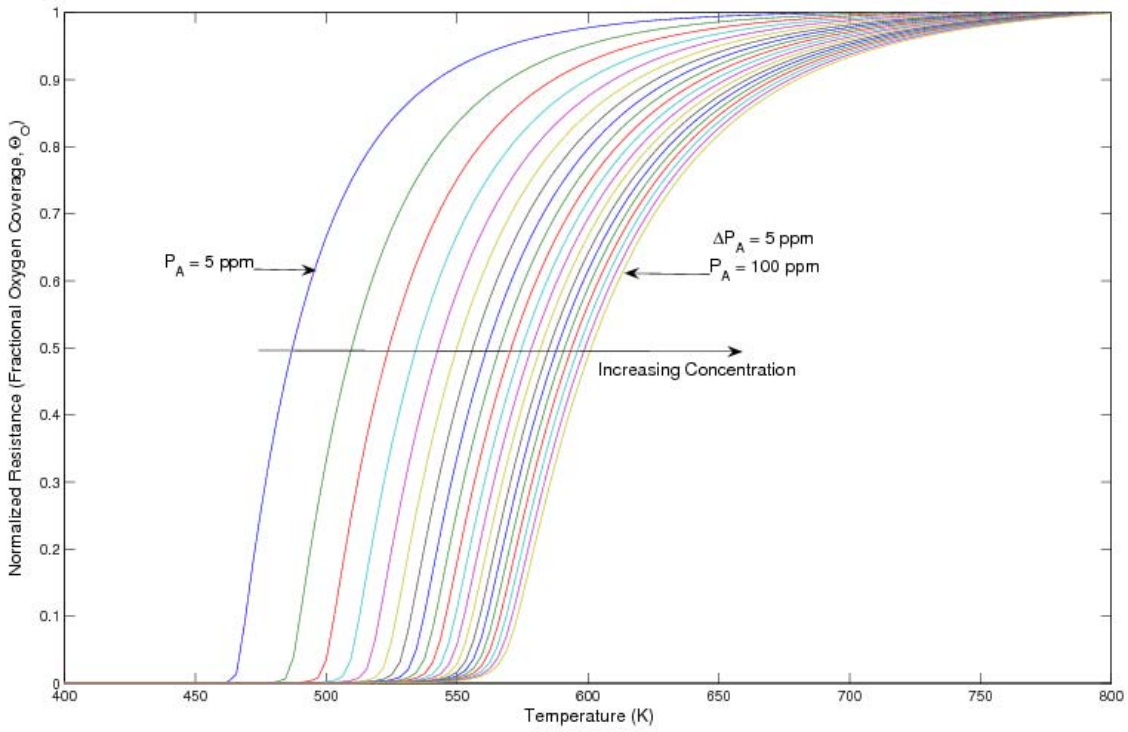

Figure 2: "S" Curves for E_A = 30 kcal/mol. 5 to 100 ppm in 5 ppm increments

Several significant observations were made upon the examination of the curves in Figures 1 and 2. Notably, at low temperature, the oxygen coverage of the film is low, regardless of the type or concentration of target gas present. Conversely, at high temperature, the oxygen coverage is high, independent of the type or concentration of gas present. Hence, even in the presence of gases, it is possible to establish two baselines for a microhotplate film, a lower resistance, (at low temperature) that corresponds to low oxygen coverage, and a high resistance, (at high temperature) corresponding to high oxygen coverage. It is of key importance that these endpoints can be established, even in the presence of target gases of unknown concentrations. A further observation is that the curves in the family are "S" shaped and change from low resistance to high resistance as temperature increases. Although the curves are "S" shaped, the temperature range where the resistance transitions from the low value to the high value is relatively small and is strongly a function of gas species and concentration.

A Novel Approach

The shape and characteristics of the curves make it possible to define an entirely new methodology for quantifying the response of a sensing film. Instead of having a response be the resistance of the film at a given temperature (or the resistances at a set of temperatures), the response is the TEMPERATURE at which the resistance is centered between the upper and lower saturation values. This temperature is strongly a function of gas concentration. Furthermore, the rate of change of the resistance in the vicinity of this temperature is also a function of the activation energy. Hence it is possible with a microhotplate to obtain readings from a film regardless of baseline resistance (or even in baseline resistance changes), to

obtain multiple dimensions of data (in our case two, but this could easily be extended), and to obtain a broader dynamic range than is possible with a fixed temperature system.

Simulated System

A computer on a chip is often referred to as a microcontroller. These devices provide the ability to control and monitor an electrical system using a high level programming language, such as C. Although the processing power remains far below that of a desktop PC, it is sufficient to control the temperature of a microhotplate and monitor the resistance of the metal oxide film. Microcontrollers have the added benefits of being small in size, and of consuming far less power than a traditional PC. This allows for a hand-held, battery powered, mobile sensing instrument. Although microcontrollers have a number of advantages, including small size and low power, their processing power and user interface abilities are limited in comparison to desktop computers. Processing systems that can classify and quantify the gas species present, using artificial neural networks and other soft computing techniques require more processing power than is provided by a typical microcontroller.

We have created a system that combines the benefits of a low power, portable, hand-held, low cost device with the sophistication and computational power of a desktop computer.

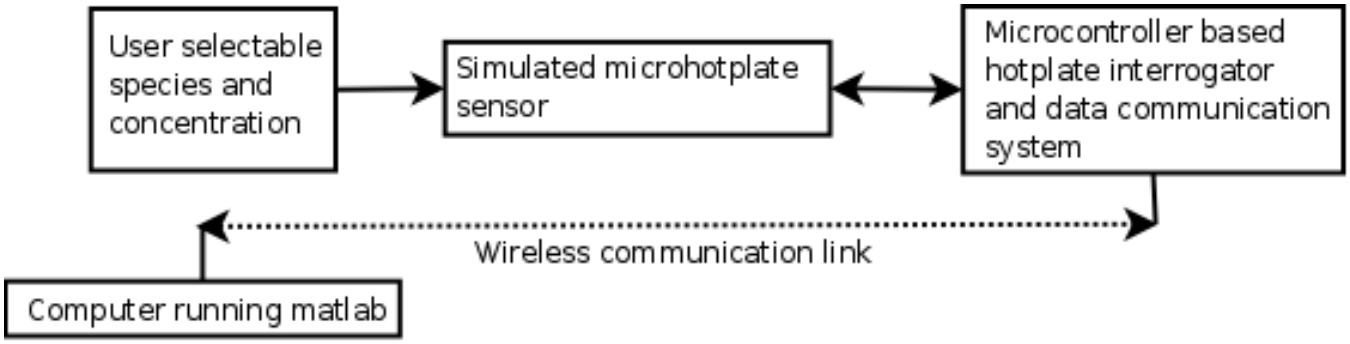

Figure 3: Simulated Sensor Platform

Figure 3, above, shows the simulated system. This system has demonstrated the viability of a "midpoint temperature" method of data analysis. The system consists of three parts. One part simulates the microhotplate itself. Through a set of user selectable inputs, a target gas and concentration is determined. This device acts as a microhotplate with a metal oxide film in the sense that a microhotplate controller commands it to go to a temperature and it responds with a resistance value (with added noise). The controller follows a calibration sequence where it samples the resistance at a low temperature, samples at a high temperature, and from those two resistances, calculates the midpoint resistance value. It then performs a binary search to find the temperature at which this resistance is achieved. Once the resistance is found, the slope of resistance with temperature is estimated by varying the temperature 10°C above and below the midpoint temperature and calculating the change in resistance. The temperature and slope values are communicated wirelessly to a PC using either a Bluetooth serial connection (100m range) or a serial-to-USB converter and processed using nearest neighbor classification functionality from the Neural Network Toolbox in Matlab.

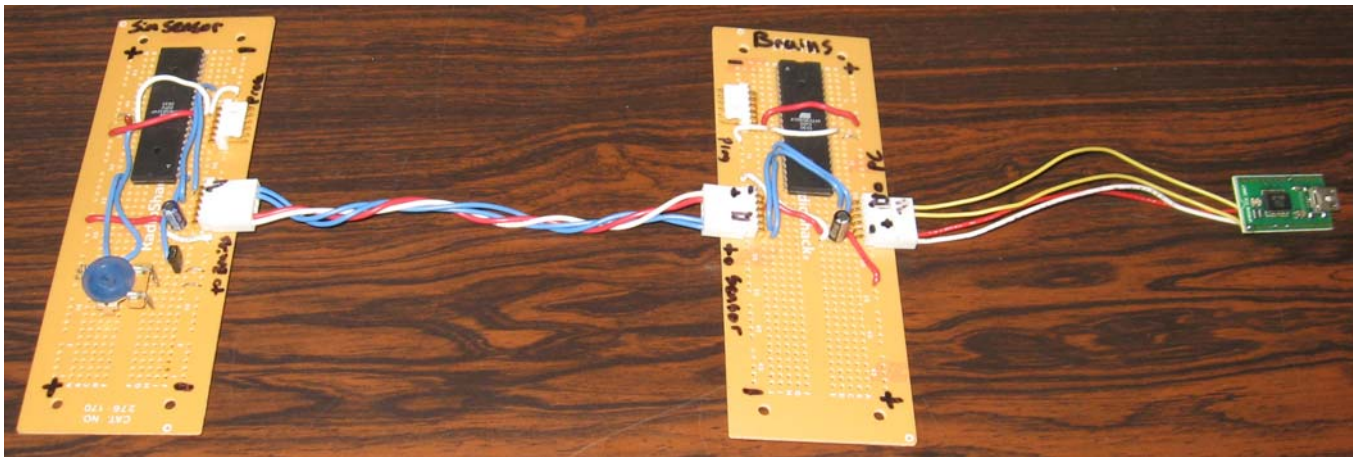

Figure 4: Simulated Sensor, Sensor Controller, and PC Interface

A photograph of the working prototype sensor platform is shown above in Figure 4.

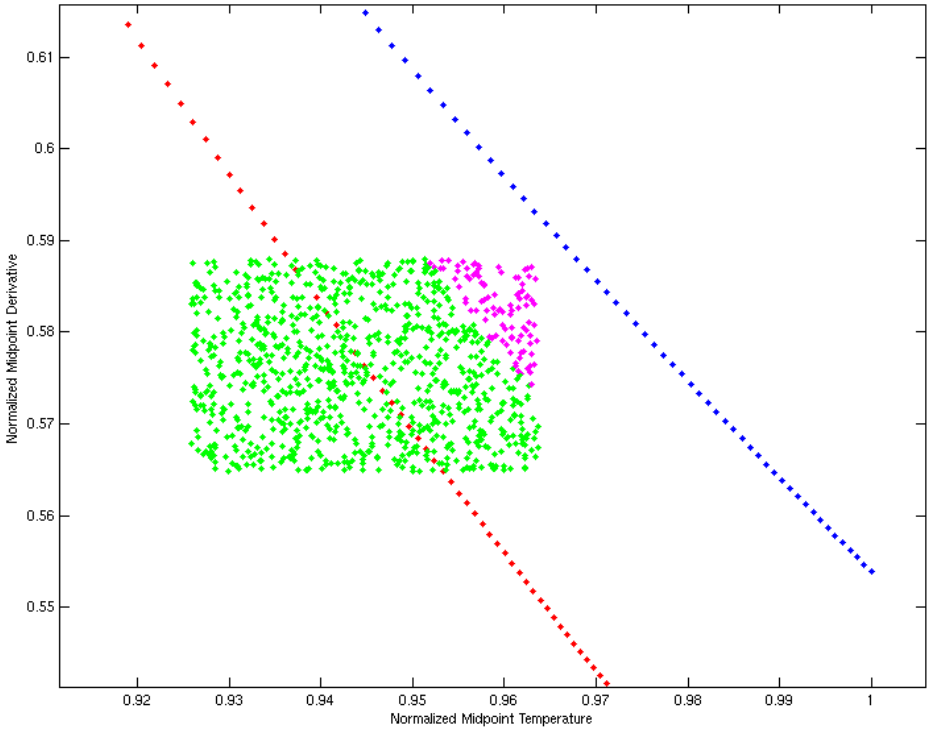

Figure 5: 1000 Samples of Simulated Data, With Added Noise, Showing the Decision Boundary

The PC is used to classify and quantify the sample received from the simulated sensor. Figure 5, above, shows 1000 data points, with random noise added by the sensor. Green points indicate a correct classification, while the pink points indicate an incorrect classification. Having the sensor controller average multiple readings it is possible to reduce the noise.

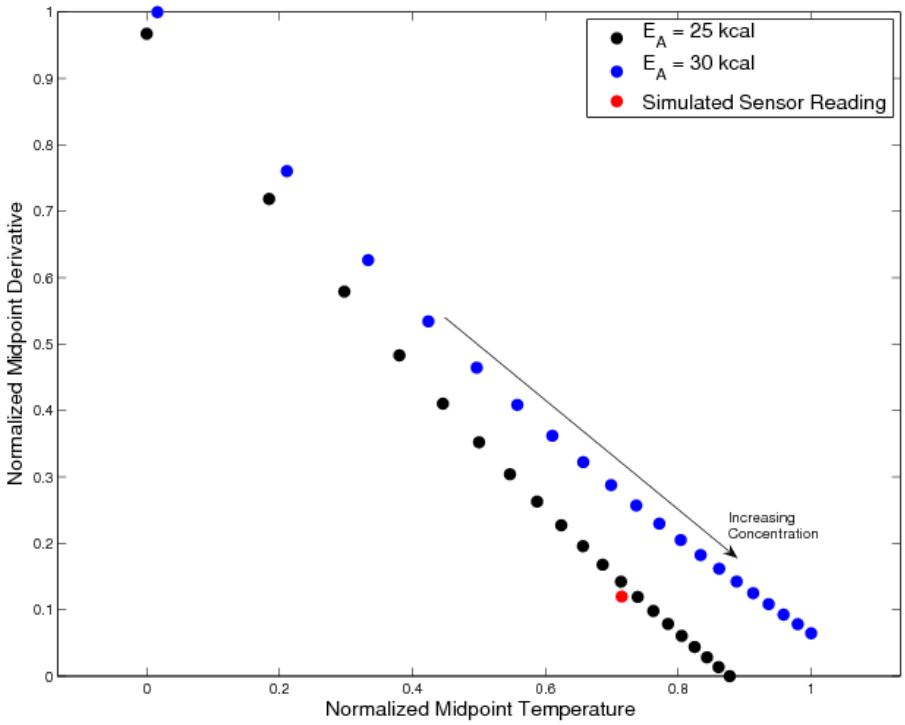

Figure 6: Noisy Data Averaged on the Sensor Controller

Figure 6, above, shows the results of averaging multiple readings together. The PC can now classify and quantify the sensor data using nearest neighbor classification.

Conclusion

Chemical reaction models can give insight into methods for control and analysis of sensor data. In particular, the models indicate that calculating the derivative of the sensor response with respect to temperature might be a reasonable way to increase the dimensionality of TPS data based on reaction kinetics.

A novel approach has been found that works well even in the presence of random noise, allowing the accurate classification and quantification of two similar gases (activation energies differing by approximately 15%) in the range from 5 to 100 ppm. This system represents a novel, demonstrated, method by which microhotplates can be used in a portable, hand-held, battery powered device. Furthermore, the effects of baseline drift, film aging, and noise (often of significant concern in sensor systems) can be addressed in a simple and effective manner. Moving the operating temperature to the region of maximum sensitivity can increase dynamic range of the film. Sophisticated processing techniques, archival storage, networking, user interface, and alarming can be accomplished with the processing power of a desktop PC, without requiring the instrument to be tethered to the PC.

References

1. Cavicchi, R.E., Suehle, J.S., Kreider, K.G., Gaitan, M., and Chaparala, P., "Fast Temperature Programmed Sensing for Micro-Hotplate Gas Sensors," IEEE Electron Device Letters, 16, 286-288 (1995)

2. Meier, D. C., Taylor, C. J., Cavicchi, R. E., White E. V, Ellzy, M. W., Sumpter, K. B., Semancik, S. "Chemical Warfare Agent Detection Using MEMS-Compatible Microsensor Arrays" IEEE Sensors Journal, Vol. 5, NO. 4, August 2005

3. Chwieroth, B., Patton, B. R., Wang, Y. "Conduction and Gas-Surface Reaction Modeling in Metal Oxide Gas Sensors" Journal of Electroceramics 6:1, 27-41, 2001

4. Wheeler, M.C., Cavicchi, R.E., Semancik, S. "Tin oxide microsensors as probes for the oscillatory CO oxidation reaction on supported Pt" J. Phys. Chem. - C III 3328-3332 (2007) and references therein

5. Shirke, A. G., Semancik, S., Cavicchi, R. E., Frederick, B. G., Wheeler, M. C. “Femtomolar Isothermal Desorption using Microhotplate Sensors” *Journal of Vacuum Science Technology A*, 25(3) 514-526 (2007)

Demonstrating a Novel Approach to the Control of Microhotplate Sensors Utilizing a Distributed Computing Approach and Numeric Modeling

Samuel Winchenbach, Department of Electrical and Computer Engineering
Dr. M. Clayton Wheeler, Department of Chemical and Biological Engineering
Dr. Mauricio Pereira da Cunha, Department of Electrical and Computer Engineering and Laboratory for Surface Science and Technology
Dr. Bruce Segee, Department of Electrical and Computer Engineering

THE UNIVERSITY OF MAINE 1865

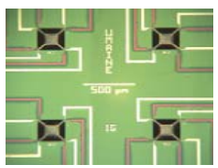
Four Element Microhotplate Array

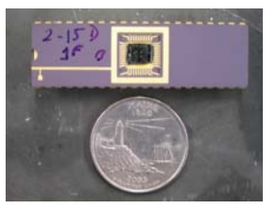
Packaged Microhotplate Array

- Temperature Programmed Sensing (TPS) is a method of gathering data at multiple temperatures from a single device to extract reaction kinetics information.
- The dynamics of chemical reactions change with temperature.
- Microhotplates are platforms that can change temperature rapidly.
- Multidimensional data from TPS can be analyzed with Artificial Neural Networks (ANN).

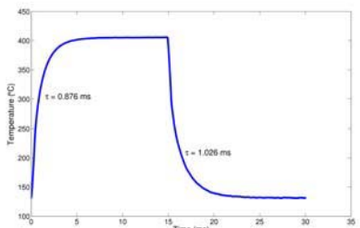

Microhotplate Temperature Response

Reactions

$$O_2 \rightarrow 2O_{ads}$$

$$A \leftrightarrow A_{ads}$$

$$O_{ads} + A_{ads} \rightarrow AO$$

Surface Site Balances

$$d\theta_O/dt = P_{O_2} H_{O_2} (1-\theta_O-\theta_A)^2 - k_1 \theta_O \theta_A$$

$$d\theta_A/dt = P_A H_A (1-\theta_O-\theta_A) - k_1 \theta_O \theta_A - k_2 \theta_A$$

$$k_i = \nu_i e^{-E_{A,i}/RT}$$

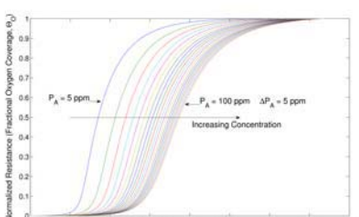

$E_{A,2}$ = 25 kcal

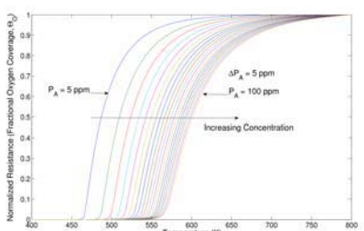

$E_{A,2}$ = 30 kcal

- The model suggests an alternative to TPS.
- Sensor response is assumed to be proportional to steady-state oxygen coverage.
- The S-shaped curves transition from low oxygen coverage in a temperature range determined by gas type and concentration.
- The shape of the transition contains information related the composition and concentration of species present.
- Dynamic Temperature Programing Sensing (DTPS) actively seeks the temperature at which the oxygen coverage is between the minimum (low temperature) and maximum (high temperature).
- The measurement is the temperature at which a response is achieved rather than the response at a fixed (or fixed set of) temperature(s).

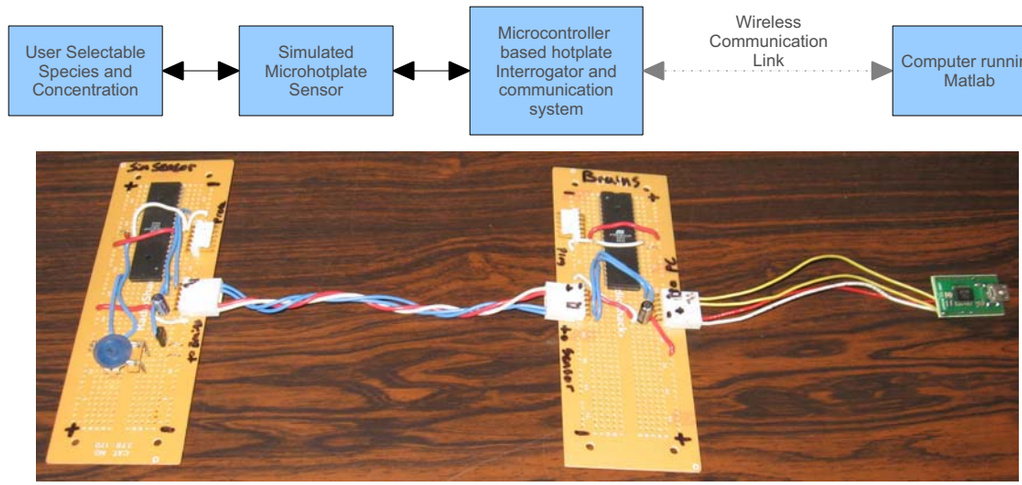

Simulated Microhotplate Sensor Platform with User Selectable Gas Type and Concentration, Sensor Interrogator and USB Communication Board

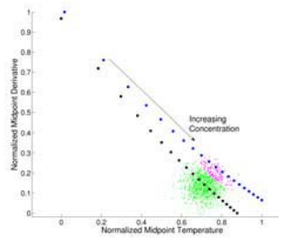

Decision Boundary of Multiple Sensor Readings

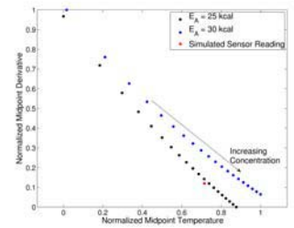

After Averaging Samples Together to Reduce Noise

- The midpoint temperature and derivative of each S-curve is the ideal solution.
- User controls connected to the microcontroller can be used to select both a species and concentration.
- The interrogator probes the simulated sensor in order to obtain a resistance (with random noise added) at a temperature.
- Using DTPS and nearest-neighbor classification an estimate of type and concentration can me made.
- Averaging multiple readings together can be used to reduce noise.

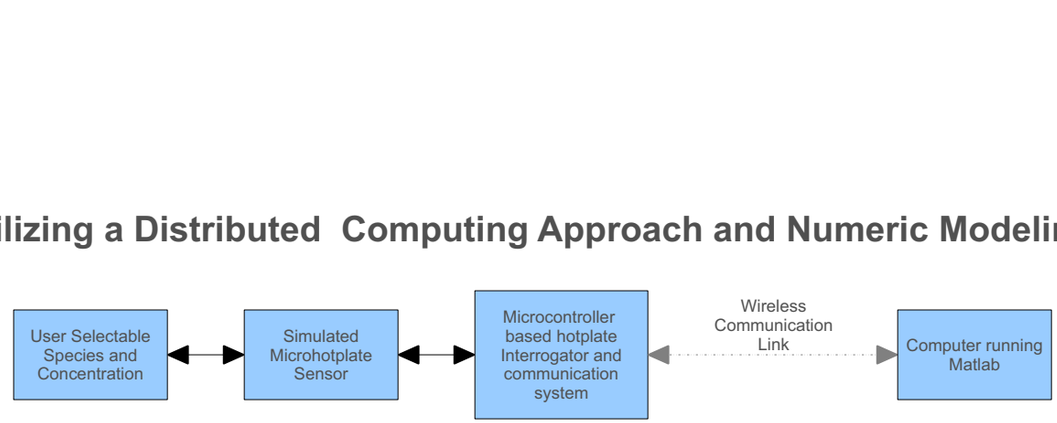

- Reaction kinetics are strongly influenced by temperature
- Microhotplates have the ability to change temperature rapidly
- Traditional sensors look for a response at a given temperature
- We look for a temperature at a given response
- Our method is self calibrating, removing unwanted characteristics such as baseline drift
- Using a low powered microcontroller a prototype based on the model was constructed
- Distributed computing implemented over a wireless link was used to provide the necessary processing power

NSF Grant # CTS-0428341

Submitted for publication to IEEE Sensors Journal. Original manuscript submitted March 05, 2010. Revised manuscript submitted June 03, 2010.

Hydrogen Fluoride Gas Detection Mechanism on Quartz Using SAW Sensors

Bennett J. Meulendyk, *Student Member, IEEE*, M. Clayton Wheeler, and Mauricio Pereira da Cunha, *Member, IEEE*

Abstract— **Hydrogen fluoride (HF) is a hazardous compound used in a variety of industrial processes and is a decomposition product of many environmentally harmful fluorinated volatile organic compounds. Surface acoustic wave (SAW) resonators on quartz substrates are suited for HF sensing because the analyte reacts directly with the sensor substrate, producing H_2O and the volatile compound, SiF_4. This work shows evidence that during gas phase HF exposure to a generalized SAW (GSAW) resonator and a pure shear horizontal SAW (SH-SAW) resonator, the dominant sensing mechanism is the detection of a condensed liquid layer on the substrate surface, rather than simply material removal via SiF_4 desorption. The GSAW and pure SH-SAW resonators, fabricated on ST-X and ST-90° quartz, respectively, have been simultaneously exposed to HF in a low-volume (1.3 cm^3) test cell. An automated gas delivery system developed under this project varied HF concentrations from 1-18 ppm. Both resonators are sensitive to the formation of a condensed liquid layer, but the frequency shift of the pure SH-SAW resonator, due to this effect, is up to 4.6 times greater than that of the GSAW device for the HF concentrations investigated. The measured sensor frequency response to potential inteferents, such as R-134a ($C_2H_2F_4$), isopropanol (C_3H_8O), propane (C_3H_8), acetone (C_3H_6O), and carbon monoxide (CO), is below the device's limit of detection, while its response to HF is as high as 7.5 times its limit of detection.**

***Index Terms*— hydrogen fluoride sensor, generalized and pure shear horizontal SAW, HF sensing on quartz.**

I. Introduction

HYDROGEN fluoride (HF) is used in the production of most fluorine containing compounds, including: refrigerants, herbicides, pharmaceuticals, high-octane gasoline, aluminum, plastics, electrical components, and fluorescent light bulbs, as well as in metal coatings, stainless steel pickling, semiconductor fabrication, and quartz purification. Acute exposure to concentrations of HF exceeding 30 ppm is immediately dangerous to human life, while chronic exposure to concentrations as low as 3 ppm may significantly affect human bones and organs [1], [2], [3]. In addition to HF process monitoring, many environmental contaminants and chemical warfare agents containing fluorine can be selectively detected via HF decomposition products [4] using hybrid sensor systems.

Commercial HF sensor systems that employ electrochemical cells are typically sensitive to concentrations in the range 0.1-20.0 ppm, but suffer poor selectivity since compounds such as HCl, SO_2, HNO, and H_2SO_4 produce sensor responses comparable to that of HF [5], [6], [7]. Other technologies utilized in commercial HF sensors include LED reflectance detectors [8], ion mobility spectrometry (IMS) [9], and tunable diode laser absorption spectroscopy (TDLAS) [10]. While these technologies can selectively identify HF, the LED reflectance detector requires over 10 minutes to detect a potentially deadly leak of 30 ppm [8]; IMS is not capable of reliably quantifying HF concentrations [9]; and TDLAS requires line of sight detection [10].

The need to improve upon commercial devices, namely to enhance the selectivity and sensitivity of HF sensors, reduce the response time and increase the dynamic range, led to further recent research efforts. Heated alkali diodes have demonstrated a sensitivity to HF concentrations as low as 0.01 ppm, although they cannot discriminate between halogenated compounds [11]. Metal-insulator-semiconductor (MIS) devices, while selective, were not able to detect HF concentrations below 6 ppm [12]. Microcantilever MEMS devices with sputter deposited SiO_x layers were shown to be sensitive to the etching of the layer by HF concentrations as low as 0.26 ppm. However, a 7% change in the stoichiometry of the SiO_x layer can result in a 130% change in the deflection of the microcantilever, for the same HF concentration [13]. Porous silicon (PSi) interferometry is another technique, which measures changes in Fabry-Perot interference fringes as HF etches a PSi thin film, was shown to possess a detection limit of 30 ppm and a response time of 10 minutes [14]. Material etching was also reported as the HF sensing mechanism of a surface acoustic wave (SAW) resonator on a quartz substrate, Euler angles [0º, 126º, 90º], with gold electrodes [15]. When measured differentially with respect to a reference device, a frequency shift of 0.13 Hz/s was characteristic of exposure to HF at 1 ppm. The addition of a silica-based sensing layer, deposited atop the resonator, increased the response to 0.83 Hz/s.

This paper reports on two-port platinum electrode SAW

Manuscript received June 03, 2010. This work was supported in part by the U.S. National Science Foundation under grants SST CTS-0428341 and DGE-0504494.

B. J. Meulendyk is with the Electrical and Computer Engineering Department, University of Maine, Orono, ME 04469

M. C. Wheeler is with the Chemical and Biological Engineering Department, University of Maine, Orono, ME 04469

M. Pereira da Cunha is with the Electrical and Computer Engineering Department, University of Maine, Orono, ME 04469 (phone: 207-581-2384; e-mail: mdacunha@eece.maine.edu).

resonator HF sensors, fabricated on both ST-90º Euler angles [0º, 132.75º, 90º] and ST-X Euler angles [0º, 132.75º, 0º]. The measured results show that the device response to HF is caused primarily by the formation of a condensed liquid layer on the substrate surface, rather than material removal. Both the ST-90º and the ST-X sensors exhibit clear frequency response shifts when exposed to HF concentrations in the range of 1 to 18 ppm. In particular, the ST-90º SAW sensor responds to 1 ppm HF with a frequency shift of 0.1 ppm/min (0.5 Hz/s), without the use of a sensing layer or reference device. Additionally, the measured ST-90º SAW sensor frequency variation to potential inteferents such as R-134a ($C_2H_2F_4$), isopropanol (C_3H_8O), propane (C_3H_8), acetone (C_3H_6O), carbon monoxide (CO), was below the device's limit of detection.

The quartz-based HF SAW sensor is expected to have high long-term stability since the detection of HF does not rely on selective or sensitive films, which may degrade or change properties over time. The manufacture of SAW sensors is also highly reproducible, since the technology employs regular semiconductor fabrication techniques. The sensor response to HF may be affected by changes in environmental conditions, such as variations in temperature and humidity. In this work, these variables were controlled and thus their effects on the sensor response were minimized.

Section II of this paper discusses background information regarding the interaction of water with the quartz substrate, the nature of the reaction between HF and quartz, as well as a comparison of the SAW modes propagating on ST-X and ST-90º oriented quartz and their sensitivity to H_2O adsorption and substrate etching. Section III presents the resonator design and fabrication details, in addition to introducing the gas test cell and automated gas delivery system. Section IV contains experimental results and the respective analysis. Section V concludes the paper.

II. Background

A. Interaction of Water with SiO_2

The interaction of water with quartz (SiO_2) substrates is significant because H_2O is both a catalyst for, and a product of, the reaction between HF and SiO_2. At atmospheric pressure and at temperatures below 150 ºC, an SiO_2 surface is fully terminated by hydroxyl groups [16], [17]. This dissociative adsorption of water on SiO_2 surfaces is energetically favorable, as indicated by low surface energy densities, $0.32 < \gamma < 0.43$ J m^{-2}, compared to the pure surface, $1.92 < \gamma < 2.77$ J m^{-2}. Furthermore, hydroxylation of the SiO_2 surface is preferred over molecular adsorption as indicated by the large hydration energies of the former ($-227.1 < \Delta H < -465.4$ kJ mol^{-1}), compared to the later ($-75.8 < \Delta H < -230.2$ kJ mol^{-1}) [16].

Once the SiO_2 surface is fully hydroxylated, molecular water adsorbs to the OH^- groups. The adsorption energy of molecular water, which decreases from -90 kJ mol^{-1} to -50 kJ mol^{-1} as coverage increases from 0 to 0.3 monolayers, is due to two effects: hydrogen bonding and a partial $SiO^{-}\cdots H_3O^+$ ionic interaction. As coverage increases to 0.3 monolayers and above, the $SiO^{-}\cdots H_3O^+$ interaction weakens and the adsorption energy is dominated by the hydrogen bond strength, which is constant at -50 kJ mol^{-1} [18], [19]. Because the adsorption energy is greater than the heat of liquefaction of water (-44 kJ mol^{-1}), the surface is considered hydrophilic [16]. For coverage above 0.3 monlolayers, multilayer condensation occurs in addition to continued growth of the first monolayer via adsorption [18].

Additionally, for coverage less than 0.2 monolayers, the measured sticking coefficient for molecular water on a fully hydroxylated SiO_2 surface is an exponential function of coverage that asymptotically approaches unity at 0.2 monlolayers. For coverage above 0.2 monlolayers, the measured H_2O sticking coefficient is unity for both a fully hydroxylated surface as well as for subsequent monolayers of adsorbed H_2O.

It has also been reported that a fully hydroxylated SiO_2 surface can retain adsorbed molecular water at temperatures up to 200 ºC, due to the increased adsorption energy of H_2O at low coverage. Dehydroxylation begins at 200 ºC and is nearly complete at 1100 ºC [17], [18], [19], [20], [21].

B. HF Vapor Phase Reaction with SiO_2

The reaction of HF with SiO_2 has two significant effects: H_2O generation and substrate material removal [22], [23]. Residual H_2O, scavenged from the hydrophilic SiO_2 surface, acts as a catalyst by ionizing HF, as described by [24],

$$2HF + H_2O \rightarrow H_3O^+ + HF_2^-. \quad (1)$$

The products of Eq. 1 then react with the SiO_2 substrate, as described by [23],

$$SiO_2 + 2H_3O^+ + 2HF_2^- \rightarrow SiF_4 + 4H_2O. \quad (2)$$

The resulting additional H_2O in Eq. 2 enhances the ionization rate of HF, subsequently increasing the reaction rate with SiO_2. This positive feedback mechanism results in the rapid formation of a condensed liquid layer on the SiO_2 surface [23], [24]. Once sufficient H_2O is generated, the reaction progresses as described by [22], [23], [25], [26],

$$SiO_2 + 3H_3O^+ + 3HF_2^- \rightarrow H_2SiF_6 + 5H_2O, \quad (3)$$

producing fluorosilicic acid, much of which remains condensed in the liquid layer. However, some fluorosilicic acid dissociates according to [23],

$$H_2SiF_6 \rightarrow 2HF + SiF_4, \quad (4)$$

where the resulting SiF_4 desorbs from the surface. The liquid layer grows until it becomes sufficiently thick, causing the reaction to become HF_2^- diffusion limited, as the ionized HF must then transport through the liquid layer to react with SiO_2

[22], [23], [24]. The liquid layer attains equilibrium when the rate of desorbing SiF_4 and H_2O balances the rate of HF_2^- transport to the SiO_2 surface [22]. Increasing the concentration of HF gas in the ambient will increase the rate of transport of HF_2^- through the liquid layer, increasing the reaction rate and thus the thickness of the condensed layer until a new equilibrium is reached. Decreasing the HF concentration will cause the liquid layer to decrease, as H_2O evaporates more quickly than can be generated by the reaction. Temperature affects the rate of H_2O evaporation and thus the equilibrium of the condensed layer. It has been shown that the reaction of HF with SiO_2 is maximized when the temperature is within the range 20-35 °C, falling off quickly at temperatures greater than 40 °C [22].

C. GSAW and Pure SH-SAW Modes

The two-port SAW resonators used in this work were fabricated with platinum (Pt) electrodes on ST-X quartz and ST-90° quartz. The ST-X orientation supports a generalized SAW (GSAW), which has particle displacement components in all three directions, parallel and normal to the sagittal plane. The ST-90° orientation supports a pure shear horizontal SAW (SH-SAW), which only has a particle displacement component normal to the sagittal plane.

For sensor applications, an attractive feature of the GSAW along ST-X quartz is its 0 ppm/°C temperature coefficient of frequency (TCF) near 20 °C when aluminum electrodes are used. It was experimentally determined in this work that for Pt electrodes, the zero TCF value is reduced by approximately 50 °C, resulting in a TCF ranging from -4.8 ppm/°C to -6.3 ppm/°C, for temperatures in the range of 20 °C to 35 °C. The TCF for the pure SH-SAW, using Pt electrodes was experimentally determined to range from 33.3 ppm/°C to 31.5 ppm/°C for temperatures in the range of 20 °C to 35 °C. Since the GSAW and the pure SH-SAW device responses are affected by temperature variations, as well as the reaction of HF with SiO_2, an oven, described in Section III, was employed in this work to reduce the effect of temperature on the measurements.

Another attractive feature for high sensitivity SAW sensors is the degree of wave confinement near the surface of the substrate. One measure of this is penetration depth, which is defined as the depth inside the substrate which contains 99% of the wave energy. A lower penetration depth corresponds to a greater confinement of energy near the substrate surface and thus, a more sensitive acoustic mode [27]. The calculated GSAW penetration depth on ST-X quartz is 2.2λ for Pt electrodes with a mark-to-space ratio of 1:1 and H/λ = 0.63%, where H is metal thickness and λ is the SAW wavelength. The calculated pure SH-SAW penetration depth on ST-90° quartz is 0.89λ for the same electrode material and structure. It is interesting to note that the penetration depth for Pt electrodes on ST-X is 2.5 times greater than that for ST-90°, suggesting that the pure SH-SAW should be more sensitive to surface changes than the GSAW on ST-X quartz.

D. SAW Sensitivity to Material Removal and Mass Loading

As described by Eq. 2 and Eq. 3, the reaction of HF with SiO_2 has two effects: liquid generation and substrate material removal. It has been reported in the literature that material removal of less than 100 nm has a negligible effect on the frequency response of GSAW resonators on quartz [0º, 126º, 0º] and pure SH-SAW resonators on quartz [0º, 126º, 90º] [28]. In the current work, etch depths in ST-cut quartz, resulting from SiF_4 desorption, as indicated by Eq. 2 and Eq. 3, were smaller than 10 nm, which was the limit of the profilometer used, and no step could be detected. Due to the reasons listed above, material removal does not significantly affect the frequency response of the resonators in this work.

The sensitivity of a propagating SAW to mass loading, can be investigated using the perturbation analysis developed by Auld [29]. The analysis considers the mechanical surface perturbation on a propagating acoustic wave due to a thin ($h < 0.01\lambda$, where h is the perturbing film thickness), uniform, lossless, isotropic film overlay. When the perturbing layer is liquid phase H_2O, the shear modulus can be considered zero, and mass sensitivity can be expresses as:

$$S_m = \frac{1}{f_0}\cdot\frac{\Delta f}{\Delta m} \approx \frac{1}{V_0}\cdot\frac{\Delta V}{\Delta m} = \frac{V_0}{4}\cdot\left[\frac{{v_x}^2}{P}+\frac{{v_y}^2}{P}+\frac{{v_z}^2}{P}\right], \quad (5)$$

where Δm is the mass change per unit area; $\Delta f = (f\text{-}f_0)$, f_0 and f are the unperturbed and perturbed device frequencies, respectively; $\Delta V = (V\text{-}V_0)$, V_0 and V are the unperturbed and perturbed SAW velocities, respectively; and $|v_i|/P^{1/2}$ is the normalized particle velocity, where i=(x, y, z), v_i are the right-handed Cartesian components of the mechanical particle velocities, and P is the power flow per unit width along the propagation direction. In this work, x is oriented in the direction of propagation, y is oriented normal to the sagittal plane, and z is oriented normal and outward to the substrate surface.

It has been shown by Grate and Klusty that the mass sensitivity of an ST-X quartz resonator, determined experimentally using Langmuir-Blodgett films with h/λ around 0.3%, agrees well (within 4%) with the value from perturbation theory, calculated using Eq. 5 [30]. Table I includes the values for V_0, $|v_i|/P^{1/2}$, and S_m on ST-X quartz, calculated using FEM/BEM [31], considering a Pt λ/8 grating with a mark-to-space ratio of 1:1 and H/λ=0.63 %. The mass sensitivity, for this geometry on ST-X quartz, expressed as a function of frequency, is $S_m = -0.167\cdot10^{-6}$ m^2 kg^{-1} Hz^{-1}.

Rearranging Eq. 5, the normalized frequency shift is given by:

$$\frac{\Delta f}{f_0} = S_m \cdot \Delta m, \quad (6)$$

and Δm can be further expressed by:

$$\Delta m = \frac{1}{S} \cdot \frac{M \cdot \Delta N}{N_A}, \quad (7)$$

where M is the atomic mass of H_2O, ΔN is the number of adsorbed molecules, S is the surface area which they cover, and N_A is Avogadro's constant. Assuming that perturbation theory can be applied to monolayer H_2O adsorption, where h/λ is on the order of 0.001%, and considering that one monolayer of tightly packed H_2O molecules contains $0.48 \cdot 10^{15}$ species/cm^2, the resulting expected frequency sensitivity is -4.6 ppm/monolayer, as depicted in Fig. 1.

III. Experimental Procedure

A. GSAW and Pure SH-SAW Resonator Fabrication and Gas Test Cell

The two-port GSAW and pure SH-SAW resonators used in this work were fabricated in the clean room facilities at the University of Maine's Laboratory for Surface Science and Technology (LASST). Both resonators use interdigital transducers (IDTs) with a periodicity of 16 μm (λ = 16 μm), a nominal mark-to-space ratio of 1:1, and an acoustical aperture of 0.8 mm. The IDTs consist of 40 finger pairs per IDT, and 500 electrodes per short-circuited grating. A zirconium adhesion layer was used with the platinum electrodes; the total bimetal thickness (H) is 100 nm. The GSAW resonator operates at a center frequency of 194.3 MHz, whereas the pure SH-SAW resonator operates at a center frequency of 293.9 MHz. This difference in center frequencies is due to the differing phase velocities of the GSAW ($v_{GSAW} \approx 3108$ m/s) and pure SH-SAW ($v_{SH\text{-}SAW} \approx 4703$ m/s) modes for the same device geometry.

Fig. 2 shows both the GSAW and pure SH-SAW resonators mounted on a printed circuit board (PCB) inside a low-volume (1.3 cm^3) gas test cell. The resonators are bonded to 50 Ω RF feed-throughs, which attach to SMA connectors via microstrip transmission lines on the opposite side of the PCB. Two RF switches connect the resonators to an Agilent 8753D network analyzer (Agilent Technologies, Santa Clara, CA, USA), allowing for the alternating measurement of both devices under identical test conditions.

B. Gas Delivery System

The GSAW and pure SH-SAW resonators were exposed to a variety of environmental test conditions using an automated gas delivery system, depicted in Fig. 3. Mass flow controllers and a bank of actuated valves were used to regulate the delivery of gases at flow rates in the range 40-2000 sccm. In this work, experiments were conducted at flow rates of 100 sccm and 1500 sccm, resulting in residence times in the test cell of 0.77 s and 0.05 s, respectively. Dry air was supplied by a Parker Balston 64-01 membrane air dryer and HPZA-3500 zero air generator (Parker Hannifin, Cleveland, OH, USA). A distilled water vapor liquid equilibrium (VLE) cell produced humid air concentrations up to 6200 ppm. Bottled, anhydrous HF, in a nitrogen carrier gas, was supplied by Matheson Tri-Gas (Matheson Tri-Gas, Inc., Montgomeryville, PA, USA). Other gases, used as potential interferents, were R-134a ($C_2H_2F_4$), isopropanol (C_3H_8O), propane (C_3H_8), acetone (C_3H_6O), and carbon monoxide (CO). Specific gas concentrations, utilized for each experiment in this work, are detailed in the following section.

To reduce the effects of temperature variation on the sensor response, a custom low-temperature oven was constructed. The oven maintains 35.0 ± 0.08 °C, using a resistive air heater operated by a proportional controller with thermistor feedback. A length of coiled tubing and the test cell are placed within the oven to ensure both the resonators and the test gases are at the desired temperature.

To further reduce the effect of temperature on the resonator frequency responses, the experimentally determined TCFs were utilized to correct for minor frequency shifts due to small temperature variations (< ± 0.08 °C) recorded in the test cell during experiments.

IV. Results and Discussion

A. Device Response to Water Vapor

As discussed in Section II, liquid condensation significantly affects the frequency responses of the GSAW and pure SH-SAW resonators. To determine the effect of H_2O condensation, independent of the chemical reaction between HF and SiO_2, the GSAW and pure SH-SAW resonators were simultaneously exposed to 100 sccm of air with humidity levels ranging from 0 to 5775 ppm.

The resonators were initially exposed to 1500 sccm dry air at 35 °C for over six hours to drive off H_2O from the substrate surfaces. Following this, the flow rate was reduced to 100 sccm and the humidity was increased by 825 ppm every 60 minutes, for seven hours. The results of this experiment are depicted in Fig. 4.

With the initial application of 825 ppm humid air, the normalized frequency shift of the pure SH-SAW resonator is 11.9 ppm. For each subsequent 825 ppm increase in humidity thereafter, the normalized frequency shift changes by less than 5.1 ppm. The GSAW resonator is less responsive with an initial normalized frequency shift of 2.8 ppm and shifts of less than 0.75 ppm thereafter. Both resonators reached their steady state frequencies less than 1.5 minutes after each change in humidity.

The concentration of humid air was then reduced to 0 ppm and the GSAW and pure SH-SAW resonators recovered to frequency values 1.5 ppm and 4 ppm less than their initial responses, prior to humid air exposure. This indicates that at the test conditions (100 sccm dry air at 35 °C), residual H_2O remains bound to the SiO_2 substrate surface after humidity is removed from the system.

A semi-infinite water layer on a substrate surface causes the rapid attenuation of a GSAW, due to compressional wave radiation into the liquid. However, throughout this experiment and the following experiments in this work, the reported H_2O monolayers are on the order of $h/\lambda = 0.001\%$, rather than bulk water. The presence of H_2O monolayers resulted in minimal

additional measured losses up to only 0.1 dB, for both the GSAW and pure SH-SAW resonators.

The total normalized frequency shift of the GSAW resonator, when exposed to 5775 ppm humid air, was -5.4 ppm. From Fig. 1, this corresponds to an average H_2O coverage of 1.16 monolayers. Considering this value of H_2O coverage, an experimentally determined mass sensitivity can be calculated for the pure SH-SAW resonator using Eqs. 6 and 7. It is appropriate to note that several of the perturbation theory approximations, such as the uniform, isotropic layer with non-zero shear modulus may not be entirely applicable to the H_2O monolayers. With that consideration in mind, if 1.16 monolayers of H_2O load both the GSAW and pure SH-SAW resonators when exposed to 5775 ppm of humid air, the mass sensitivity that corresponds to a normalized frequency shift of -34 ppm for the pure SH-SAW resonator, is $S_m = -0.695 \cdot 10^{-6}$ m^2 kg^{-1} Hz^{-1}. Thus, the experimentally determined mass sensitivity of the pure SH-SAW resonator is 4.16 times greater than that of the GSAW resonator. The higher experimental SH-SAW sensitivity can be partially credited to its lower penetration depth (0.89λ) when compared to the GSAW (2.2λ).

B. Exposure to Varying Concentrations of HF in Dry Air

The frequency response of the GSAW and pure SH-SAW devices to varying concentrations of HF in dry air is depicted in Fig. 5. After acquiring a baseline measurement of 0 ppm HF at 1500 sccm, the resonators were consecutively exposed to 6, 0, 12, 0, 18, and 0 ppm HF, in 120 minute intervals. The flow rate during HF exposure was reduced to 100 sccm to increase the residence time of HF in the test cell. The flow rate during recovery was increased to 1500 sccm to enhance the desorption rate of the H_2O monolayers from the substrate surface. Two rates of frequency change are observed after each HF gas exposure and are summarized in Table II. The larger, primary rate, results from the rapid growth of the liquid layer during the initiation stage of the reaction. The smaller, secondary rate, occurs when the reaction becomes HF_2^- diffusion limited. Both the initiation rate and the diffusion limited rate increase as the HF concentration is increased.

The standard deviations, σ_0 of the normalized frequency responses of the GSAW and pure SH-SAW resonators in the absence of HF are 0.14 ppm and 0.4 ppm, respectively. Therefore, the limit of detection, defined as $L_D = 3 \cdot \sigma_0$, corresponds to a normalized frequency shift 0.42 ppm for the GSAW and 1.2 ppm for the pure SH-SAW. For an applied HF concentration of 6 ppm, the total normalized frequency shift was $4 \cdot L_D$ for the GSAW and $7.5 \cdot L_D$ for the pure SH-SAW resonators.

Upon removing HF from the test gas and increasing the flow rate of dry air, liquid generation ceased and the liquid monolayers desorbed, resulting in a recovery of the resonator responses. In particular, following exposure to 6 ppm and 12 ppm HF, the GSAW and pure SH-SAW resonator responses shown in Fig. 5 recovered to frequencies that were 0.5 ppm and 2 ppm higher than their baselines, respectively. This result is attributable to incomplete desorption of H_2O on the substrate surface at the start of the experiment and the variability of the desorption rate at high flow rates.

Following exposure to 18 ppm HF, the resonator responses in Fig. 5 did not overshoot the baselines during the 120 minute recovery period. This may be attributable to incomplete desorption of the increased amount of H_2O, created as a result of the increased HF concentration, for the allowed recovery time.

The frequency responses of the GSAW and pure SH-SAW resonators to 1 ppm HF are depicted in Fig. 6 and included in Table II. At this concentration, the GSAW and pure SH-SAW resonators exhibit responses of $2 \cdot L_D$ and $3.3 \cdot L_D$, respectively. These results indicate that the GSAW device is approaching the lower limit of its dynamic range for HF concentrations of 1 ppm, while the pure SH-SAW resonator reveals the capability of measuring concentrations under 1 ppm.

C. Exposure to Varying concentrations of HF in Humid Air

Fig. 7 depicts the results of an experiment conducted to verify the effects of increasing and decreasing concentrations of HF on the condensed liquid layer on the pure SH-SAW resonator. Specifically, the device was initially exposed to stagnant air, followed by 4125 ppm humid air at 100 sccm, causing the frequency to decrease nearly 20 ppm in less than 1 minute, as H_2O quickly condensed on the SiO_2 surface.

At 180 minutes, 18 ppm HF was added to the system. A constant flow rate of 100 sccm was maintained by reducing the humid air concentration to 3310 ppm. The dip observed at 180 minutes is due to the generation of H_2O during the initiation stage of the HF reaction with SiO_2. The magnitude of this reaction is reduced when compared to the dry air carrier gas scenario (Fig. 5), due to the competing effect of H_2O evaporation, resulting from the reduction in humid air. At 182 minutes, the effect of H_2O evaporation dominates the response, causing a 5 ppm positive frequency shift. Meanwhile, HF continues to ionize in the H_2O layer and diffuse to the SiO_2 surface where it reacts. At 195 minutes, when the rate of new H_2O generation exceeds the rate of H_2O evaporation, the condensed layer begins to grow again, causing the resonator frequency to decrease at a rate of 0.069 ppm/min. This secondary rate is nearly three times greater than when dry air was used as the carrier gas (Fig. 5). The reaction of HF with SiO_2 is dependent on the ionization of HF in H_2O, as described by Eq. 1 through Eq. 3. When the carrier gas is dry air, the only source of H_2O is what can be initially scavenged from the SiO_2 surface, supplemented by the H_2O generated as a product of the reaction itself. However, when the carrier gas is humid air, an abundance of H_2O is available at the SiO_2 surface to ionize the HF, resulting in an increased rate of reaction.

At 300 minutes, the HF concentration is reduced to 12 ppm and since the flow rate was maintained at 100 sccm, the concentration of humid air is increased to 3580 ppm. The increase in humid air concentration causes H_2O to quickly condense on the substrate surface, resulting in a 1 ppm step frequency decrease at 300 minutes. The decrease in HF concentration causes the reaction rate with SiO_2 to slow,

resulting in a slight reduction in the slope of the frequency response. At 420 minutes, the HF concentration is reduced to 6 ppm and the humid air is correspondingly increased to 3850 ppm. The reduction in HF, causes the slope of the frequency response to be positive, indicating that more H_2O is now evaporating from the condensed layer than can be supplied by the reaction of HF with SiO_2. At 475 minutes a steady state is reached when the amount of evaporating H_2O equals that being generated by the reaction. At 540 minutes the HF is reduced to 1 ppm and humid air is increased to 4080 ppm. Again, more H_2O evaporates from the liquid layer than can be supplied by the reaction and a steady state is reached at 625 minutes. When HF is removed from the system at 660 minutes, the concentration of humid air is returned to 4125 ppm, and the condensed liquid layer slowly approaches a steady-state thickness, as indicated by the flattening frequency response. The 3 ppm offset in normalized frequency observed at 740 minutes is credited to differences in the total amount of adsorbed H_2O between the beginning (around 150 minutes) and the end of the experiment.

Comparing Figs. 5, 6, and 7, it is interesting to note that independent of the initial amount of adsorbed H_2O on the SiO_2 substrate, the amount of H_2O generated by the reaction with HF is constant when the reaction is at a steady state. In particular, the total normalized frequency shift resulting from exposure to 6 ppm HF in dry air (Fig. 5), measured from the baseline at 30 minutes to the equilibrium value at 60 minutes, is 9 ppm. When 4125 ppm humid air is added to the carrier gas, the total normalized frequency shift resulting from exposure to 6 ppm HF (Fig. 7), measured from the baseline at 180 minutes to the equilibrium value at 475 minutes, is also 9 ppm. Similarly, for 1 ppm HF in carrier gases of both dry and humid air, the normalized frequency shifts are both 4 ppm (Fig. 6, from 30 minutes to 150 minutes; Fig. 7, from 180 minutes to 625 minutes). This indicates that the addition of HF to the system results in the same change in adsorbed H_2O and is independent of the initial amount of H_2O on the surface.

D. Exposure to Potential Interferents

Fig. 8 shows the variation in the frequency response of the pure SH-SAW resonator when exposed to 18 ppm of R-134a ($C_2H_2F_4$), isopropanol (C_3H_8O), propane (C_3H_8), acetone (C_3H_6O), carbon monoxide (CO), and HF, in dry air. The resonator response to the potential interferents was less than its limit of detection while its response to HF was $5 \cdot L_D$, denoting the high selectivity to HF with respect to the measured interferents. Of particular significance, is the lack of response to the hydrofluorocarbon, R-134a, indicating that ionization of the HF molecule is critical in the reaction of HF with SiO_2, and that other hydrogen- and fluorine-containing compounds may not result in a similar sensor response.

V. Conclusions

In this paper the effects of 1-18 ppm HF exposure on both GSAW and pure SH-SAW quartz resonators have been examined. Experiments verified that the formation of a condensed liquid layer on the SiO_2 substrate is the dominant effect in detecting the presence of HF, rather than SiO_2 removal. For the HF concentrations used in this work, the frequency response of the pure SH-SAW resonator was up to 4.6 times greater than the GSAW resonator. The pure SH-SAW device also exhibited the capability of measuring HF concentrations below 1 ppm. Additionally, the resonator response to potential interferents was less than its limit of detection while its response to HF was up to $7.5 \cdot L_D$. These results indicate that quartz-based SAW resonators are well suited for the detection of low concentrations of HF in air.

References

[1] U.S. Agency for Toxic Substances & Disease Registry, "U.S. Toxicological Profile for Fluorides, Hydrogen Fluoride, and Fluorine," 2003.

[2] U.S. Center for Disease Control and Prevention, "NIOSH Pocket Guide to Chemical Hazards," 3rd Ed., 2007.

[3] U.S. Occupational Safety and Health Administration, "Occupational Safety and Health Standards," 2006. [Online] Available: http://www.osha.gov/pls/oshaweb/owadisp.show_document?p_table=STANDARDS&p_id=9993.

[4] H. Sohn, S. Letant, M. J. Sailor, and W. C. Trogler, "Detection of Fluorophosphonate Chemical Warfare Agents by Catalytic Hydrolysis with a Porous Silicon Interferometer," *Journal of the American Chemical Society,* vol. 122, pp. 5399-5400, 2000.

[5] G. A. Milco, "Method and apparatus for the detection of toxic gases," U.S. Patent 5,624,546, 29 Apr 1997.

[6] Enmet Corp., "Personal gas detectors with sample pump for O_3, HF, and other reactive toxic gases," [Online] Available: http://www.enmet.com/index.shtml [Accessed: 24 Nov 2008].

[7] CEA Instruments Inc., "Personal multi-gas confined space entry monitors," [Online] Available: http://www.ceainstr.com/page_1.html [Accessed: 24 Nov 2008].

[8] ATB Analytics LLC, "Shur-Shot Hydrogen Fluoride Detector," 6 March 2008. [Online] Available: http://atbanalytics.com/products.html [Accessed: 24 Nov 2008].

[9] Smith Detection, "Ion mobility spectroscopy," [Online] Available: http://www.smithsdetection.com/eng/IMS.php [Accessed: 24 Nov 2008].

[10] M. B. Frish, M. C. Laderer, R. T. Wainner, A. O. Wright, A. H. Patel, J. Stafford-Evans, J. R. Morency, M. G. Allen, and B. D. Green, "The Next Generation of TDLAS Analyzers," in *SPIE Optics East* Boston, MA, 2007.

[11] J. F. Schabron, S. S. Sorini, and J. F. Rovani, Jr., "Field screening for halogenated volatile organic compounds: the new X-Wand HVOC screening device," Western Research Institute, Laramie, WY, Final Report 06-R009, March 2006.

[12] W. Moritz, S. Krause, A. A. Vasiliev, D. Y. Godovski, and V. V. Malyshev, "Monitoring of HF and F_2 using a field-effect sensor," *Sensors and Actuators B: Chemical,* vol. 24, pp. 194-196, 1995.

[13] J. Mertens, E. Finot, M.-H. Nadal, V. Eyraud, O. Heintz, and E. Bourillot, "Detection of gas trace of hydrofluoric acid using microcantilever," *Sensors and Actuators B: Chemical,* vol. 99, pp. 58-65, 2004.

[14] S. Létant and M. J. Sailor, "Detection of HF Gas with a Porous Silicon Interferometer," *Advanced Materials,* vol. 12, pp. 355-359, 2000.

[15] V. Blondeau-Patissier, S. Ballandras, G. Lengaigne, W. Daniau, G. Martin, P. Blind, D. Hauden, and M. H. Nadal, "High sensitivity anhydride hexafluorhydric acid sensor," *Sensors and Actuators B: Chemical,* vol. 111-112, pp. 219-224, 2005.

[16] N. H. de Leeuw, F. M. Higgins, and S. C. Parker, "Modeling the Surface Structure and Stability of α-Quartz," *The Journal of Physical Chemistry B,* vol. 103, pp. 1270-1277, 1999.

[17] O. Sneh and S. M. George, "Thermal Stability of Hydroxyl Groups on a Well-Defined Silica Surface," *The Journal of Physical Chemistry,* vol. 99, pp. 4639-4647, 1995.

[18] O. Sneh, M. A. Cameron, and S. M. George, "Adsorption and desorption kinetics of H2O on a fully hydroxylated SiO2 surface," *Surface Science,* vol. 364, pp. 61-78, 1996.

[19] V. Bolis, B. Fubini, S. Coluccia, and E. Mostacci, "Surface hydration of crystalline and amorphous silicas," *Journal of Thermal Analysis and Calorimetry,* vol. 30, pp. 1283-1292, 1985.
[20] D. W. Sindorf and G. E. Maciel, "Silicon-29 NMR study of dehydrated/rehydrated silica gel using cross polarization and magic-angle spinning," *Journal of the American Chemical Society,* vol. 105, pp. 1487-1493, 1983.
[21] W. K. Lowen and E. C. Broge, "Effects of Dehydration and Chemisorbed Materials on the Surface Properties of Amorphous Silica," *The Journal of Physical Chemistry,* vol. 65, pp. 16-19, 1961.
[22] P. J. Holmes and J. E. Snell, "A vapour etching technique for the photolithography of silicon dioxide," *Microelectronics and reliability,* vol. 5, pp. 337-341, 1966.
[23] C. R. Helms and B. E. Deal, "Mechanisms of the HF/H_2O vapor phase etching of SiO_2," *Journal of Vacuum Science and Technology A,* vol. 10, pp. 806-811, 1992.
[24] N. Miki, H. Kikuyama, I. Kawanabe, M. Miyashita, and T. Ohmi, "Gas-phase selective etching of native oxide," *Electron Devices, IEEE Transactions on,* vol. 37, pp. 107-115, 1990.
[25] M. Wong, M. M. Moslehi, and D. W. Reed, "Characterization of Wafer Cleaning and Oxide Etching Using Vapor-Phase Hydrogen Fluoride," *Journal of The Electrochemical Society,* vol. 138, pp. 1799-1802, 1991.
[26] J. Allgair, J. M. Ryan, H. J. Song, M. N. Kozicki, T. K. Whidden, and D. K. Ferry, "Nanoscale patterning of silicon dioxide thin films by catalyzed HF vapor etching," *Nanotechnology,* vol. 7, pp. 351-355, 1996.
[27] M. Pereira da Cunha, D. C. Malocha, D. W. Puccio, J. Thiele, and T. B. Pollard, "LGX pure shear horizontal SAW for liquid sensor applications," *Sensors Journal, IEEE,* vol. 3, pp. 554-561, 2003.
[28] S. Ballandras, M. H. Nadal, W. Daniau, V. Blondeau-Patissier, V. Eyraud, D. Hauden, B. Guichardaz, L. Hairault, B. Lebret, and P. Y. Caze, "Toward the development of an anhydride hexafluorhydric acid sensor based on surface transverse wave devices," in *Ultrasonics Symposium, 2002. Proceedings. 2002 IEEE*, 2002, pp. 457-460 vol.1.
[29] B. A. Auld, *Acoustic fields and waves in solids*, 2nd ed. Malabar, Fla.: R.E. Krieger, 1990.
[30] J. W. Grate and M. Klusty, "Surface acoustic wave vapor sensors based on resonator devices," *Analytical Chemistry,* vol. 63, pp. 1719-1727, 1991.
[31] T. B. Pollard and M. P. da Cunha, "Improved pure SH SAW transduction efficiency on LGS using finite thickness gratings," in *Ultrasonics Symposium, 2005 IEEE*, 2005, pp. 1048-1051.
[32] J. Kondoh, K. Saito, S. Shiokawa, and H. Suzuki, "Simultaneous Measurements of Liquid Properties Using Multichannel Shear Horizontal Surface Acoustic Wave Microsensor," *Japanese Journal of Applied Physics,* vol. 35, p. 3093, 1996.

Bennett J. Meulendyk (S'05) was born in Maine in 1982. He received the B.S. degree in electrical engineering at the University of Maine, Orono, ME, USA in 2005 and is currently pursuing his Ph.D. degree in Electrical and Computer Engineering at the University of Maine.

He has been involved with microwave acoustics research and materials characterization in the Microwave Acoustics Laboratory at the University of Maine's Laboratory for Surface Science and Technology (LASST) since the summer of 2004. As an undergraduate student he was a two-time participant in the National Science Foundation Research Experience for Undergraduates (NSF-REU) summer program at the University of Maine. As a graduate student he participated in the National Science Foundation's Integrative Graduate Education and Research Traineeship (IGERT). His current research interest involves the development of SAW chemical sensors.

M. Clayton Wheeler was born in San Diego, CA in 1963, and received a Bachelor's (1991), Master's (1996), and Ph.D. (1997) in Chemical Engineering from the University of Texas at Austin. He is a registered professional chemical engineer with over 30 publications in the areas of surface adsorption dynamics, chemical sensing, and heterogeneous catalysis. He worked on many multidisciplinary teams during his tenure at (i) Texaco where he worked with groups of technicians, physicists, chemists and design, safety, and process engineers in the development of alternative energy sources and (ii) as a National Research Council Postdoctoral Fellow at NIST where he worked with teams of similar composition to fabricate and test sensor devices. His experience in fundamental gas adsorption phenomena at the University of Texas at Austin provides a unique insight into catalytic reaction principles and their application to gas sensing. He joined the Department of Chemical and Biological Engineering at the University of Maine in 2001 where he currently holds the position of Associate Professor. His primary areas of education are in the areas of chemical kinetics, reactor design, and process simulation and design. He is currently leading a research team to develop technologies for converting biomass to liquid fuels and chemicals in which one aspect is use of sensor devices for catalyst discovery.

Mauricio Pereira da Cunha (S'88–M'95–SM'02), born in Brazil in 1963, received the Bachelor's degree, 1985, and the Master's with Honors in electrical engineering, 1989, from the Escola Politécnica, Universidade de São Paulo. Master's thesis title is "Design and Implementation of a 70 MHz SAW Convolver." He received the Ph.D. degree, Dean's Honor List, from McGill University, Montreal, PQ, Canada, in electrical engineering in 1994.Ph.D. thesis title is "SAW Propagation and Device Modeling on Arbitrarily Oriented Substrates".

Mauricio has worked with the Microwave Devices R&D Group at NEC (Nippon Electric Co.), Brazil, Laboratório de Microeletrônica, Escola Politécnica, Department of Electrical Engineering, Universidade de São Paulo, McGill University, Montreal, PQ, Canada, and SAWTEK Inc., Orlando, FL. He passed a sabbatical year at University of Central Florida, Consortium for Applied Acoustoelectronic Technology (CAAT), Orlando, FL, where he worked in cooperation with Piezotechnology Inc, on the characterization of new piezoelectric materials, namely langatate, langanite, and langasite, and with bulk and surface acoustic wave devices. Mauricio was a Professor in the Department of Electronic Engineering, Universidade de São Paulo until he joined the Department of Electrical and Computer Engineering at the University of Maine in 2001, where he presently holds the position of Associate Professor.

Dr. Pereira da Cunha is a member of the IEEE, Sigma Xi, and of the Brazilian Microwave Society (SBMO). He was elected to serve on the SBMO Administrative Committee from 1996 to 1999. He is a reviewer and an associate editor for the IEEE UFFC TRANSACTIONS, and he has been a member of the IEEE International Ultrasonics Symposium Technical Program Committee since 1997. He has served on the UFFC-Society Administrative Committee from 2002–2004, served as Technical Program Committee Chair for the IEEE 2007 Ultrasonics Symposium, New York, NY, and is presently the Vice-Chair for Ultrasonics. He has more than 140 journal, conference, and presentations in the area of microwave acoustic propagation, acoustic wave material properties, bulk and surface acoustic wave modeling and devices, and sensors.

TABLE I. THEORETICAL VALUES CALCULATED VIA FEM/BEM FOR GSAW RESONATORS ON ST-X QUARTZ

v_g (m/s)	$\|v_i\|/P^{1/2} \times \omega^{1/2} \times 10^{-6}$ (m/s)/(W/m)$^{1/2}$			$S_m \times 10^{-6}$ (m^2 kg^{-1} Hz^{-1})
	x	y	*z*	
3080	3.21	0.43	4.90	-0.167
Calculated for a half-metalized, λ/8, Pt grating with H/λ=0.63%.				

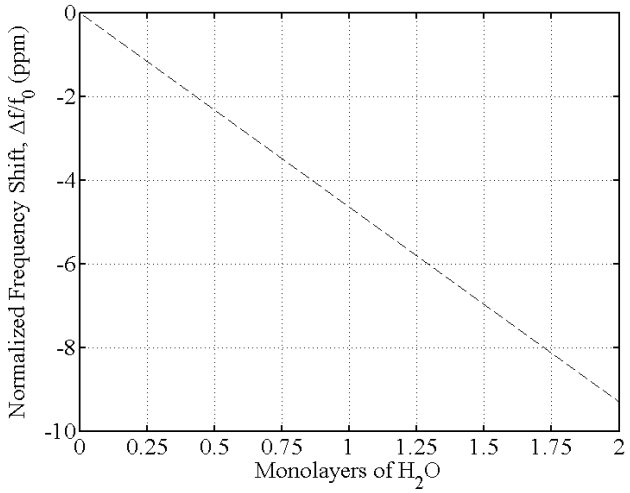

Fig. 1. Theoretical normalized frequency shift of GSAW resonator to monolayers of adsorbed H_2O. GSAW operating frequency: 194.3 MHz.

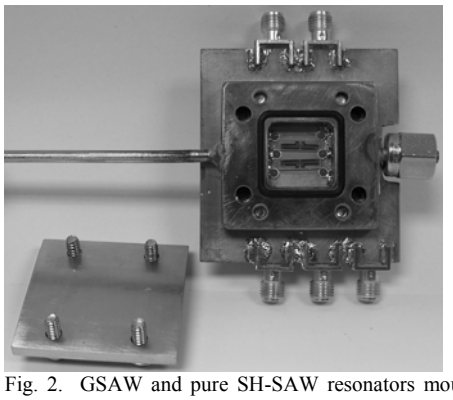

Fig. 2. GSAW and pure SH-SAW resonators mounted inside the gas test cell.

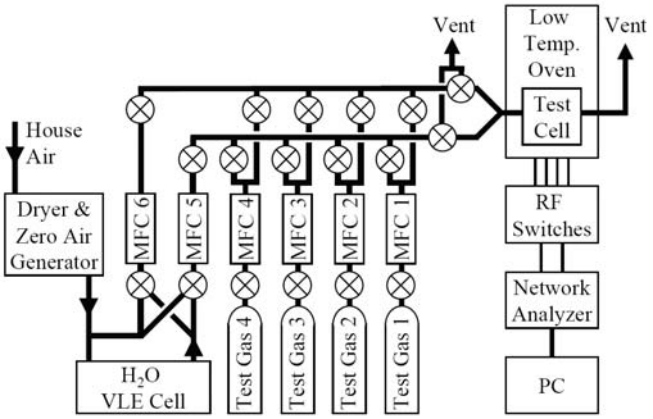

Fig. 3. Representation of the gas delivery system.

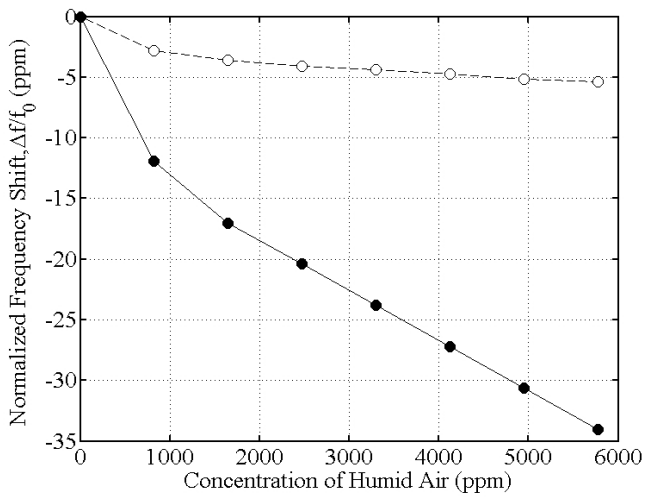

Fig. 4. Normalized frequency shift of the GSAW (dashed line, open circles) and pure SH-SAW (solid line, solid circles) resonators to increasing concentrations of humid air at 100 sccm and 35 °C. GSAW operating frequency: 194.3 MHz. SH-SAW operating frequency: 293.9 MHz.

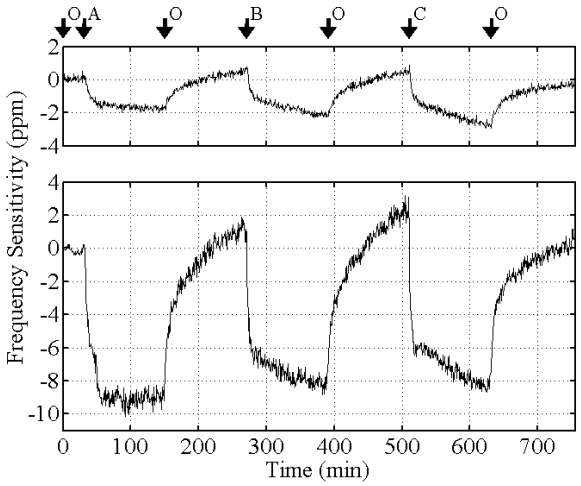

Fig. 5. Normalized frequency shift of the GSAW (top curve) and pure SH-SAW (bottom curve) resonators to HF concentrations of 6 ppm (A), 12 ppm (B), and 18 ppm (C) in 100 sccm dry air at 35°C. At O, the concentration of HF was 0 ppm and the flow rate of dry air was 1500 sccm to enhance the desorption rate of the condensed H_2O monolayers. GSAW operating frequency: 194.3 MHz. Pure SH-SAW operating frequency: 293.9 MHz.

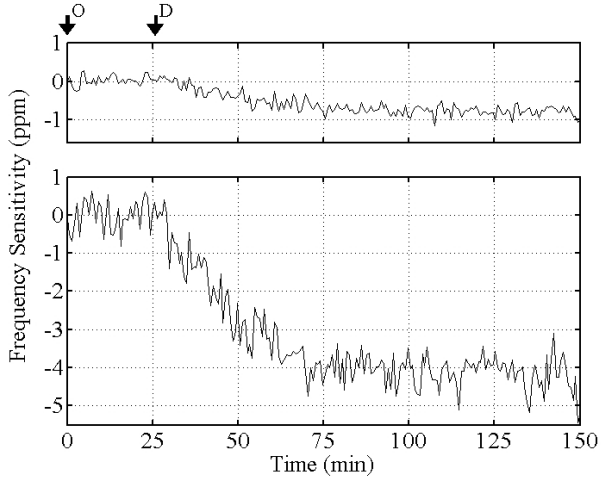

Fig. 6. Normalized frequency shift of the GSAW (top curve) and pure SH-SAW (bottom curve) resonators to an HF concentration of 1 ppm (D) in 100 sccm dry air at 35°C. At O, the concentration of HF was 0 ppm and the flow rate of dry air was 1500 sccm. GSAW operating frequency: 194.3 MHz. Pure SH-SAW operating frequency: 293.9 MHz.

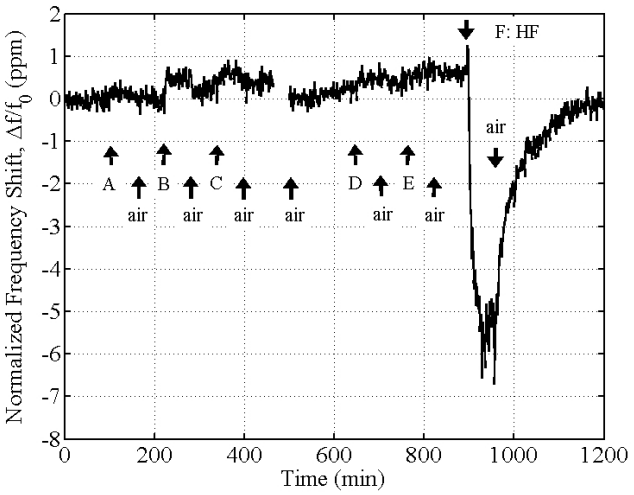

Fig. 8. Normalized frequency shift of SH-SAW resonator to 18 ppm of A: tetrafluoroethane, B: isopropanol, C: propane, D: acetone, E: carbon monoxide, and F: HF, in 100 sccm dry air at 35 °C. The experiment was conducted in two parts because the gas delivery system is restricted to four simultaneous gases. SH-SAW operating frequency: 293.9 MHz.

TABLE II. PURE SH-SAW AND GSAW RESONATOR RESPONSES TO VARYING CONCENTRATIONS OF HF IN 100 SCCM DRY AIR AT 35 °C

HF conc.	**Pure SH-SAW**		**GSAW**	
	Primary rate (ppm/min)	***Secondary rate (ppm/min)***	***Primary rate (ppm/min)***	***Secondary rate (ppm/min)***
1 ppm	-0.091	-0.001	-0.015	-0.002
6 ppm	-0.341	-0.001	-0.108	-0.003
12 ppm	-0.741	-0.018	-0.163	-0.010
18 ppm	-1.326	-0.024	-0.239	-0.013

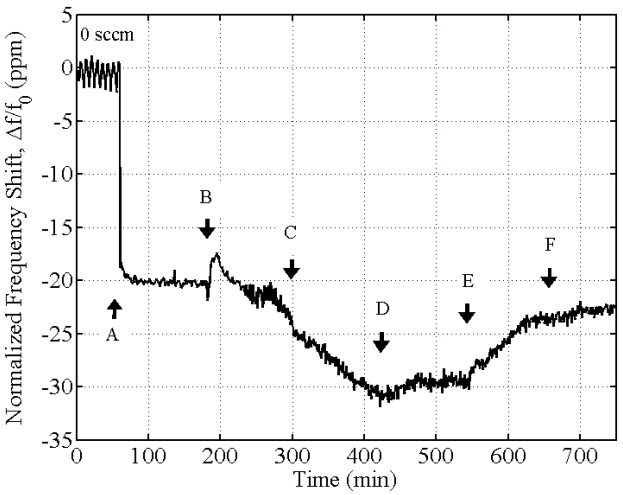

Fig. 7. Normalized frequency shift of the pure SH-SAW resonator to varying concentrations of HF and humid air at 35 °C. A: 0 ppm HF, 4125 ppm humid air, 100 sccm; B: 18 ppm HF, 3310 ppm humid air, 100 sccm; C: 12 ppm HF, 3580 ppm humid air, 100 sccm; D: 6 ppm HF, 3850 ppm humid air, 100 sccm, E: 1 ppm HF, 4080 ppm humid air, 100 sccm; F: 0 ppm HF, 4125 ppm humid air, 100 sccm. Pure SH-SAW operating frequency: 293.9 MHz.

Tracking deformable 2D objects in wireless sensor networks

Guang Jin
Department of Spatial Information Science and Engineering
University of Maine
Orono, Maine, US 04469
jin@spatial.maine.edu

Silvia Nittel
Department of Spatial Information Science and Engineering
University of Maine
Orono, Maine, US 04469
nittel@spatial.maine.edu

ABSTRACT

Geosensor networks are deployed to detect, monitor and track continuous environmental phenomena such as toxic clouds or dense areas of air pollution in an urban environment. In this paper, we abstract such continuous phenomena as 2D objects and only consider their boundary using wireless sensor networks to monitor them over time. In order to maximize energy-efficient monitoring of the phenomena, we present an in-network algorithm based on the concept of deformable curves to incrementally track spatiotemporal changes of the object. We show that the in-network incremental boundary tracking approach based on deformable curves collects sufficient information efficiently to track the overall spatiotemporal properties about a 2D object. By simulations, we demonstrate the energy-efficiency of our approach.

Categories and Subject Descriptors

H.2.8 [**Database Management**]: Database Applications—*Spatial databases and GIS*; H.2.4 [**Database Management**]: Systems—*Distributed databases*

General Terms

Algorithms, Management, Performance

Keywords

Wireless Sensor Networks, Spatial Queries, Deformable Object Tracking

1. INTRODUCTION

Continuous environmental phenomena such as toxic clouds or oil spills in the ocean can be represented by their boundary, i.e. as 2D objects with spatiotemporal properties, since the boundary is often the interesting property with regard to tracking location, spreading or disappearance. Taking the example of wildfires, in October 2007, several wild fires burnt at the same time in Southern California. The Witch Fire, the largest wild fire, started in Witch Creek Canyon near Santa Ysabel and spread quickly to Ramona, Rancho Bernardo, Poway and Escondido. By the end of October, the Witch Fire was fully contained. In this paper, we present an efficient in-network algorithm to track the boundary of an object such as the Witch Fire over time and space by treating its boundary as a deformable curve, and based on the collaboration between neighboring nodes on identifying incremental changes of the deforming curve.

A way to identity the initial 2D boundary is to compare the neighboring sensed values of the sensor nodes in the network, and use user defined thresholds to detect the occurrence of an object such as a fire or toxic cloud [7]. The individual point boundary reports need to be connected as closed curves in *Wireless Sensor Networks* (WSN) [10, 5, 9], and provide snap shots of the 2D objects.

Once the boundary is detected and connected as a closed curve, we are interested in tracking the change of the boundary with minimal number of messages and energy consumption. In our approach we treat the boundary as a deformable curve; thus, the object keeps its identity, but changes its geometry incrementally over time and space. We propose an in-network algorithm, in which sensor nodes have local knowledge about the curve and collaborate with neighboring nodes to monitor the deforming of the curve over time. Our simulation results show that our tracking algorithm requires a small amount of communication cost to maintain the structure of the deformable curve. Different types of aggregated information about the deformable curve can be computed by in-network aggregation algorithms [6] with a minimal amount of communication cost. We also illustrate that the aggregated information can provide qualitative spatiotemporal properties of 2D objects such as shrinking and expanding.

2. PREVIOUS WORK

In this paper, we model space to be observed as a 2D space, $\mathbb{R}^2$. s_i is used to identify a sensor node and also its spatial location. We define the immediate neighboring nodes of sensor node, s_i, as a node set,

$$\mathbb{N}(s_i) : \{s_j | s_j \ AND \ s_i \text{ can directly communicate}\}, \quad (1)$$

and $s_i \in \mathbb{N}(s_i)$.

For the contributions of this paper, we build on previous work with regard to the SNAKE model [2]. We also assume

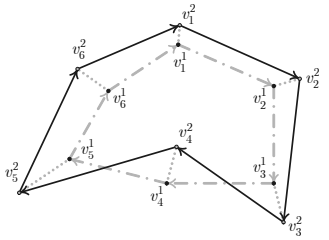

Figure 1: Example of deformable 2D object tracking

that distributed sensor nodes can locally detect points of the object boundary, and can connect them to form the initial closed curve [7, 10, 5, 9]. Figure 1 illustrates an example of how to track a 2D object by using a deformable curve. V^t indicates the curve at time t, and consists of n vertices, $v_1^t, v_2^t, \cdots v_n^t$, linked by straight lines. V^0 indicates the initial boundary. By tracking individual vertices of V^t, sensor nodes are able to track the object's boundary spatiotemporally without knowing the detailed global geometric information about the curve. V^t is defined as follows.

$$v_i^t = (x_i^t, y_i^t), \tag{2a}$$

$$v_{n+1}^t = v_1^t, \tag{2b}$$

$$v_n^t = v_0^t. \tag{2c}$$

The vertices are 2D points as shown by Equation 2a. V^t is a closed curve, as indicated by Equation 2b and Equation 2c.

V^t should well represent the 2D object's boundary at time t. The vertices on a deformable curve change their locations over time to adapt the curve structure to the current boundary's location and shape. According to the SNAKE model the appropriate placement of V^t at time t needs to minimize the quantity, E, as defined by,

$$E = \alpha E_{ten} + \beta E_{cur} + \gamma E_{ext}. \tag{3}$$

E_{ten} in Equation 3 is the first order continuity constraint, which keeps the vertices to be evenly distributed along the boundary. E_{cur} in Equation 3 is the second order continuity constraint, and indicates V^t's curvature. E_{cur} is used to control the curve's smoothness. E_{ext} is known as the external force or edge strength, which keeps the curve close to the 2D object's boundary. α, β and γ are relative weights of each force model, and describe the importance of different forces to the final shape and location of V^t.

3. REVISED SNAKE MODEL

The external and internal forces of the SNAKE model "move" vertices (and consequently the edges connecting them) on a deformable curve to track the 2D object, and capture the boundary changes. To implement our boundary tracking algorithm for WSN, we only allow the vertices, v_i^t, to move onto the locations of sensor nodes. We call a sensor node, s_i, a vertex node at time t, if a vertex v_j^t exists at the location of s_i (i.e. $v_j^t = s_i$). We define the set of neighboring nodes, which can communicate directly with s_i and detect parts of the object boundary, $\mathbb{NB}()$, as,

$$\mathbb{NB}(s_i, t) : \{s_j | s_j \in \mathbb{N}(s_i)\ AND\ \mathbb{B}(s_j, t) = 1\}. \tag{4}$$

The work on external force models is the most active research area with regard to the SNAKE model in the field of image processing. However, many of those models cannot be efficiently implemented in the resource-constrained WSN. Inspired by the balloon model [1], we defined our external force model as,

$$E_{ext}(s_i, t) = \begin{cases} \mathbb{NB}(s_i, t), & \text{if } \mathbb{NB}(s_i, t) \neq \varnothing; \\ \{s_j | s_j \in \mathbb{N}(s_i)\ AND \\ s_j \text{ is inside the curve}\}, & \text{if } \mathbb{NB}(s_i, t) = \varnothing\ AND \\ & s_i \text{ detects object}; \\ \{s_j | s_j \in \mathbb{N}(s_i)\ AND\ s_j \\ \text{is not inside the curve}\}, & \text{if } \mathbb{NB}(s_i, t) = \varnothing\ AND \\ & s_i \text{ detects non-object.} \end{cases} \tag{5}$$

To compute external force model as defined by Equation 5, sensor nodes only exchange messages among immediate neighboring nodes. The proposed external force model creates candidate locations for vertices to move onto. The candidate locations have the same weight with regard to the external force. To calculate the weight among candidate locations, we revise Equation 3 as,

$$E = \alpha E_{ten} + \beta E_{cur}. \tag{3'}$$

Based on Equation 3′, a vertex moves to the location with the minimal weight among the candidate locations provided by our external force model.

We use a light-weight E_{ten} model which only requires exchanging messages locally as suggested by Perrin et al. [8],

$$E_{ten} = Var\left(\left|v_i^{t+1} - v_{i-1}^t\right|, \left|v_i^{t+1} - v_{i+1}^t\right|\right). \tag{6}$$

For a candidate location, v_i^{t+1}, of v_i^t, $Var()$ measures the variance of the lengths of two connected edges, $\left|v_i^{t+1} - v_{i-1}^t\right|$ and $\left|v_i^{t+1} - v_{i+1}^t\right|$. Equation 6 constrains the vertices to be evenly distributed along the curve. To compute E_{ten} defined by Equation 6, a vertex node only needs its immediate neighboring vertices' locations on the deformable curve.

The new curvature force is defined as,

$$E_{cur} = Var\left(\pi, \angle v_{i+1}^t v_i^{t+1} v_{i-1}^t\right). \tag{7}$$

As indicated by Equation 7, our curvature model is biased towards straight lines, through which the smoothness of deformable curves can be maintained. The locations of the immediate neighboring vertices on the deformable curve is sufficient for a vertex node to compute E_{cur} as defined by Equation 7.

The parameter D_{split} controls the number of vertices when the curve deforms.

$$\begin{cases} \left|v_{i+1}^t - v_i^t\right| \leqslant D_{split}, & \text{No change;} \\ \left|v_{i+1}^t - v_i^t\right| > D_{split}, & \text{Add a vertex between} \\ & v_i^t \text{ and } v_{i+1}^t. \end{cases} \tag{8}$$

In order to dynamically add or remove vertices, a vertex node can compare the distance to its immediate neighboring vertices with D_{split}.

Based on the proposed external and internal force models, sensor nodes exchange messages only among neighboring nodes to update the latest forces and adapt the shape and location of deformable curve. For example, to maintain E_{ten} and E_{cur}, a vertex node needs the locations of its immediate two neighboring vertices. By updating the external and internal forces and maintaining the deformable

curve structure, the real-time tracking of 2D objects can be implemented resource-efficiently.

4. EXTRACTING 2D OBJECT'S SPATIAL PROPERTIES

Based on the locations of the vertices on a deformable curve and the vertex movement, we extract aggregated information to represent the overall spatial and spatiotemporal changes of the 2D object. Due to the space limitations, we only list a few types of aggregated information as follows.

$$A^t = \frac{1}{2}\sum_{i=1}^{n}\left(x_i^t y_{i+1}^t - x_{i+1}^t y_i^t\right). \tag{9}$$

As indicated by Equation 9, the area value of a closed curve is represented by an aggregated result. A vertex node prepares its local partial results based on its location and its immediate neighboring vertex on the deformable curve. Similar to computing $SUM()$ in TAG [6], the area about the current curve can be aggregated through the in-network aggregation information processing.

$$C^t = (x_C^t, y_C^t), \tag{10a}$$

$$x_C^t = \frac{1}{6A^t}\sum_{i=1}^{n}\left[(x_i^t + x_{i+1}^t)(x_i^t y_{i+1}^t - x_{i+1}^t y_i^t)\right], \tag{10b}$$

$$y_C^t = \frac{1}{6A^t}\sum_{i=1}^{n}\left[(y_i^t + y_{i+1}^t)(x_i^t y_{i+1}^t - x_{i+1}^t y_i^t)\right]. \tag{10c}$$

The *centroid* of a 2D object is also called the center of mass or the center of gravity. We treat the centroid of a 2D object as a 2D point, as indicated by Equation 10a. Based on the in-network aggregation to compute the area of a 2D object, the location of a centroid can be aggregated similarly in-network, as indicated by Equation 10b and 10c.

$$\overrightarrow{C^t C^{t+1}}. \tag{11}$$

Based on the updates about the centroid's location, users can understand an object's overall location changes in space. Equation 11 describes the trajectory of the 2D object between time t and $t+1$. Based on Equation 11, we can support spatiotemporal queries about the object's movement and moving direction. For example, "how fast is the 2D object moving?" and "is the 2D object moving north?"

$$\angle C^t p C^{t+1}. \tag{12}$$

We can also use the centroid to present the rotation information. The rotation information is defined by the centroid's change relative to a given point, p. Based on Equation 12, we can answer spatiotemporal queries about the object's rotation for the given point p, such as "is the 2D object moving anticlockwise with regard to the point p?"

The aggregated information is usually processed using a tree structure [6]. A sensor node prepares a local partial result and aggregates the result with the partial results from its children nodes. A partial result is kept in a constant message size and sent to the parent node. Compared with reporting boundary points and linked curves, processing the aggregated information can greatly reduce the communication requirements. Based on the aggregated information, the user can be informed in real-time about the overall spatiotemporal properties about 2D objects. In this way, a WSN can provide abstract spatial and spatiotemporal properties of 2D objects without reporting the detailed geometric information about the objects, and save energy.

5. EXPERIMENTAL EVALUATION

Table 1: Parameter settings

Parameter	Value	Parameter	Value
Network Layout	Grid	Network size	169
Node Interval	8	Radio Range	10
Root location	$(2, 2)$	D_{split}	18
α	1	β	1
Feeding Interval	$700s$	Sampling Interval	$350s$

We implemented the distributed deformable curve tracking algorithms in TinyOS [4], and used CLDP [3] as the routing protocol. We run our codes in TOSSIM [4], and set the simulated environment as follows. The network has a grid layout and 169 sensor nodes were distributed evenly in a 100×100 2D space at the interval of 8. The root node was located at $(2, 2)$, and connected to a base station. The wireless radio range was 10, which allowed a sensor node to directly communicate with up to four neighbors within the range. To control the curve tracking quality, D_{split} was set to 18. The weights α and β were equal to 1. Sensor nodes collected sensor readings based on two video clips. Each video clip contained one object. The initial shapes of both objects were a solid circle with $radius = 25$. The initial curves were both an inscribed regular octagon of the circle. Object 1 started with the $center = (35, 35)$, and moved $x{+}4, y{+}4$ in each frame while keeping its area constant. Object 2 started with $center = (50, 50)$, and enlarged $radius{+}4$ in each frame while keeping the center unchanged. A video frame was updated to TOSSIM in every 700 seconds. Sensor nodes were woken up in every 350 seconds to collect updated sensor readings, detect objects and boundaries, and deform the tracking curves. A sensor node took a sensor reading at the corresponding pixel value in the concurrent video frame based on the node's location. Table 1 summarizes the parameter settings in our experiments.

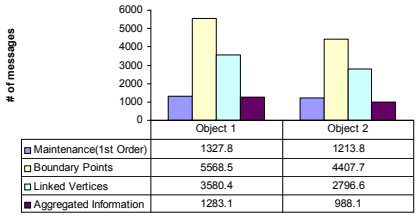

Figure 2: Communication cost

We compared the communication cost of tracking deformable curves against the cost of reporting boundary points. Figure 2 illustrates the average communication costs from the tests. To track both objects, reporting the points around the object boundary is the most expensive among different types of communication cost. Reporting linked vertices required less resources than the point boundary reports did, since some boundary points on a straight line can be suppressed. If we

consider the communication to maintenance the deformable curves, the total communication cost of tracking deformable curves was still a little smaller than the cost of reporting boundary points. Tracking deformable curves enables extracting abstract spatiotemporal properties of objects. We performed tests based on the aggregated information. As shown in Figure 2, processing aggregated information consumed much less communication resources than reporting boundary points or linked vertices required.

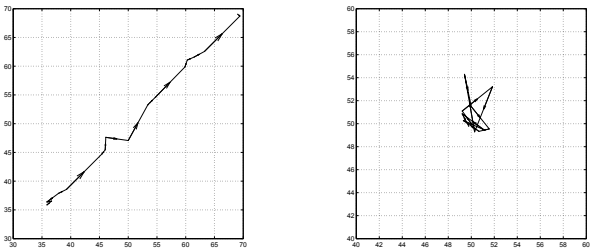

(a) Object 1 (b) Object 2

Figure 3: Centroid moving paths

Due to the space limitations, we only present our experimental results with regard to the area and centroid changes of 2D objects. Figure 3 shows the centroid's movement based on the aggregated information from the tests. In the experimental data set, Object 1 moved from southwest to northeast, while Object 2 kept its centroid at the center of the 100×100 space. Based on the aggregated information, the user can understand the moving patterns of two objects. Object 1 moved, while Object 2 roughly remained still as explained by Figure 3(a) and Figure 3(b). The paths in Figure 3 were not very smooth because of the relatively low monitoring resolution.

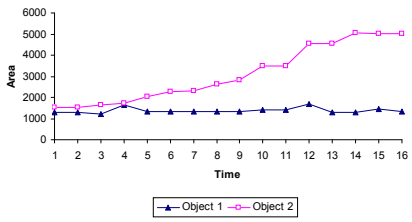

Figure 4: Area change

Figure 4 shows the area changes based on the aggregated information from the tests. A user can see that the area of Object 1 remained constant while the area of Object 2 expanded. Due to the relatively low monitoring resolution, the area changes were not smooth, as shown in Figure 4. By combining Figure 3 and Figure 4, a user can find more complex spatiotemporal properties about the Object 1 and 2.

6. CONCLUSION

We developed a distributed algorithm of tracking 2D objects in WSN based on the SNAKE model. The proposed tracking algorithm maintains the deformable curve by exchanging messages around nearby sensor nodes. Our simulation results show that the communication cost of our tracking algorithm is reduced and scales linearly with the number of vertices on the curve. Based on the in-network tracking of deformable curves, we show that the aggregated information provides qualitative information about spatial and spatiotemporal properties of 2D objects. Our experimental results demonstrate that the wireless communication can be reduced by providing the aggregated information about deformable curves.

Acknowledgements: This research was funded under NSF grants NSF 0448183 and 0428341.

7. REFERENCES

[1] L. D. Cohen. On active contour models and balloons. *CVGIP: Image Understanding*, 53(2):211–218, 1991.

[2] M. Kass, A. Witkin, and D. Terzopoulos. Snakes: Active contour models. *International Journal of Computer Vision*, V1(4):321–331, January 1988.

[3] Y.-J. Kim, R. Govindan, B. Karp, and S. Shenker. Geographic routing made practical. In *NSDI'05: Proceedings of the 2nd conference on Symposium on Networked Systems Design & Implementation*, pages 217–230, Berkeley, CA, USA, 2005. USENIX Association.

[4] P. Levis, N. Lee, M. Welsh, and D. Culler. Tossim: accurate and scalable simulation of entire tinyos applications. In *SenSys '03: Proceedings of the 1st international conference on Embedded networked sensor systems*, pages 126–137, New York, NY, USA, 2003. ACM Press.

[5] Y. Liu and M. Li. Iso-map: Energy-efficient contour mapping in wireless sensor networks. In *ICDCS '07: Proceedings of the 27th International Conference on Distributed Computing Systems*, page 36, Washington, DC, USA, 2007. IEEE Computer Society.

[6] S. Madden, M. J. Franklin, J. M. Hellerstein, and W. Hong. Tag: a tiny aggregation service for ad-hoc sensor networks. *SIGOPS Operating Systems Review*, 36(SI):131–146, 2002.

[7] R. Nowak and U. Mitra. Boundary estimation in sensor networks: Theory and methods. In *IPSN*, pages 80–95, 2003.

[8] D. P. Perrin and C. E. Smith. Rethinking classical internal forces for active contour models. In *IEEE Conference on Computer Vision Pattern Recognition*, volume 2, page 615, Los Alamitos, CA, USA, 2001. IEEE Computer Society.

[9] I. Solis and K. Obraczka. Efficient continuous mapping in sensor networks using isolines. In *The Second Annual International Conference on Mobile and Ubiquitous Systems: Networking and Services (MobiQuitous 2005)*, pages 325– 332, San Diego, CA, USA, July 17-21 2005.

[10] X. Zhu, R. Sarkar, J. Gao, and J. S. B. Mitchell. Light-weight contour tracking in wireless sensor networks. In *The 27th Annual IEEE Conference on Computer Communications (INFOCOM'08)*, 2008.

IEEE TRANSACTIONS ON PARALLEL AND DISTRIBUTED SYSTEMS, vol. 19, (2008), p. 559.,
"10.1109/TPDS.2007.7074

Towards Spatial Window Queries Over Continuous Phenomena in Sensor Networks

Guang Jin and Silvia Nittel
Department Of Spatial Information And Engineering
University of Maine, USA
{jin,nittel}@spatial.maine.edu

Abstract

Recent research on sensor networks has focused on efficient processing of declarative SQL queries over sensor nodes. Users are often interested in querying an underlying continuous phenomenon, such as a toxic plume, while only discrete readings of sensor nodes are available. Therefore, additional information estimation methods are necessary to process the sensor readings to generate the required query results. Most estimation methods are computationally intensive, even when computed in a traditional centralized setting. Furthermore, energy and communication constraints of sensor networks challenge the efficient application of established estimation methods in sensor networks. In this paper, we present an approach using Gaussian Kernel estimation to process spatial window queries over continuous phenomena in sensor networks. The key contribution of our approach is using a small number of Hermite coefficients to approximate the Gaussian Kernel function for sub-clustered sensor nodes. As a result, our algorithm reduces the size of messages transmitted in the network by logarithmic order, thus, saving resources while still providing high quality query results.

***Index Terms*— Wireless sensor networks, spatial databases, distributed databases, query processing.**

I. Introduction

Today, micro-scale sensing in combination with tiny computing and communication devices forming sensor networks enable us to measure physical environmental phenomena in a level of detail that we were not able to observe and measure before.

A. Problem Definition

Sensor networks continuously collect information about the physical environment. Due to their massively parallel, distributed, failure-prone and energy-constrained nature, sensor networks are tedious to program. The database community takes the standpoint that viewing a sensor network as a distributed database system, which accepts and processes declarative SQL queries, significantly simplifies the programming and deployment task of sensor networks. Approaches such as TinyDB [1], [2] and Cougar [3], [4] are the first implementations of such small-scale and distributed DBMSs.

Environmental monitoring is usually interested in spatially continuous phenomena, such as microclimates around redwood trees [5] or within vineyards [6]. Spatial window queries are important for users to understand the underlying phenomena, while only sensor readings at discrete and limited node locations are available. Although many available techniques are able to estimate a continuous phenomenon based on point samples, the current research challenge is finding a resource-efficient adaption of those methods for the resource constrained environment of sensor networks.

B. Our Contribution

In this paper, we present SWOP (***S**patial **W**indow Query **O**ver **P**henomena*), an efficient algorithm to support in-network spatial window query processing based on Gaussian Kernel estimation. In general, SWOP first groups sensor nodes into sub-clusters according to node locations. Next, SWOP transforms Gaussian weighted readings into a Hermite series for each cluster representing the detailed information about local sensor nodes to minimize the communication cost. In this way, a large set of node readings can be represented by only a small number of Hermite coefficient terms, while the communication cost for node IDs and individual sensor readings is reduced. Therefore, the total amount of data transmitted inside the network is reduced by logarithmic order, and the computation cost on individual nodes is kept constant. A centralized computer or a microserver deployed in the network with more powerful resources evaluates the transformed, minimized data set to generate the final spatial window query result. Due to the fast convergence speed of

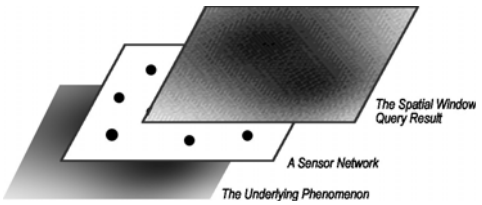

Fig. 1. A model of sensor networks

figure

Hermite expansion, the difference between results of SWOP and the traditional centralized Gaussian Kernel estimation is minimal. The experimental results confirm our expectation and demonstrate the high performance of SWOP for different data sets.

The remainder of this paper is organized as follows: The preliminaries of SWOP are formulated in Section II. Section III reviews several estimation techniques, and Section IV proposes the theoretical foundation of SWOP. We describe the algorithms of SWOP and analyze its computation and communication cost in Section V. The experimental results are illustrated in Section VI. In Section VII, we explore the related work. We conclude and describe the future work in Section VIII.

II. Preliminary

A. Basic Concepts

In this section, we first formalize several relevant concepts for querying continuous phenomena using sensor networks.

Definition 1: A spatial continuous phenomenon is a spatial scalar field that represents the variation of a scalar property over a geographical space. Examples of the scalar properties are temperature, wind-speed, or the concentration of a gas pollutant in the air. Formally, given a geographical space S and a class of scalar values V, a *spatial continuous phenomenon* is a function F whose domain is S and codomain is V [7].

Definition 2: A monitored region, R, is a subarea of the geographical space and is observed by a particular sensor network. Although the physical world is a 3D Euclidean space, in this paper we mainly assume a 2D Euclidean space.

Definition 3: For each point p in R the phenomenon value is represented by $Y(p)$. Additionally, we use s_i to identify an individual sensor node and its spatial location. $Y(s_i)$ is defined as the sensor reading and phenomenon value at the sensor node s_i. For an estimation result for any point p in R, we use $\hat{Y}(p)$.

B. Modeling Sensor Networks And Spatial Window Queries Over Phenomena

A sensor database system is a "mediator" between users and the underlying phenomena, as shown by Figure 1. Most of the current research work focuses on in-network processing of temporal queries. Local processing of temporal queries at individual nodes benefits from the minimized communication messages [8], [9]. Spatial queries, especially over an underlying continuous phenomenon, are not well supported today, since in-network processing of spatial queries is much more complex and expensive than processing temporal queries, and requires the inevitable communication overhead among neighboring nodes.

Spatial queries can be roughly categorized into two groups based on the spatial predicates in the declarative SQL. One type is *point query*, which return values for particular points in space. Here, the query result can be a sensor reading at a well-defined sensor node location, or an estimation result for a point in-between sensor nodes based on neighboring sensor readings. Another type of spatial queries is *spatial region query*, which return values for a continuous spatial region, R. Different from point queries at well-defined node locations, point queries in-between sensor nodes and spatial range queries require additional estimation techniques. For example, Voronoi diagram and TIN (Triangulated Irregular Network) based approaches were used to support spatial aggregation queries [10]. Processing estimation techniques, however, requires additional resources from networks.

An important class of sensor network applications is the observation of spatially continuous phenomena such as microclimates or the distribution of gas pollutants. In this case, simple aggregated statistical information is not sufficient. Here, a special type of spatial region queries becomes relevant, i.e. *spatial window queries* which return the phenomenon's continuous distribution within a well-defined boundary of the monitored region R, e.g."SELECT p.temperatureField FROM Phenomenon p WHERE p.location WITHIN region R". On the contrary to spatial aggregation queries, a spatial window query returns values at arbitrary points in R as shown by Figure 1 and presents the result in a digital format, such as a digital image in a user-defined resolution. The number of points in the result is usually more than the number of sensor nodes within the spatial window predicate. Additional estimation techniques are necessary to "fill" the blank points in-between sensor nodes.

In traditional settings, spatial window queries were processed in a centralized setting based on all raw readings, while constrained sensor networks favor in-network processing of estimation techniques to minimize the data communication cost among nodes.

III. Answering Spatial Window Queries Using Estimation Techniques

Before applying estimation techniques in sensor networks, we need to answer several questions, such as "how to represent a spatial window query result" and "how to process additional estimation techniques in the network".

A. Voronoi Diagram

Voronoi diagrams provide a simple approximation model, where the monitored region, R, is partitioned into a set of "Voronoi cells" based on the locations of sensor nodes. The phenomenon in a cell is presented by the sensor reading at the cell center. For example, a spatial aggregation query result can be represented as a weighted summary of sensor readings according to the sizes of Voronoi cells [10]. To answer a spatial window query, a sensor network needs to find the Voronoi diagram intersected with the query predicate as a set of edges. Suppose n ($n > 3$) sensor nodes involved, the upper bound of the number of edges is $3n-6$, and the lower bound is $n-1$ [11]. A distributed algorithm can find the Voronoi edges, but requires additional resources from the network [10]. Similar neighboring sensor readings can be merged [12], but such compression ideas are also applicable to raw sensor readings. Based on the Voronoi diagram, we can generate a TIN [10] as a 3D terrain about the underlying phenomenon. TINs are useful to generate contour maps about the phenomena, but consume similar resources as Voronoi diagrams do. Overall, using Voronoi diagram based approaches needs an expensive algorithm to find and represent the Voronoi cells, and the estimation results are rather coarse.

B. Spatial Regression

Spatial regression attempts to represent the underlying phenomenon as a function. The solution of regression can be represented as,$\hat{Y}(q) = \sum_{i=1}^{k} [w_i \cdot f_i(q)]$, where the estimated value for any point in R is a weighted summary of predefined basis functions, $f()$s. In a 2D polynomial regression [13], similar to a 1D polynomial temporal regression [8], $f()$s are polynomial functions of x and y coordinates. For instance, an underlying phenomenon can be represented by a quadratic polynomial function, $\hat{Y}(q) = w_0 + w_1 \cdot x_q + w_2 \cdot y_q + w_3 \cdot x_q^2 + w_4 \cdot y_q^2 + w_5 \cdot x_q y_q$, if x_q and y_q represent the x and y coordinates of point q. Another form of spatial regression is known as Kernel regression, where the basis functions are a set of kernel functions, $k()$s [14]. Each kernel function has a unique kernel center in space, and is typically a predefined non-increasing function of the Euclidian distance between the center and the input point. Given k basis functions $f()$s and n sensor readings, to minimize the MSE (Mean Squared Error), the weights for basis functions are computed by, $W = (\sum_{i=1}^{n}(F(s_i)^T F(s_i)))^{-1} \sum_{i=1}^{n}(F(s_i)^T Y(s_i))$, where W and $F()$ are the vector format of w and $f()$, i.e. $W = [w_1, w_2, \cdots, w_k]^T$, and $F(s_i) = [f_1(s_i), f_2(s_i), \cdots, f_k(s_i)]$.

To represent the estimation result, a sensor network only needs to return the estimated weights (W) which require minimal resources from a sensor network compared with transmitting raw sensor readings. One way to find the estimated W is to aggregate the two matrixes, $\sum_{i=1}^{n}(F(s_i)^T F(s_i))$, and $\sum_{i=1}^{n}(F^T Y(s_i))$ within the network, and compute W outside. For a more heterogenous spatial phenomenon, more basis functions are required to increase the estimation quality. However, the cost on networks increases exponentially when applying more basis functions, since each node needs $(k^2+k) * k_i$ data to aggregate for k basis functions if k_i represents the data requirement for one element in the matrix. Choosing special forms of kernels, such as Block kernel or Cone kernel [14], in a kernel regression may relax the data requirement for individual nodes, but the quality of estimation result is deteriorated due to the discontinuity of the kernel functions. Another possible solution is using the distributed matrix inversion operations [14], [15] by exchanging local aggregated matrices among neighboring nodes. This solution is still expensive with regard to the communication cost, since distribution matrix inversion algorithms require more than one iteration of exchanging local information to achieve a satisfactory error tolerance. Although the weights, W, require minimal resources, the communication cost to find the solution of W deteriorates the performance of constrained sensor networks. If a network is monitoring a dynamic phenomenon at a frequent temporal rate, the distributed matrix inversion operations face more difficulties.

For sensor database systems, efficient processing of spatial window queries requires the relaxation of the cost of in-network estimation processing and the in-network representation of the query result. The two requirements are often intertwined. For example, a spatial regression uses minimal resources to represent the weights, W, but requires iterations of communication to find the solution of W. We need to find an estimation model to minimize both requirements and still maintain the high quality of spatial window query results.

IV. Theoretical Foundation of SWOP

A. Kernel Estimation

SWOP is based on another well-known estimation model, Kernel estimation. Different from Kernel regression [14], Kernel estimation is a non-parametric estimation and can be stated as "total amount of observed values per unit area". Kernel estimation is also a special spatial moving-average method, so the estimation result is robust against noise. For a point q in monitoring region R, Kernel estimation estimates the phenomenon value at that point as,

$$\hat{Y}(q) = \frac{1}{\tau^2} \sum_{i=1}^{n} Y(s_i) K\left(\frac{|s_i - q|}{\tau}\right), \text{where } s, q \in R. \quad (1)$$

In Equation 1, $Y(s_i)$ represents a reading for the sensor node s_i, $\hat{Y}(q)$ is the estimation result for the point q, and $|s_i - q|$ presents the Euclidian distance between the point q and the sensor node s_i.

In a simple distributed algorithm [16], [2], [13], every sensor node evaluates its neighboring points in R. In a routing

tree based protocol, each node aggregates its partial result with the partial results from its children [2], [13]. The size of total data extracted from the network is linearly scaled by the number of points to represent the Kernel estimation result. To answer a high resolution spatial query result, we need more estimation points than the number of involved sensor nodes. Therefore, a simple distributed solution often makes no significant improvement compared with a traditional centralized solution, especially when raw readings are compressed in the network.

B. Gaussian Kernel and Fast Transforms

The main difficulty of applying Kernel estimation in sensor networks is the entangled links between estimation points and sensor readings. Neither direct evaluating sensor readings outside the network nor direct evaluating estimation points within the network is resource-efficient.

SWOP chooses another way to efficiently process the Kernel estimation based on the Gaussian kernel. Gaussian kernel is a very smooth kernel function. Gaussian Kernel estimation has a wide range of applications, such as financial analysis [17] and image processing [18], and estimates the phenomenon value at the point q as,

$$\hat{Y}(q) = \frac{1}{\tau^2}\sum_{i=1}^{n} Y(s_i)e^{-|s_i-q|^2/\tau^2}, \text{where } s,q \in R. \qquad (2)$$

To break the entangled links between estimation points and sensor nodes, SWOP has to transform the Gaussian kernel. Two fast transforms are available, the FGT (Fast Gaussian Transform) [19] and the IFGT (Improved Fast Gaussian Transform). Both fast transforms use an infinite series to approximate the Gaussian kernel and truncate insignificant series terms to accelerate the evaluating speed. This feature is very favorable to SWOP, since the truncated series can use a small size of data to represent detailed information about all raw readings. To achieve more efficient processing in constrained sensor networks, SWOP needs to choose an appropriate transform which minimizes the data requirement of communication.

Let's first explain two transforms in the 1D space. The FGT utilizes the Hermite expansion to represent the exponential function as,

$$e^{-|s_i-q|^2/\tau^2} = \sum_{j=0}^{\infty}\frac{1}{j!}\left(\frac{\Delta s_i}{\tau}\right)^j h_j\left(\frac{\Delta q}{\tau}\right), \qquad (3)$$

where $\Delta s_i = s_i - s_*$, $\Delta q = q - s_*$ and the Hermite functions $h_j(x)$ are defined by

$$h_j(x) = (-1)^j \frac{d^j}{dx^j}\left(e^{-x^2}\right).$$

The FGT needs to group sensor nodes into sub-clusters. Here, s_* is the cluster center which satisfies $|s_i - s_*|/\tau < 1$, so the Hermite coefficients converge to zero and the Gaussian kernel can be safely approximated by the first p terms,

$$\hat{Y}(q) \approx \frac{1}{\tau^2}\sum_{j=0}^{p} A_j(s)h_j\left(\frac{\Delta q}{\tau}\right), \qquad (4)$$

where the Hermite coefficients $A_j(s)$ are defined as

$$A_j(s) = \frac{1}{j!}\sum_{i=1}^{n} Y(s_i)\left(\frac{\Delta s_i}{\tau}\right)^j. \qquad (5)$$

The IFGT(Improved Fast Gaussian transform) [18] factorizes the Gaussian kernel as

$$e^{-|s_i-q|^2/\tau^2} = e^{-\frac{\Delta s_i{}^2}{\tau^2}} e^{-\frac{\Delta q^2}{\tau^2}} e^{-\frac{2\Delta s_i \Delta q}{\tau^2}} \qquad (6)$$

and uses Taylor expansion to approximate,

$$e^{-2\Delta s_i \Delta q/\tau^2} = \sum_{j=0}^{\infty}\frac{2^j}{j!}\left(\frac{\Delta s_i}{\tau}\right)^j\left(\frac{\Delta q}{\tau}\right)^j.$$

In IFGT, Equation 2 is approximated as

$$\hat{Y}(q) \approx \frac{1}{\tau^2}\sum_{j=0}^{p} C_j(s)e^{-\Delta q^2/\tau^2}\left(\frac{\Delta q}{\tau}\right)^j, \qquad (7)$$

where the Taylor coefficients $C_j(s)$ are defined as

$$C_j(s) = \frac{2^j}{j!}\sum_{i=1}^{n} Y(s_i)e^{-\Delta s_i{}^2/\tau^2}\left(\frac{\Delta s_i}{\tau}\right)^j. \qquad (8)$$

Here, the cluster center satisfies $2|\Delta s_i||\Delta q|/\tau^2 < 1$, so the Taylor coefficients converge to zero and terms after the first p terms can be safely truncated.

To safely truncate the series, both FGT and IFGT group the sensor nodes into sub-clusters with a radius smaller than the required bandwidth. For each cluster, the Hermite coefficients, Equation 5, and the Taylor coefficients, Equation 8, can represent the detailed sensor locations and readings, therefore are the only data needed from the network. SWOP needs to choose a transform which requires a smaller number of expansion terms for the same quality criteria. If we assume $\rho_s = |s_i - s*|/\tau$ is the normalized cluster radius, and $\rho_p = |q - s_*|/\tau$ is the normalized distance between query points and cluster centers, the Hermite expansion requires $\rho_s < 1$ while the Taylor expansion requires $2\rho_s\rho_q < 1$. The Taylor expansion also requires $\rho_q > 1$, or the estimation result ignores some important readings outside the range [18]. Thus, the Taylor expansion requires smaller cluster radiuses than the Hermite expansion does. The IFGT also introduces an exponential term, 2^j, to the expansion, and therefore decrease the converge speed of the expansion. In other words, even for the same cluster size, the Hermite expansion converges faster to zero than the Taylor expansion does, which can also be proven by the error bound of FGT [20] and IFGT [18]. Thus, SWOP chooses the Hermite expansion to transform raw sensor readings because of the faster convergence speed of Hermite series and the relaxed cluster size.

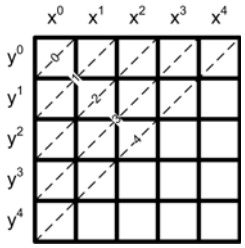

Fig. 2. Coefficient polynomial order

figure

V. SWOP

A. Normalized Kernel

Although Equation 1 is useful in many cases, the normalized Kernel estimation model performs better when nodes are unevenly distributed. The normalized model estimates the phenomenon value at the point q as the estimation value by Equation 1 divided by total kernel weights,

$$\hat{Y}(q) = \frac{\sum_{i=1}^{n} Y(s_i) e^{-|s_i-q|^2/\tau^2}}{\sum_{i=1}^{n} e^{-|s_i-q|^2/\tau^2}}, \text{where } s,q \in R. \quad (9)$$

In Equation 9, τ^{-2} in the denominator and the numerator is cancelled. Based on the normalized model, the estimation result of SWOP is robust against the uneven distribution of sensor nodes, e.g. lossy readings.

B. Data Reduction in High Dimensional Space

Differentiating different dimensions is important when a phenomenon is not isotropic, i.e. the phenomenon is directionally different, so the Kernel estimation can use different bandwidths for different dimensions. In a high dimensional space, the FGT treats Equation 3 as a product of p-terms Hermite expansion along each dimension, and requires p^d terms in total for a d-dimensional space [19]. In the IFGT, the total number of terms in a d-dimensional space is $\binom{p+1}{d}$ by treating the vector product as a scalar dot-product in Equation 6 [19]. Therefore, it is stated that the IFGT outperforms the FGT in high dimensional space [18].

Geoinformation about sensor nodes are at least 2D in real applications. In other words, if we choose to transform the Gaussian function as the normal FGT does, the data requirement grows exponentially for more Hermite coefficient terms along each dimension. The communication channel of constrained sensor networks can be easily overwhelmed to achieve smaller errors for the fast transform. Now, let's reconsider the both transforms as indicated by Equation 4 and Equation 7. Both transforms benefits from the elimination of insignificant series terms with values close enough to 0. According to the inequality for Hermite functions by Szász [21],

$$\frac{1}{n!}|h_n(x)| \leqslant \frac{2^{n/2}}{\sqrt{n!}} e^{-x^2/2}, \text{ where } n \geqslant 0 \text{ and } x \in \mathbb{R},$$

,

$$\frac{2^{n/2}}{\sqrt{n!}} < 1, \text{ where } n \geqslant 4,$$

and $\rho_s < 1$, we can conclude that in Equation 4, the expansion terms converge to zero. The Hermite function, $h_n()$, targets the query point. Only the cluster radius, ρ_s, determine the convergence. Therefore, we can conclude that the significance of the Hermite expansion terms is determined by the polynomial order of the coefficients. In the 1D scenario, taking the first p terms means taking the expansion terms with polynomial order lower than $p-1$ in both fast transforms. In a high dimensional space, the traditional coefficient terms ordering strategy chosen by the FGT requires an exponential increase on the resource consumption to achieve smaller errors. SWOP, on the other hand, reorders the series terms based on their significance, i.e. the polynomial order. For example, in a 2D space, the original Hermite coefficients from the network can be represented as a 2D array as shown by Figure 2, where each element is a sum of products of x and y Hermite coefficients. To get the Hermite coefficients less than the quartic order, SWOP only requires the upper-left triangular matrix, since the lower-right triangular elements are much closer to 0 than the upper-left elements. In this way, SWOP relaxes the data requirement of Hermite expansion from p^d to $\binom{p+1}{d}$ based on $(p-1)$ polynomial order in a d-dimensional space, and requires the same cost as the Taylor expansion does. Our experimental results confirm our expectation that by truncating Hermite series coefficients based on the polynomial order, SWOP outperforms the traditional FGT, since for the same data requirement, SWOP returns better estimation results than the traditional FGT does.

C. Clustering in Dynamic Networks

SWOP groups sensor nodes into sub-clusters according to the node locations and transforms raw readings into the Hermite coefficients. For each sensor cluster, SWOP is a special aggregation query. For different types of networks, SWOP uses different processing strategies.

The main difference for processing SWOP in mobile and static networks is the clustering algorithm. The FGT does it by dividing the space into regular grid cells, named 'Boxes' [19]. This clustering algorithm is very simple, but may introduce many empty boxes due to the uneven distribution of sensor nodes, especially when nodes are mobile. The optimal clustering, however, is known to be *NP* hard [22]. Several sub-optimal clustering algorithms, such as K-means, G-means and hierarchical clustering [23], are still useful for static sensor networks. For a mobile sensor networks, directly distributed applications of such sub-optimal clustering algorithms are not efficient, since the computation and communication cost is

Algorithm 1 Routine of distributed clustering

Require: A required cluster size for appropriate Gaussian kernel bandwidth. The radius of the cluster should be smaller than the bandwidth to satisfy the converge condition of Hermite expansion.
Ensure: This algorithm merges small clusters into larger clusters until no merge can be done.

```
1: new_member = receive_new_join()
2: update_my_cluster(new_member)
3: if to_announce() then
4:     broadcast_announcement()
5: else if candidate = receive_announcement() then
6:     if satisfy_required_cluster_size(my_cluster, candidate) then
7:         join_to(candidate)
8:         resgin_cluster_head()
9:         notify_memeber_nodes()
10:    end if
11: end if
```

too expensive for the constrained environment. Distributed clustering algorithms, such as HEED [24] and LEACH [25], provide solutions for mobile sensor networks. In distributed clustering algorithms, each sensor node can be a cluster head or belong to a cluster. A sensor node with more remaining energy and more potential communication links with others more likely announces itself to be a cluster head. Other nodes can join an appropriate cluster by detecting and analyzing the cluster-head announcements. HEED has several advantages over LEACH, such as supporting multi-hop clustering and different clustering preferences. Thus, we choose the HEED as the basic clustering method in SWOP for mobile networks. In SWOP, the cluster radius should be smaller than the Kernel bandwidth, τ, to satisfy the convergence condition, while bigger clusters are favorable to achieve a higher compression rate. Thus, we set the cluster radius to 0.9τ in SWOP. The only issue of applying distributed clustering algorithms is the required cluster size might be larger than the possible communication range of sensor nodes. In this case, SWOP allows small clusters to merge together till required cluster radius similar to what we did in [26].

After being clustered in SWOP, each sensor cluster is identified by its cluster center, s_*, which may not coincide with the location of the cluster head node. The detailed information about individual sensor readings and sensor locations can be transformed into a small number of Hermite coefficients. Because of the fast convergence speed of Hermite expansion, we expect the difference between the results of SWOP and centralized Kernel estimation is minimal. For each cluster in a mobile network, the Hermite coefficients are a special aggregation data and are routed to the central computer [24]. In a static network, SWOP identifies clusters centrally and dispatches a set of multi-aggregation queries into the network over non-overlapped sub-clusters [27].

D. Description of SWOP Algorithm

Algorithm 1 outlines the clustering algorithm we have developed in [26] for SWOP. When the network starts up, all sensor nodes are cluster heads. Each cluster head uses $to\_announce()$, a HEED like algorithm, to make cluster head announcements. After receiving the cluster head announcements, a cluster head can decide to merge its cluster to another cluster. All non-head member nodes can detect the changes by the notification from their cluster head nodes. Small clusters merge into larger clusters until merging any two neighboring cluster will cause the cluster radius larger than the required cluster size. In a static sensor network, we can apply a centralized, more optimal and more expensive clustering procedure, while the distributed clustering algorithm, such as Algorithm 1 is appropriate for a mobile sensor network.

After identifying the cluster center and the number of nodes in the cluster, distributed sensor nodes can aggregate the Hermite coefficients as indicated by Equation 5. Whether convert the raw readings into Hermite coefficients depends on the number of nodes in every cluster, which will be discussed in Section V-F. Algorithm 2 illustrates the routine of preparing the Hermite coefficients in sensor networks. For a mobile sensor network, Hermite coefficients for both denominator and numerator in Equation 9 should be prepared, if the number of nodes in cluster is large enough. The function $aggregate\_Hermite\_coefficient()$ takes the local sensor's location and reading to prepare Hermite coefficients for required polynomial order according to Equation 5. If a cluster contains a small number of nodes, the raw data including sensor readings and locations are returned to the central computer as shown by Algorithm 2. The numerator coefficients contain both nodes' locations and sensor readings, while the denominator coefficients consist of only nodes' location information. In a static network, we only need the numerator coefficients since the nodes' location information can be cached. We can also utilize a centralized clustering algorithm for static networks to create better clustering pattern and save more energy caused by Algorithm 1. As shown by Algorithm 2, SWOP can be treated as a set of multi-aggregation queries over non-overlapping clusters, which can be efficiently processed by the method provided by [27].

After receiving a spatial window query, a central computer first invokes the necessary sensor nodes and disseminates initial messages into the network as shown by Algorithm 3. After receiving all Hermite coefficients and uncompressed data from all clusters, the central computer needs to reconstruct the weighted readings based on Equation 3 from the partial expansion and sum them with uncompressed readings. After the central computer estimates all points within the spatial window region based on a user-defined resolution, a visual image is returned. SWOP can easily be extended for a stream-based spatial window processing, which just requires a stream feed of the Hermite coefficients from the distributed sensor nodes.

E. Analysis of SWOP

1) Computation Cost: The computation cost of the central computer is related to the number of points m for a user-defined resolution, the number of clusters k and the chosen

Algorithm 2 Routine of preparing Hermite coefficients

Require: The Hermite coefficient polynomial order, n
Ensure: Aggregation of Hermite coefficients from the network
1: $msg = receive\_msg()$
2: **if** $from\_same\_cluster(msg)$ **then**
3: **if** $my\_cluster.number\_of\_members() > tolerance$ **then**
4: $denominator\_coefficients = aggregate\_Hermite\_coefficient(msg, my\_location, 1, n)$
5: $numerator\_coeffcients = aggregate\_Hermite\_coefficient(msg, my\_location, my\_reading, n)$
6: $my\_msg = pack\_message(numerator\_coeffcients, denominator\_coefficients, cluster\_center)$
7: **else**
8: $my\_msg = pack\_message(msg, my\_reading, my\_location, cluster\_center)$
9: $route\_to\_central\_base(my\_msg)$
10: **end if**
11: **else**
12: $route\_to\_central\_base(my\_msg, msg)$
13: **end if**

Algorithm 3 Routine of preparing final spatial window results at the central base

Require: Specifications for required query window, Kernel bandwidth, cluster radius and Hermite coefficient polynomial order.
Ensure: Sending query specifications into the network, and generating the spatial window query results
1: $init\_msg = get\_query(specifications)$
2: $send\_to\_sensors(init\_msg)$
3: $(Hermite\_coefficients, cluster\_centers) = receive\_from\_network()$
4: **for** $point \in query\_window$ **do**
5: $generate\_estimation\_result(point, Hermite\_coefficients, cluster\_centers)$
6: **end for**
7: $return(estimation\_result)$

polynomial order $p-1$. The computation complexity can be formulated as $O(m*k*\binom{p+1}{2})$. The chosen polynomial order $p-1$ and the number of clusters k are much smaller than the number of invoked sensor nodes n for an acceptable error tolerance. The computation cost for a central computer can be relaxed as O(m) which is linearly relative to the user-defined resolution for a spatial window query. Further computation acceleration can be achieved by differentiating the Hermite series around the estimation points as shown by [19]. In this paper, we ignore it because the computation is done by a central computer or a microserver, and the computation cost has no effect on the network.

The computation cost of a sensor node is dominated by the clustering procedure, since aggregating Hermite coefficients requires a constant cost as shown by Equation 5 and Algorithm 2. In a mobile sensor network, SWOP chooses a distributed clustering algorithm which has to consume resources from the network. If SWOP uses a HEED-based clustering algorithm and the required cluster radius is smaller than the communication range, SWOP requires O(1) resources from the network, which has been proven by [24]. If the cluster radius is larger than the communication range and only merge operations among small clusters are allowed [26], in the worst case where all nodes need to be merged into a single cluster, the complexity of the merge operation can be approximated as $O(log(n))$ for n nodes [28]. Thus, the total computation complexity of a sensor node is $O(log(n))$ in the worst case and $O(1)$ in general cases for a mobile network. For a static sensor network, the clustering procedure can be predetermined by the central computer, so the computation complexity can be further relaxed.

2) Communication Cost: The size of the total data extracted from the network of SWOP is determined by the number of clusters, c, and the chosen polynomial order, $p-1$. For each cluster, $k_p+2\binom{p+1}{2}k_i$ bits are needed for the Hermite coefficients, where k_p is the required bit-length to represent a point for the cluster center s_* and k_i is the required bit-length to represent a term of the Hermite series. Whereas, $l(k_p+k_i)$ bits are needed for the raw data if l sensor nodes are in the cluster.

The total communication cost within the network depends on particular communication protocols and the network topology. For a mobile environment, clustering protocols are preferable and typically the non-head nodes and their cluster-heads have a direct communication link. Assuming the worst topology, in which all cluster-head nodes form a line structure, receive and relay messages one by one, SWOP requires $0.5(1+c)c(k_p+2\binom{p+1}{2}k_i)$ data for the total communication between cluster head nodes within the network. If h represents the number of cluster heads before a particular cluster head on the path to the central base, the cluster head receives $(c-h-1)(k_p+2\binom{p+1}{2}k_i)$ and send $(c-h)(k_p+2\binom{p+1}{2}k_i)$ to the next hop. In the best case, in which every cluster head can directly send its messages to the cluster base, the total communication cost within the network is $c(k_p+2\binom{p+1}{2}k_i)$.

For a static environment using routing tree based protocols, SWOP is a set of multi-aggregation queries over non-overlapped spatial clusters. The in-network query processing can be optimized by the algorithm provided by [27], [29], and SWOP is categorized as a *min* query in [27]. Further cost evaluation of communication can be found in [27], [29].

F. Discussion of SWOP

Most processing techniques only focus on the properties of the sensor readings or estimation results. SWOP, however, addresses the spatial properties of the sensor nodes. The compression gain of SWOP results from the spatial clustering. Based on above discussion, we can define the number of nodes in cluster to achieve the compression gain. In a large cluster with more than $[k_p + 2\binom{p+1}{2}k_i]/(k_p + k_i)$ sensor nodes, the raw readings can be reduced to the first $p-1$ order Hermite coefficients in a 2D space. Since SWOP focuses on the spatial properties of the sensor nodes, the available compression techniques can also be applied on SWOP's transformed data among different clusters in the multi-hop transmission. Due to normalized Kernel estimation's robustness against noisy and lossy samples, SWOP performs well in the noisy and lossy environment of sensor networks. Furthermore, we do not limit SWOP to static sensor networks. The denominator in Equation 9 only presents the spatial properties of invoked sensor nodes. In a static sensor network, the spatial properties of sensor nodes are typically cached by the central computer, so more than half of the communication can be saved by excluding the denominator in normalized Kernel estimation from the in-network communication. A centralized clustering can also find better clustering patterns and therefore help SWOP to accomplish even a higher data compression rate.

By significantly compressing the 2D or 3D spatial readings in SWOP, we can treat the transformed data as a special snapshot in 1D temporal space. Therefore, any 1D temporal processing method, such as [8], [9], is applicable to the transformed SWOP data. The temporal processing of SWOP is another important issue; we do not discuss it in this paper due to the space limitation.

Overall, the computation complexity of SWOP with regard to distributed sensor nodes is constant and communication messages are minimized. SWOP is practical for both static and mobile sensor networks.

VI. Experimental Evaluation

SWOP is a set of multi-aggregation queries over non-overlapped spatial clusters in routing-tree based sensor networks. We assume SWOP to be running in a more challenging environment, mobile sensor networks; here, we use a x-y coordinate ($128bits$) to identify sensor nodes, choose the HEED-based clustering procedure, and assume the node communication range is bigger than the required cluster radius (i.e. a direct communication link between a non-head member and its cluster head). We implemented SWOP in Java and ran it over different data sets. In our simulations, the behavior of sensor networks is simulated by treating each sensor node as a thread running independently and communicating with each other by exchanging messages. The data sets consist of two real data sets from the CalCOFI survey off the coast of Southern California [30] and from a snapshot from an experiment in the Intel Lab [31], and two synthetic data sets. Without losing any generalization, we normalized the sensor readings to $[0,1]$. Finding an optimal bandwidth has been researched well for Kernel estimation [32], and the fast optimization algorithm [33] for Gaussian kernel bandwidth is also available. Therefore, we only tested SWOP under pre-chosen bandwidths. The fixed bandwidth is useful to test two synthetic data sets, since we compare the SWOP estimation results with alternative estimation techniques by their processing costs based on the estimation quality. Since related work [14], [13], [10] only compare their approaches with respect to centralized solutions, it is difficult to cross-evaluate them. In our experiments, we compare SWOP with alternative approaches based on "real" underlying phenomena, i.e. two synthetic data sets.

A. Coefficient ordering strategy and error evaluation

Spatial window queries access the distribution of underlying phenomena for a given region. An efficient in-network query processing targets to minimize the difference between results of the traditional centralized techniques and itself. The following tests are based on the average MSE from multiple runs. We first compared MSEs between the results of SWOP and centralized Kernel estimation as shown by Table I based on different truncating strategies. Table I confirms that by ordering the polynomial order of Hermite coefficients, SWOP achieves high quality results while relaxing the data requirement compared with taking the p^2 product by FGT. Aggregating more Hermite coefficients with higher polynomial-order decreases the difference between results of SWOP and the centralized Kernel estimation. Since the maximal MSE between results of SWOP and the centralized Kernel estimation results based on zero-order Hermite coefficients are around 10^{-3}, we performed other quality experiments based on the zero-order Hermite coefficients.

TABLE II. Mean squared errors relative to "real" values

table

Data set	Kernel	SWOP
Synthetic #1	4.6E-03	7.16E-03
Synthetic #2	3.23E-02	4.40E-02

While the first two real data sets only provide us point samples of a realistic underlying phenomenon, the two synthetic data allow us to compare the estimated results with "real" values as shown by Table II. Based on our choice for the first synthetic data set, the mean squared errors between the SWOP result and the "real" phenomenon are around 10^{-3}. The SWOP result of #1 set is reliable for many practical purposes. We fixed the bandwidth for the second synthetic data to test SWOP against alternative approaches, although the MSE on the second synthetic data indicates an over-smoothed result. In practice, the method introduced by [33] can help

TABLE I. Cost and quality based on different truncating strategies

table

p	1	2	3	4	5	6	7	8	9	10
Number Of Total Terms In 2D Space based on different truncating strategies										
p-1 order	1	3	6	10	15	21	28	36	45	55
p terms	1	4	9	16	25	36	49	64	81	100
MSE on the salinity data based on different truncating strategies										
p-1 order	6.93E-04	5.20E-04	7.06E-05	2.01E-05	3.98E-06	8.67E-07	1.66E-07	2.78E-08	5.22E-09	7.18E-10
p terms	6.93E-04	4.53E-04	2.48E-05	1.06E-05	7.88E-07	2.54E-07	1.86E-08	4.18E-09	2.83E-10	4.55E-11
MSE on the Intel Lab data based on different truncating strategies										
p-1 order	1.03E-03	3.19E-04	1.01E-04	1.39E-05	4.76E-06	5.30E-07	1.27E-07	1.55E-08	2.18E-09	3.01E-10
p terms	1.03E-04	3.19E-04	4.55E-05	5.46E-06	1.18E-06	1.21E-07	1.62E-08	1.79E-09	1.33E-10	1.76E-11
MSE on the synthetic data #1 based on different truncating strategies										
p-1 order	7.51E-04	5.24E-04	5.39E-05	9.08E-06	2.19E-06	3.42E-07	5.27E-08	6.47E-09	8.35E-10	7.54E-11
p terms	7.51E-04	4.96E-04	1.01E-04	1.67E-05	5.96E-06	8.55E-07	2.33E-07	2.74E-08	6.36E-09	6.17E-10
MSE on the synthetic data #2 based on different truncating strategies										
p-1 order	2.58E-03	3.64E-04	3.03E-04	2.42E-05	1.29E-05	1.13E-06	4.12E-07	3.70E-08	1.04E-08	8.76E-10
p terms	2.58E-03	3.98E-04	1.78E-04	1.27E-05	4.72E-06	3.47E-07	8.44E-08	6.19E-09	1.23E-09	7.32E-11

users to find the optimal bandwidth according to different phenomenon distributions.

B. Estimation Results

To demonstrate the estimation result using SWOP, we run SWOP multiple times for every data set, and the estimation results with the highest compression rates were chosen for display.

The first data set has 372 measurements of salinity density off the coast of Southern California in the CalCOFI survey [30], based on which a 30×30 estimation map with $\tau = 0.2$ is generated. Figure 3(b) shows the estimation result based on the traditional centralized Kernel estimation while the result using SWOP with 0 order coefficients and the result based on the Voronoi diagram are shown in Figure 3(c) and Figure 3(a) respectively. In this example, the x-coordinate is the distance from the coast, y indicates the depth of the sample, and a lighter point in Figure 3 indicates the saltier water.

The second set of estimation results based on a smaller data set from the Intel Lab is illustrated by Figure 4. In this data set, 48 point samples of the temperature were taken from a snapshot during an experiment in the Intel Lab [31]. A 30×30 map is estimated. The results based on the Voronoi diagram, the centralized Kernel estimation with $\tau = 11$ and SWOP with 0 order coefficients are shown by Figure 4(a), Figure 4(b) and Figure 4(c) respectively, where a darker point indicates the colder temperature.

Both real data sets only provide point samples, but the validation compared to the real underlying phenomena is not possible. Therefore, we use two synthetic data sets to test the effectiveness of SWOP. Two 401×401 continuous gray scale picture were synthetically generated as shown in Figure 5(a) and Figure 6(a). These two data sets can be interpreted as two different distributions of a "real phenomenon". For example, we can assume two gas leakages in the upper-left and lower-right corner of Figure 5(a). We set $\tau = 80$ to test the performance of SWOP based on 21×21 point samples taken from the underlying "phenomenon" at the interval of 20 pixels. Figure 5(b) and Figure 6(b) illustrate the results of centralized Kernel estimation. Figure 5(c) and Figure 6(c) show the SWOP estimation results with 0 order coefficients for the two synthetic data sets. For the fixed bandwidth, both centralized Kernel estimation and SWOP return a truthful estimation result on the synthetic data #1. For the second data set, the two small "gas leakages" are obscured, which indicates an over-smoothed result, and the result of SWOP based on the zero order Hermite coefficients is somewhat distorted compared with the centralized Kernel estimation result. Here, we just set the bandwidth fixed on purpose to compare the SWOP estimation results with other alternative estimation results based on their estimation qualities.

The estimation results based on Voronoi diagram show the layout and readings of sensor nodes directly, but the results are coarse compared with the results based on Kernel estimation. Furthermore, the cost of Voronoi diagram based approaches limits their application in constrained sensor networks. Whereas, even compared with the "real" phenomena, the results of SWOP still directly illustrate the real phenomenon distributions.

C. Cost Evaluation

TABLE III. Required data size for each cluster(in bit)

table

Data set	# of clusters	Raw data	SWOP
Salinity	21	3475.39	253.85
Intel-lab	8.8	1093.12	249.7
Synthetic #1	23.1	3572.66	251.4
Synthetic #2	22.7	3730.04	252.3

In our tests, we use one double ($64bits$) to present a sensor reading and two doubles ($128bits$) to present a sensor node identity, i.e. its location. We recorded the average number of clusters and the average size of raw data and SWOP data for each cluster based on zero order Hermite coefficients from

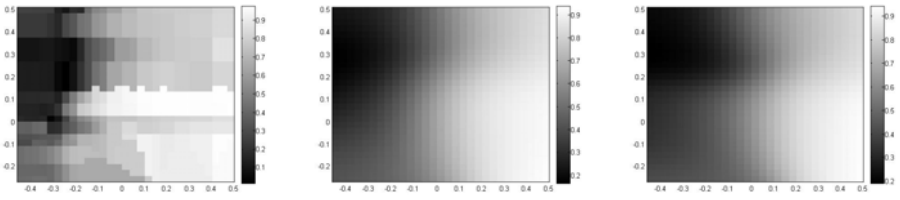

(a) Voronoi diagram (b) Centralized Kernel (c) SWOP

Fig. 3. Query results on the salinity data

figure

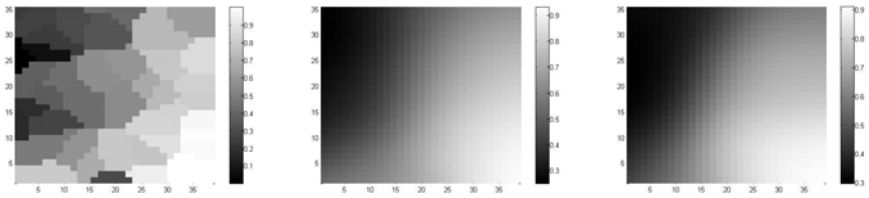

(a) Voronoi diagram (b) Centralized Kernel (c) SWOP

Fig. 4. Query results on the Intel lab data

figure

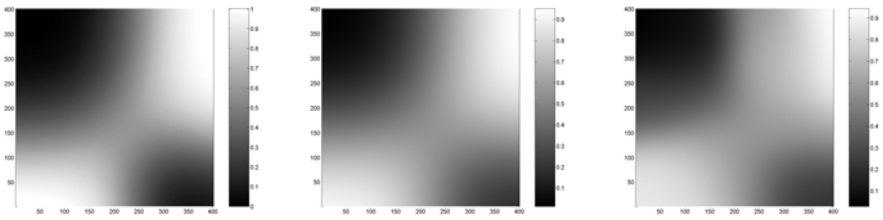

(a) Original Data (b) Centralized Kernel (c) SWOP

Fig. 5. Query results on the synthetic Data #1

figure

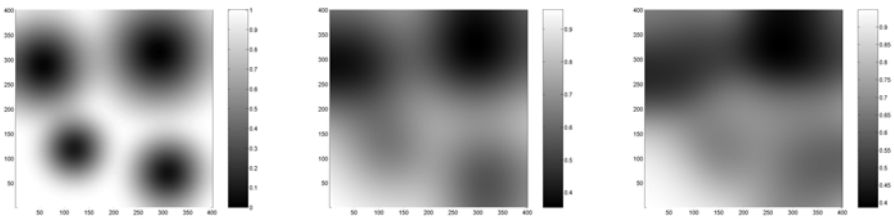

(a) Original Data (b) Centralized Kernel (c) SWOP

Fig. 6. Query results on the synthetic Data #2

figure

multiple independent tests on each data set, as shown by Table III. The clustering algorithm plays an important role in SWOP for the compression gain. After being clustered, a non-head node requires 192 bits to send its reading and ID to the cluster head. The message size for each cluster head to present its cluster members depends on the chosen order of Hermite coefficient. For the zero-order, each cluster head needs 256 bits to represent its member nodes for both the numerator and denominator in Equation 9. Since small clusters just send their raw readings, the average message size

is a little smaller than 256 bits as show by Table III. Compared with transmitting raw data for each cluster, SWOP saves 94% messages. The total communication cost of a network depends on different communication protocols and network layouts, and it is difficult to simulate SWOP for all cases. Users can find relevant evaluation results about it from [27], [29].

D. Comparison With Alternative Approaches

TABLE IV. Evaluation on wavelets

table

Coefficient threshold		Data size	MSE
readings	node ID		
Intel-Lab data			
0	0	698.98	0
0.2	0	449.71	9.53E-04
0.4	0	391.79	1.71E-02
0	6	661.98	1.23E-03
0	10	649.04	2.63E-03
0.3	6	310.82	8.53E-03
0.4	6	317.28	2.49E-02
0.3	8	323.61	8.6E-03
0.4	8	329.81	2.92E-02
Salinity data			
0	0	2896.26	0
0.2	0	1967.57	9.63E-04
0.4	0	1919.22	1.11E-02
0	0.10	1529.13	1.93E-03
0	0.2	1534.45	7.43E-03
0.2	0.1	651.84	1.97E-03
0.3	0.1	687.52	7.43E-03
0.2	0.15	619.79	6.43E-03
0.3	0.15	594.22	1.33E-02

1) Wavelet And Delta Compression: Any compression algorithm can be applied in clustering protocols to compress raw sensor readings for each cluster. We implemented Haar wavelets and allow cluster heads to transform raw readings and node IDs into wavelets. Table IV illustrates the experiment results on the two real data sets for different wavelet coefficient settings. An advantage of wavelets is that they can present data in different scales and compress lossless data based on which we can apply any analytical models. As shown in Table IV, Haar wavelets can compress lossless data in about 60% size of the raw data for each cluster. In our experiments, we only compared the centralized Kernel estimation results based on wavelet data with the Kernel estimation results on original data. By eliminating small wavelet coefficients, we can achieve higher compression rates, but degrade the estimated results. However, to achieve a similar quality of SWOP, wavelet-based methods require a larger data size than that SWOP does. More tests on the synthetic data sets and Delta-compression show similar results to wavelets, therefore we exclude the detailed comparison about them due to space limitations. By evaluating wavelets, Delta-compression and SWOP, we conclude that SWOP requires a smaller size of data but still returns high quality estimation results.

2) Spatial Regression: Since we fixed the bandwidth for both synthetic data sets, we compare SWOP with different 2D spatial regression methods on the synthetic data sets based on different estimation qualities. We did our tests to evaluate the estimation results against the "real" phenomena and the cost of processing alternative approaches in the network.

TABLE V. Evaluation on 2D polynomial regression

table

Polynomial Order	MSE	# of $f()s$
Synthetic data #1		
1	7.5E-02	3
2	1.2E-02	6
3	4.8E-03	10
4	1.5E-03	15
Synthetic data #2		
1	6.2E-02	3
2	6.0E-02	6
3	4.9E-02	10
4	2.6E-02	15

We run different 2D spatial regression methods in a traditional centralized setting on all raw data. The results based on different orders of polynomial regressions is shown by Table V. With higher orders of polynomial equations, the estimated results get better. To achieve a similar quality of SWOP with the current bandwidth setting, a 2D spatial polynomial regression requires 10 or more basis functions for both synthetic data sets. For Kernel regression, we test different numbers of kernels based on different kernel functions separated at fixed intervals with different bandwidths. Table VI illustrates the minimal MSE based on different numbers of kernels and different kernel functions. Table VI also shows the chosen bandwidth and kernel-center interval for the different kernel functions to return the best estimation results based on different numbers of kernels. To achieve a similar quality of SWOP, the Kernel regression requires 9 or more kernels. Figure 7 and Figure 8 show the estimation results based on the cubic polynomial, and the best estimation results based on 9 cone kernels and 9 Gaussian kernels for synthetic data #1 and #2 respectively.

Generally, both regression estimation methods require 9 or more basis functions to achieve a similar or better quality of SWOP. To return the final estimation results, we need at least $(81+9)\cdot k_i$ data from the network. Applying several types of kernel functions decreases the size of data exchanged among neighboring nodes, but the estimation results are not very smooth due to the discontinuity of the kernel functions (e.g. the estimation results based on cone kernels Figure 7(b)). On average, for both synthetic data, SWOP returns around 23 clusters, and requires a similar size of data, about $23\cdot 4\cdot k_i$, from the network for a similar quality compared with the 2D spatial regression methods. However, almost all nodes involved in regression methods need to receive and send the same large size of data. In SWOP, only the cluster heads near to the central base or a micro-server need to communicate with the large-sized messages. The nodes within a cluster and the nodes at the bottom on a routing tree in SWOP relax their communication costs. Furthermore, for the current cluster radius setting $0.9(80) = 72$ and the current spatial

table

TABLE VI. Evaluation on Kernel regression

# of kernels	Block kernel			Cone kernel			Gaussian kernel		
	Min MSE	Kernel Interval	Bandwidth	Min MSE	Kernel Interval	Bandwidth	Min MSE	Kernel Interval	Bandwidth
Synthetic data #1									
16	8.37E-03	110	165	4.06E-04	130	195	4.60E-04	110	95
9	2.09E-02	140	210	1.72E-03	140	210	1.15E-03	160	130
4	6.84E-02	200	300	1.37E-02	210	315	1.19E-02	210	265
Synthetic data #2									
16	2.96E-02	120	260	2.83E-02	110	325	3.85E-02	130	65
9	3.78E-02	170	255	4.13E-02	160	310	4.19E-02	150	75
4	6.26E-02	200	300	5.82E-02	200	300	5.89E-02	170	165

window size 401×401, a compact clustering pattern should contain less than 9 clusters; whereas the distributed clustering algorithms do not return an ideal clustering pattern. SWOP can achieve a higher compression gain by applying more sophisticated clustering methods.

Regression estimation methods focus on minimizing global errors, while SWOP and non-parametric estimation methods focus on revealing local variations. If we compare the estimation results of SWOP and regression estimation methods to the "real" underlying phenomena, the local change is better preserved by SWOP than by regression estimation methods for the similar global quality, MSE. For example, in Figure 8(a), one of the small peaks has totally disappeared.

VII. Related Work

As a basis for many protocols and a key element for sensor data processing, sensor node clustering algorithms are important in the field of sensor networks. LEACH [25] and HEED [24] are two of the most efficient algorithms available. LEACH first introduced a probability selection to choose the cluster head. Each node in LEACH can be the cluster head, and the probability of being a cluster head is predefined. Nodes rotate the roles of being a non-head member or a cluster head to save energy. HEED [24] improves the selection procedure by using other metrics, such as the remaining energy, to determine a dynamic probability. HEED has several additional advantages over LEACH, such as supporting multi-hop clustering.

Due to the constrained environment of sensor networks, sensor DBMSs favor aggregation queries. TAG [1] provides such a framework for this type of queries. TAG uses a tree structure to connect sensor nodes. Each node aggregates the partial results from its descendants, so the communication cost can be minimized and the messages are often kept constant. Trigoni et al. provide an optimization strategy for multiple aggregation queries in sensor networks [27], [29]. They categorized different types of aggregation queries and provided different optimization strategies to reform the communication topology.

As a result of the built-in spatial properties, sensor readings naturally support spatial queries. Simple aggregation queries [1], [2], however, often fail to generate correct answers for spatial aggregation queries if the nodes are not evenly distributed. Current approaches applied basic spatial interpolation methods, e.g. Voronoi diagram and TIN [10], to estimate the aggregation results. Kernel regression method has also been utilized to support spatio-temporal queries in sensor networks [14]. To find the weights for predefined kernel functions in the network, however, a sensor network requires iterations of communication [14], which deteriorates the network performance. In [13], a 2D polynomial regression was used to control the contour map quality.

In-network compression techniques are also important to sensor networks to reduce the in-network resource consumption. In [34], wavelet based compression has been introduced, where a sensor network can do pairwise comparison between sensor readings to generate discrete wavelets and reduce in-network transmitted data.

VIII. Conclusion And Future Work

In this paper, we presented a novel in-network estimation technique of spatial window queries, SWOP, designed for answering queries over continuous phenomena based on the Kernel estimation method. SWOP breaks the entangled links between estimation points and sensor nodes by utilizing Hermite expansion. In SWOP, a small number of Hermite coefficients represents all information about the invoked sensor nodes including their locations and readings. Hence, SWOP minimizes the size of data and relaxes the computation complexity, compared with a centralized solution and an ordinary distributed solution. Our simulation of SWOP tested the data sets of real phenomena, and synthetic data. The result of the simulation shows that SWOP competes well with other approaches by relaxing the resource consumptions and still providing high quality query results. We will combine the temporal and spatial aspects together for the future version of SWOP, which is not covered in this paper.

Acknowledgements: This research was funded under NSF grants NSF 0448183 and 0428341.

References

[1] S. Madden, M. J. Franklin, J. M. Hellerstein, and W. Hong, "Tag: a tiny aggregation service for ad-hoc sensor networks," *ACM SIGOPS*,

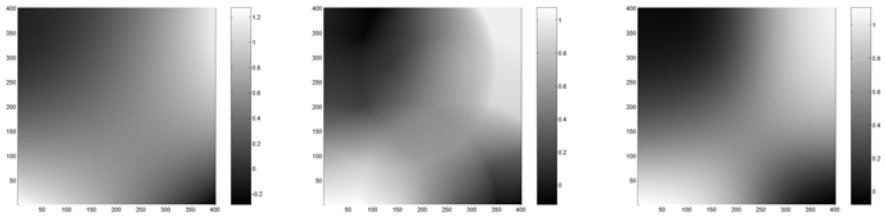

(a) Polynomial (b) Cone Kernel (c) Gaussian Kernel

Fig. 7. Alternative estimations on the synthetic data #1

figure

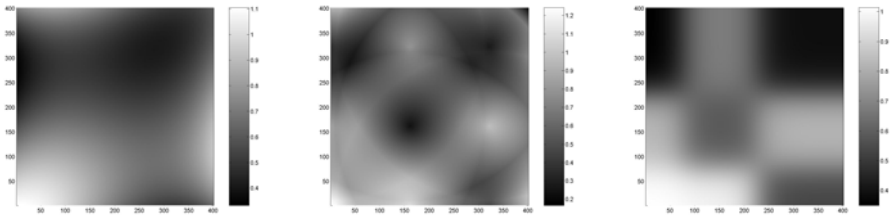

(a) Polynomial (b) Cone Kernel (c) Gaussian Kernel

Fig. 8. Alternative estimations on the synthetic data #2

figure

vol. 36, no. SI, pp. 131–146, 2002.

[2] J. M. Hellerstein, W. Hong, S. Madden, and K. Stanek, "Beyond average: Toward sophisticated sensing with queries.," in *IPSN*, pp. 63–79, 2003.

[3] A. Demers, J. Gehrke, R. Rajaraman, N. Trigoni, and Y. Yao, "The cougar project: a work-in-progress report," *SIGMOD Record*, vol. 32, no. 4, pp. 53–59, 2003.

[4] P. Bonnet, J. Gehrke, and P. Seshadri, "Querying the physical world," *IEEE Personal Communication*, vol. 7, pp. 10–15, 2000.

[5] G. Tolle, J. Polastre, R. Szewczyk, D. Culler, N. Turner, K. Tu, S. Burgess, T. Dawson, P. Buonadonna, D. Gay, and W. Hong, "A macroscope in the redwoods," in *ACM SenSys*, pp. 51–63, 2005.

[6] J. Burrell, T. Brooke, and R. Beckwith, "Vineyard computing: Sensor networks in agricultural production," *IEEE Pervasive Computing*, vol. 3, pp. 38–45, Jan. 2004.

[7] M. Duckham, S. Nittel, and M. Worboys, "Monitoring dynamic spatial fields using responsive geosensor networks," in *ACM GIS*, pp. 51–60, 2005.

[8] A. Deligiannakis, Y. Kotidis, and N. Roussopoulos, "Compressing historical information in sensor networks," in *ACM SIGMOD*, pp. 527–538, 2004.

[9] A. Jain, E. Y. Chang, and Y.-F. Wang, "Adaptive stream resource management using kalman filters," in *ACM SIGMOD*, pp. 11–22, 2004.

[10] M. Sharifzadeh and C. Shahabi, "Supporting spatial aggregation in sensor network databases," in *ACM GIS*, pp. 166–175, 2004.

[11] F. Aurenhammer and Klein, *Handbook of Computational Geometry*, ch. 5. Elsevier Science Pub Co, 1st ed., January 1, 2000.

[12] B. Harrington and Y. Huang, "In-network surface simplification for sensor fields," in *ACM GIS*, pp. 41–50, 2005.

[13] W. Xue, Q. Luo, L. Chen, and Y. Liu, "Contour map matching for event detection in sensor networks," in *ACM SIGMOD*, pp. 145–156, 2006.

[14] C. Guestrin, P. Bodík, R. Thibaux, M. A. Paskin, and S. Madden, "Distributed regression: an efficient framework for modeling sensor network data.," in *IPSN*, pp. 1–10, 2004.

[15] V. Delouille, R. Neelamani, and R. G. Baraniuk, "Robust distributed estimation in sensor networks using the embedded polygons algorithm.," in *IPSN*, pp. 405–413, 2004.

[16] J. Racine, "Parallel distributed kernel estimation," *Computational Statistics and Data Analysis*, vol. 40, no. 2, pp. 293–302, 2002.

[17] M. Broadie and Y. Yamamoto, "Application of the fast gauss transform to option pricing," *Management Science*, vol. 49, no. 8, pp. 1071–1088, 2003.

[18] C. Yang, R. Duraiswami, N. A. Gumerov, and L. Davis, "Improved fast gauss transform and efficient kernel density estimation," in *ICCV*, pp. 464–471, IEEE Computer Society, 2003.

[19] L. Greengard and J. Strain, "The fast gauss transform," *SIAM Journal on Scientific and Statistical Computing*, vol. 12, no. 1, pp. 79–94, 1991.

[20] B. J. C. Baxter and G. Roussos, "A new error estimate of the fast gauss transform," *SIAM Journal on Scientific Computing*, vol. 24, no. 1, pp. 257–259, 2002.

[21] O. Szász, "On the relative extrema of the hermite orthogonal functions," *J. Indian Math. Soc.*, vol. 25, pp. 129–134, 1951.

[22] M. Bern and D. Eppstein, "Approximation algorithms for geometric problems," pp. 296–345, 1997.

[23] J. Han and M. Kamber, *Data Mining: Concepts and Techniques*. Morgan Kaufmann, 1 ed., 2001.

[24] O. Younis and M.-S. Fahmy, "Heed: A hybrid, energy-efficient, distributed clustering approach for ad hoc sensor networks," *IEEE Transactions on Mobile Computing*, vol. 3, no. 4, pp. 366–379, 2004.

[25] W. B. Heinzelman, A. P. Chandrakasan, and H. Balakrishnan, "An application-specific protocol architecture for wireless microsensor networks," *IEEE Transactions on Wireless Communications*, vol. 1, no. 4, pp. 660–670, 2002.

[26] G. Jin and S. Nittel, "Udc: A self-adaptive uneven clustering protocol for dynamic sensor networks," in *International Conference on Mobile Ad-hoc and Sensor Networks (MSN)*, 2005.

[27] N. Trigoni, Y. Yao, A. J. Demers, J. Gehrke, and R. Rajaraman, "Multi-query optimization for sensor networks.," in *DCOSS* (V. K. Prasanna, S. S. Iyengar, P. G. Spirakis, and M. Welsh, eds.), vol. 3560 of *Lecture Notes in Computer Science*, pp. 307–321, Springer, 2005.

[28] R. Nowak and U. Mitra, "Boundary estimation in sensor networks: Theory and methods.," in *IPSN*, pp. 80–95, 2003.
[29] N. Trigoni, Y. Yao, A. J. Demers, J. Gehrke, and R. Rajaraman, "Multi-query optimization for sensor networks," In TR2005-1989, Cornell University, 2005.
[30] A. Bucklina, P. H. Wiebeb, S. B. Smolenacka, N. J. Copleyc, and M. E. Clarke, "Integrated biochemical, molecular genetic,and bioacoustical analysis of mesoscale variability of the euphausiid nematoscelis difficilis in the california current," *Deep-Sea Research*, vol. 49, pp. 437–462, 2002.
[31] http://berkeley.intel research.net/labdata/.
[32] O. V. Lepskii and V. Spokoiny, "Optimal pointwise adaptive methods in nonparametric estimation," tech. rep., undated.
[33] V. C. Raykar and R. Duraiswami, "Fast optimal bandwidth selection for kernel density estimation," in *Proceedings of the sixth SIAM International Conference on Data Mining* (J. Ghosh, D. Lambert, D. Skillicorn, and J. Srivastava, eds.), pp. 524–528, 2006.
[34] J. Hellerstein and W.Wang, "Optimization of in-network reduction," in *VLDB-Workshop DMSN*, pp. 166–175, 2004.

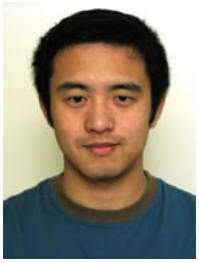

Guang Jin Guang Jin is a graduate student at the Department of Spatial Information Science and Engineering at the University of Maine, Orono, Maine, USA. Since 2003 he has been researching in sensor networks and query processing in sensor networks.

Silvia Nittel Dr. Silvia Nittel is an Associate Professor in the Department of Spatial Information Science and Engineering at the University of Maine. She received her Ph.D. in databases from the University of Zurich in 1994. Her current research focuses on database management techniques for sensor networks, especially sensor networks deployed in environmental and geographic applications. She co-organized the first workshop on "Geosensor Networks", and co-authored the first book in this area.